

2024

High measurement rate property measurement methods for molten salts

<https://hdl.handle.net/2144/49312>

Downloaded from DSpace Repository, DSpace Institution's institutional repository

BOSTON UNIVERSITY
COLLEGE OF ENGINEERING

Dissertation

**HIGH MEASUREMENT RATE PROPERTY MEASUREMENT
METHODS FOR MOLTEN SALTS**

by

ALEXANDER S. LEVY

B.S., Drexel University, 2016

Submitted in partial fulfillment of the
requirements for the degree of
Doctor of Philosophy

2024

© 2024 by
Alexander S. Levy
All rights reserved

Approved by

First Reader

Uday B. Pal, Ph.D.
Professor of Mechanical Engineering
Professor of Materials Science and Engineering

Second Reader

Karl F. Ludwig, Jr., Ph.D.
Professor of Physics
Professor and Associate Division Head of Materials Science and
Engineering

Third Reader

Soumendra N. Basu, Ph.D.
Professor of Mechanical Engineering
Professor and Associate Division Head of Materials Science and
Engineering

Fourth Reader

Srikanth Gopalan, Ph.D.
Professor of Mechanical Engineering
Professor of Materials Science and Engineering

DEDICATION

I would like to dedicate this work to my parents, Ruth Mayer and Mark Levy,
and my partner, Xi (Sophie) Jiang.

ACKNOWLEDGMENTS

I would like to express my appreciation to my PI Prof. Uday Pal. Without his expertise and guidance, I would have not been able complete this work. I also greatly appreciate his patience and understanding that research takes time and cannot be completed in a day, I rarely felt pressured when experiments went awry. I would also like to thank my co-advisor Prof. Karl Ludwig for his guidance and support. In addition, I would like to extend my gratitude to my committee members Prof. Basu and Prof. Gopalan.

I also want to express my gratitude for the staff of EPIC, including Bob Sjostrom, Joe Estano, Kara Morgensen, Tasker Smith, Ryan Bakinowski, Caroline Carbo, and Adam Zelny. Their support and knowledge of manufacturing was a critical piece for the completion of my research. I'd like to thank Dr. Alexey Nikiforov for his valuable support and instructions in scanning electron microscopy. I'd like to thank Anna Masland and Emery Dutton along with the rest of the ME office staff for their constant assistance.

My acknowledgement also goes to my past and current colleagues. I am particularly grateful to Dr. Haoxuan Yan and Anubhav Wadehra for being excellent collaborators as we learned and troubleshooted the work together. The three of us shared in the frustrations of failure and joys of success. Anubhav Wadehra's parallel work on X-Ray Measurement Techniques provided excellent opportunities for us to explore these materials in ways we would have otherwise ignored. I would also like to thank Dr. Michelle Sugimoto, Dr. Jillian Mulligan, Dr. Ayesha Akter, John-In Lee, Emily Gosh, Haoxiang Yu, Kaixin Suo, and Toluwalope John for their support, friendship and advice.

To all other colleagues who have contributed their time, shared their knowledge, and helped in many forms, I express my gratitude.

I would like to express my sincere gratitude to Hadassah Flagg, Federico Coppo, Farah Haidar, and David Taman. As undergraduates, your assistance and commitment to the research work have been an invaluable contribution to the completion of this project.

Lastly, I want to express my deepest gratitude to my family. To my parents, Ruth Mayer and Mark Levy, who always supported me and encouraged me to pursue my interests. To my partner, Xi (Sophie) Jiang, who's love, support and encouragement knows no bounds. Without her, I would have never pursued or accomplished this.

HIGH MEASUREMENT RATE PROPERTY MEASUREMENT

METHODS FOR MOLTEN SALTS

ALEXANDER S. LEVY

Boston University, College of Engineering, 2024

Major Professor: Uday B. Pal, Ph.D., Professor of Mechanical Engineering, Professor of Materials Science and Engineering.

ABSTRACT

The demand for clean energy production and storage has inspired research in molten salt-based technologies. Understanding of how molten salts change with respect to temperature is vital to establishing efficient, cost-effective systems. Experimental measurements of physical properties and parallel x-ray studies of material structure can be used together to better understand how the molten salt speciation and behavior changes with temperature. Limited research into such materials means there are knowledge gaps and uncertainty in reported property values with respect to temperature due to difficulties in accurate experimental determination of properties. This is in part due to the stringent environmental requirements necessary due to the reactivity of the materials at elevated temperatures. Additionally, common high temperature techniques are time consuming, limiting the quantity of materials that can be evaluated. Many research efforts attempt to utilize MD modeling to fill these gaps and accelerate this process, however accurate physical measurements are still required to verify the results.

This thesis presents the development of glove box compatible techniques that are chosen with the intent of reducing measurement time while still providing accurate results of thermophysical properties as a function of temperature. Studies were performed on two candidate molten salts for one technology of interest, the Molten Salt Reactors

(MSRs). The first is FLiNaK, the well-studied eutectic of the LiF-KF-NaF system with the composition of 46.5-11.5-42 mole percent. The second is a lesser studied salt NaF-ZrF₄ with a composition of 53-47 mole percent. This salt was chosen as a surrogate for the NaF-ZrF₄-UF₄ fuel candidate used in the original MSR experiments between 1950 and 1970.

Properties measured in this work include viscosity, surface tension and density. Viscosity was measured with a falling ball viscometer adapted to high temperature applications. The intent of this system was to provide viscosity measurements as a function of temperature while minimizing sampling time and sample quantity. The applicable testing conditions were extended beyond the Stokes Flow regime (Reynolds Number < 1) typically used in the classic falling ball viscometer. A high temperature induction sensor was developed to measure the rate of the falling metallic ball, in this case Ti. Additionally, density and surface tension were measured simultaneously as a function of temperature with the maximum bubble pressure method. Combining these property measurements reduces total measurement time by eliminating the need for a second experiment. This method also addresses the effect of surface tension on density measurements that is commented on in published literature for molten salts, including FLiNaK and NaF-ZrF₄. Considerations were made on both measurements to address environmental effects that might influence results. Characterization of salt samples before and after measurements were performed to provide context for the accuracy of the measurements with respect to temperature that may arise from these interactions with the environment and the materials used in the experiments.

TABLE OF CONTENTS

DEDICATION	iv
ACKNOWLEDGMENTS	v
ABSTRACT.....	vii
TABLE OF CONTENTS.....	ix
LIST OF TABLES	xii
LIST OF FIGURE.....	xiii
1. INTRODUCTION.	1
1.1. History of Molten Salt Reactors & Reactor Technology.....	1
1.2. Molten Salts in MSR.....	3
1.3. Importance of Thermophysical Properties in Molten Salts	5
1.3.1. Density	6
1.3.2. Viscosity	7
1.3.3. Surface Tension	8
1.3.4. Other MSR Salt Thermophysical Properties.....	9
1.4. Research Scope	10
2. OVERVIEW OF EXISTING MEASUREMENT TECHNIQUES	11
2.1. Density Methods	12
2.2. Viscosity Methods	13
2.3. Surface Tension Methods	17
3. MATERIALS PROCESSING, HANDLING AND CHARACTERIZATION	20
3.1. Molten Salt Impurities	21
3.2. Experimental Environment	22
3.2.1. Glove Box Testing Environment	23

3.2.2.	X-Ray Measurement Sample Holder Designs	26
3.3.	Material Synthesis and Handling	29
3.4.	Characterization Methods, Techniques and Procedures	30
3.4.1.	Visual Inspection	30
3.4.2.	Digital Scanning Calorimetry (DSC) & Thermogravimetric Analysis (TGA).....	33
3.4.3.	X-Ray Powder Diffraction (XRD).....	38
3.4.4.	Inductively Coupled Plasma Optical Emission Spectroscopy (ICP-OES) and Ion Selective Electrode (ISE).....	43
3.4.5.	Scanning Electron Microscopy (SEM) with Energy Dispersive X-ray Spectroscopy (EDS).....	44
3.5.	X-Ray Sample Handling Procedure and Relevant Lessons Learned.....	47
3.6.	Material Processing, Synthesis & Characterization Summary	52
4.	SURFACE TENSION & DENSITY DEVICE AND MEASUREMENTS	53
4.1.	Introduction.....	53
4.2.	Sample Preparation	55
4.3.	Maximum Bubble Pressure Testing Setup.....	56
4.4.	Maximum Bubble Pressure Experimental Procedure	60
4.5.	Maximum Bubble Pressure Data Analysis	62
4.6.	Maximum Bubble Pressure Results	65
4.6.1.	Room Temperature Testing and Verifications.....	65
4.6.2.	Molten Salt Measurement Results	68
4.6.3.	Post Measurement Characterization	73
4.7.	Discussion.....	81
4.8.	Maximum Bubble Pressure Measurements Summary	83

5. HIGH TEMPERATURE FALLING BALL VISCOMETER & VISCOSITY	85
5.1. Introduction.....	85
5.2. Material Synthesis and Analysis.....	88
5.3. Falling Ball Viscometer Theory, System and Calculations	90
5.3.1. Velocity – Viscosity Relationship: Modeling & Validation.....	91
5.3.2. Ball Drop Mechanism.....	96
5.3.3. Sensing Device: High Temperature Solenoid Coils	97
5.3.4. Ball Detection	99
5.3.5. Falling Ball Viscometer Experimental Procedure	102
5.3.6. Molecular Dynamic Methods	104
5.4. Viscosity Results.....	105
5.5. Viscosity Discussion & Conclusion	109
6. CONCLUSIONS AND FUTURE WORK.....	113
6.1. Conclusions.....	113
6.2. Future Work	116
APPENDIX.....	119
BIBLIOGRAPHY.....	126
CURRICULUM VITAE.....	134

LIST OF TABLES

Table 3.1: ICP-OES & Fluorine Results Compared to Ideal Composition of FLiNaK....	44
Table 3.2: ICP-OES & Fluorine Results Compared to Ideal Composition of NaF-ZrF ₄ .	44
Table 3.3: Composition of Supra 55VP and Phenom of As Made salt samples.....	46
Table 3.4: Sample composition by EDS analysis of x-ray chamber testing on NaF-ZrF ₄	49
Table 3.5: Selected tests (incomplete) of various conditions on both salts showing possible indication of effect of different environmental conditions	51
Table 4.1: Room Temperature Water Surface Tension and Density Verification Measurements	66
Table 4.2: FLiNaK Density kg/m ³ Coefficients	69
Table 4.3: FLiNaK Surface Tension (mN/m) Coefficients	70
Table 4.4: NaF-ZrF ₄ Density kg/m ³ Coefficients	72
Table 4.5: NaF-ZrF ₄ Surface Tension (mN/m) Coefficients	73
Table 5.1: Viscosity $Pa \cdot s$ FLiNaK Eutectic Arrhenius Coefficients (Equation 5.24)..	106
Table 5.2: NaF-ZrF ₄ (53-47 mol%) and similar compositions Viscosity [$Pa \cdot s$] Arrhenius Coefficients (Equation 5.24).....	108
Table 5.3: Percent difference in viscosity at select temperatures between MD and experimental results evaluated with the same density.	109

LIST OF FIGURES

Figure 1.1: MSR Reactor Conceptual Diagram [11]	3
Figure 2.1: Diagram of the Archimedes method as developed by Argonne National Lab for measuring density of molten fluoride and chloride salts for MSR applications. [27].....	13
Figure 2.2: The internal diagram (a) and (b) the modified furnace setup and Brookfield rheometer as developed by Argonne National Lab for measurement of molten salts fluoride and chloride salts for MSR applications. [26].....	14
Figure 2.3: The high temperature oscillating cup rheometer method as described by Ito to measure molten NaCl. [32]	16
Figure 2.4: Conceptual diagram of the rolling ball viscometer showing the breakdown of applicable forces as described by Biiri, where \mathbf{FG} is the gravitational force, \mathbf{FL} is the lift force, \mathbf{FB} is the buoyancy force and f is the drag force. [34].....	17
Figure 3.1: Schematic of the Glove box furnace with staged components for viscosity measurement (as described in Section 4).....	25
Figure 3.2: Image of the glove box and assembled furnace when first installed.....	25
Figure 3.3: The custom heating element for the glove box furnace. a) Depicts the heating element after the Kanthal wire is wrapped and annealed at 1200 °C. b) The wire is then pasted to the alumina tube, and a steel thermal conductor inserted inside. c) The heating element is then installed into the furnace with steel couplings were used to attach the exposed ends of the Kandhal wire (leads) to electrical cables. An outer Alumina tube housing is used to help to support and protect the heating element...	26
Figure 3.4 a) Diagram of heater and sample holder for glassy carbon crucible designed for PDF scattering experiments. b) The as made heating element and ceramic holder with Kanthal heating wire pasted onto the surface of the Formlabs 3D printed ceramic holder. c) The holder as mounted to the stage as it would be seen in the x-ray test chamber.	28
Figure 3.5: a) The EXAFS/XANES thin sample holder as assembled schematic using b) HBN plates with a 100 μm depression. The front (c) and side (d) views of the sample holder as assembled and e) the holder wrapped in Alumina Wool as attached to the stage of the x-ray test chamber.	29
Figure 3.6: Fractured as made sample of NaF-ZrF ₄ showing the top (black/gray, gas-salt) and bottom (white, Ni-salt) interfaces as observed after synthesis.....	31

Figure 3.7: FLiNaK coloration of various salt samples as exposed to different conditions. a) An as-made sample with no impurities b) a sample exposed to an inadequate gas environment (high oxygen content). c & d) a sample tested after surface tension measurements using Stainless Steel bubbling tubes that show indication of dissolved metals, metal oxide or metal fluoride possibly due to reaction of chromium in the stainless steel with trace oxygen/moisture impurities in the glovebox.	33
Figure 3.8: NaF-ZrF ₄ phase diagram with relevant composition labeled. [56]	34
Figure 3.9: LiF-NaF-KF Phase diagram as generated using the FactSage thermodynamics database with the eutectic composition labeled.	35
Figure 3.10: DSC/TGA of FLiNaK. Approximate melting and solidification temperatures are labeled, 446 °C and 442 °C, respectively. It is comparable to the theoretical melting point of 456 °C.	36
Figure 3.11: DSC/TGA Analysis of NaF-ZrF ₄ . Approximate melting point is 501 °C, it is comparable to the melting point identified in literature of 520 °C.	36
Figure 3.12: TGA mass loss data of FLiNaK as a function of temperature, where a) is the initial collected data and b) is the analyzed percentage loss at each set temperature by evaluating the slope of the weight change as a function of time.	37
Figure 3.13: Example of hygroscopic behavior exhibited by FLiNaK when exposed to air for 5 minutes or less.	38
Figure 3.14: XRD diffraction patterns of as-made FLiNaK samples prepared with Domed holder as shown in Figure 3.15.a and Kapton tape as shown in Figure 3.15.b. Signals are shown with the background included and the background removed to compare the effect of each holder.	39
Figure 3.15: Example sample holder methods for performing FLiNaK XRD scans, a) the domed cover available from Bruker and b) a regular sample holder covered with Kapton tape.	40
Figure 3.16: XRD scans showing the effect of hydration of FLiNaK samples as exposed to moisture in the air on days of varying humidity levels. They are compared to a sample with no humidity, sealed with a Kapton tape cover.	41
Figure 3.17: XRD diffraction patterns of NaF-ZrF ₄ (53-47 mol%) with comparable PDF cards for similar composition F ₃₁ -Na ₇ -Zr ₆ (53.8-46.2 mol%) and potential impurity ZrO ₂ . No ZrO ₂ peaks are observed.	42
Figure 3.18: XRD Scan of a) Oxyfluoride identified in NaF-ZrF ₄ sample including higher levels of ZrO ₂ and b) low oxygen content oxyfluoride identified in baked ZrF ₄ under	

inadequate conditions. Additional peaks not identified are potentially additional oxyfluoride phases.	43
Figure 3.19: Comparison of SEM/EDS as performed on the SUPRA and Phenom RPOX Desktop SEM with EDS values reported in Table 3.....	46
Figure 3.20: Mapping of as made NaF-ZrF ₄ region near Ni-salt interface showing formation of ZrO ₂ collecting in the salt.	46
Figure 3.21: Associated samples from x-ray chamber procedural testing. A) The as made sample as produced in the glove box environment. This image shows higher levels of ZrO ₂ as produced at an interface of the salt sample, also more common in earlier samples. B) A sample tested without the Drierite column and oxygen trap. C) A sample tested at 800 °C for 2 hours resulting in low Zr content. These samples are often difficult to polish, resulting in uneven surfaces.	49
Figure 4.1: Diagram of bubbling tube and plumbing schematic used for surface tension.	58
Figure 4.2: Pictures of the surface tension probe where a) shows the entire assembly prior to inserting it into the furnace. The flange (A) and alumina tube (B) for mounting the tube sub-assembly are clearly visible. The internal bottom portion of the assembly is shown in b) where the lid and guide (C) have the bubbling tube (D) thermocouple (E) and reference wire (F) with alumina sheathing interested through it. The top half of the assembly is clearly shown in c) showing the screw micrometer (G) as assembled with the movable guide block (H). The top portion of the bubbling tube (D) thermocouple (E) and reference wire (F) are also visible. The reference wire for the alumina sheath (J) is not attached to the moving block (H). A guide (I) is used to prevent the moving portion from twisting. The top of the flange (K) is used to mount to the flange body (A). The entire assembly is inserted into the furnace as shown in d) where the gas line and reference wire connections are attached.	59
Figure 4.3: Baseline pressure reading of uncalibrated signal of PX409 pressure transducer while installed into glove box with flowing gas.	60
Figure 4.4: Pressure data as a function of depth as collected at 645 °C on the NaF-ZrF ₄ showing distinct pressure changes at each depth.	62
Figure 4.5: An example of data collected that includes early bubble release identified by short bubble formation times with outlying low peak pressure. These bubbles are indicated by the red arrows.	63
Figure 4.6: The average maximum peak plotted as a function of uncorrected (black) and corrected (red) depths at 645 °C. Note that the intercepts remain constant, as the density can be evaluated independently from surface tension.	65

Figure 4.7: Stages of bubble formation as observed with collected data in this study. The bubble starts forming initially (1) with slow pressurization slowly increasing bubble size (2,3) and reaching a maximum pressure as a hemisphere (4). Bubbles are then detached from the inner radius of the tube (5) and rapidly expand while the pressure decreases (6) before releasing from the tube.	66
Figure 4.8: Comparison of spike anomalies during bubble formation between different size diameter tubes.	67
Figure 4.9: As measured FLiNaK density compared to select studies from literature.	68
Figure 4.10: As measured FLiNaK surface tension compared to available published studies.	70
Figure 4.11: As measured NaF-ZrF ₄ Density compared to selected studies from literature of varying compositions.	71
Figure 4.12: As measured NaF-ZrF ₄ surface tension compared to available published studies.	72
Figure 4.13: XRD scans of as measured FLiNaK. For this salt, samples are only taken from near the top of the crucible. Samples are compared to salt precursors the as made salt scan.	74
Figure 4.14: XRD Scans of as measured NaF-ZrF ₄ samples taken at different depths, near the top, middle, and bottom of the sample to look for indications of high oxyfluoride content. Scans are compared to Na ₇ Zr ₆ F ₃₁ and the as made salt scan.	74
Figure 4.15: Example SEM images of tube cross sections a) A cross section of a prepared tube ends inner corner. b) A cross section of a tube end after exposure to FLiNaK. Note the heavy radius is as prepped, not from corrosion. c) A cross section of a tube with sharper corner between the inner edge and bottom surface end after exposure to NaF-ZrF ₄ . Note, the heavy corrosion on the sharp corners of the tube.	77
Figure 4.16: Comparison of segments of (a) a Control Tube Stainless Steel 304 tube and (b) a Stainless Steel 304 tube exposed to FLiNaK. Tube segments are away from the tube end but show similar variation in each (maximum difference of 11 μm and 15 μm respectively). Note the outside surfaces remain straight for both tubes.	78
Figure 4.17: EDS Line scan of outer edge of a Stainless Steel 304 control tube showing only Cr, Fe and Ni content.	80
Figure 4.18: EDS Line scan of outer edge of a Stainless Steel 304 control tube showing only Cr, Fe and Ni content.	81

Figure 4.19: EDS Line scan of outer edge of a Stainless Steel 304 used with NaF-ZrF ₄ showing only Cr, Fe and Ni content. Cr and Fe content appear to decrease in corroded region where pitting occurs. Where Fe decreases Zr increases, indicating Fe results are affected by the presence of Zr on the surface.	81
Figure 5.1: XRD of NaF-ZrF ₄ (53-47 mol%) of as made salt sample compared to after run sample, with Na ₇ Zr ₆ F ₃₁ PDF used as a baseline for comparison.	89
Figure 5.2: XRD of FLiNaK of as made salt sample compared to after run sample with appropriate precursor PDF comparison.	90
Figure 5.3: Diagram of high temperature falling ball viscometer design (not to scale) illustrating the basic setup of the vertical cylindrical heater, thermal conductor with cavity for the sample and solenoid sensors as positioned inside the glove-box sized furnace.	91
Figure 5.4: COMSOL derived velocities of Brookfield Standards compared to room temperature experimental results.	95
Figure 5.5: Extended verification of model using COMSOL simulation to evaluate the flow conditions of different Re numbers.	96
Figure 5.6: Ball Drop assembly exploded view A) Dropping rod B) Load ball in this tube before dropping C) Loading Mechanism D) Tube for balls waiting to be loaded E) Mounting Flange F) Knob for loading balls G) lever for turning dropping rod.	97
Figure 5.7: Assembly of (a) solenoid coils from start to finish, excluding the curing steps and attachment of the bottom spacer and (b) the finished assembly.	98
Figure 5.8: Circuit loop of modified tank circuit for proximity detection of metallic balls.	99
Figure 5.9: Dual coil signals example after post processing with Low Pass Filter for the appropriate frequency.	101
Figure 5.10: Example Data of 579 °C average temperature looking at all cutoff frequencies for the low pass filter. Data demonstrates convergence of Sample at the approximate cutoff frequency (0.47 Hz) as seen in the Standard Deviation.	101
Figure 5.11: Fully assembled ball drop mechanism with coil assembly A) Coil Assembly B) Ball Loading and dropping mechanism C) Lead Attachment to connect to Arduino circuit.	102
Figure 5.12: Results from validation testing of terminal velocity of NaF-ZrF ₄ at elevated temperatures.	103

Figure 5.13: Prediction from COMSOL model of distance to reach terminal velocity and respective Reynold's number as a function of temperature for FLiNaK (a) and NaF-ZrF₄ (b). Reynold's Number confirms if the predicted velocity is in a reasonable range for the laminar flow model, and peak salt height is determined to be the salt height of the available molten salt at a given temperature based on weighed mass and reported density. 103

Figure 5.14: As measured FLiNaK viscosity as a function of temperature with an exponential-Arrhenius fit compared to selected former studies. 106

Figure 5.15: As measured NaF-ZrF₄ (53-47 mol%) viscosity as a function of temperature with an exponential-Arrhenius fit compared to selected former studies. 107

1. INTRODUCTION

Across many industries environmentally clean technologies are being explored to mitigate greenhouse gas emissions. As a result, molten salt technologies have made a resurgence as replacements for some established industry standard technologies such as materials production, energy storage and energy production [1, 2, 3]. While each technology has unique salt property requirements, resulting in variation of materials selected, the desired understanding of the underlying science and the tools to study them are largely the same. Knowledge of the relationships between molten These material studies including liquid salt structure, speciation, and thermophysical properties and how they relate to structure, speciation, and are critical in explaining the overall behavior of the molten salt and its applicability for a particular application. This work explores methods to study these properties for select molten salts under consideration for applications in Molten Salt Reactors (MSR).

1.1. History of Molten Salt Reactors & Reactor Technology

When operated without any negative incidence, nuclear energy is considered an excellent form of emission-free energy production, accounting for 18.9% of U.S. energy production in 2021. [4]. The technology utilized in operational reactors has not changed significantly since Generation II and III reactors were brought online in the late 1990's. These reactors are variations of water-cooled solid fuel systems, with the major difference between Generation II and Generation III reactors being associated with operational longevity and safety. Additionally, these reactors exhibit many operational concerns that have decreased public support in continuing nuclear energy expansion. [5]

Molten Salt Reactors (MSR), first demonstrated in the 1954 in the Aircraft Reactor Experiment (ARE), are a class of nuclear reactor that is believed to address many downfalls of current reactor technologies while still providing efficient low carbon energy production. [5, 6] These reactors, considered as one design option for Generation IV reactors, offer many advantages over Generation II and III reactors, including improved safety, improved operational efficiency due to higher temperature operating potentials, and lower waste generation. [7, 8] Additionally, they provide operational benefits that other Generation IV reactor candidates do not have such as remote-online refueling and lower fissile densities. Additional safety measures can be easily implemented, such as emergency dump tanks that can quench the fissile salt quickly in the case of an emergency stopping any reaction. MSR are characterized as containing liquid fuel in the form of molten salt, dissolved into a carrier-coolant salt, described further in Section 1.2. [7, 9, 10]

The molten salt reactor, as shown in Figure 1.1, is generally comprised of a main reactor core, a primary heat exchange loop, and a steam plant loop. Much like a conventional reactor, the main reactor core is where heat is generated through a controlled nuclear reaction of fissile material. Similarly, a primary heating loop removes heat energy from the reactor core, however the working fluid is molten salt instead of a water-steam system in previous generation plants. This primary heat exchanger is considered “clean” as it contains no fissile material and acts as a bridge between the radioactive main core and power generation. The molten heated molten salt can then be pumped to a secondary heat exchanger, to power a more typical steam plant for energy

production. [7]

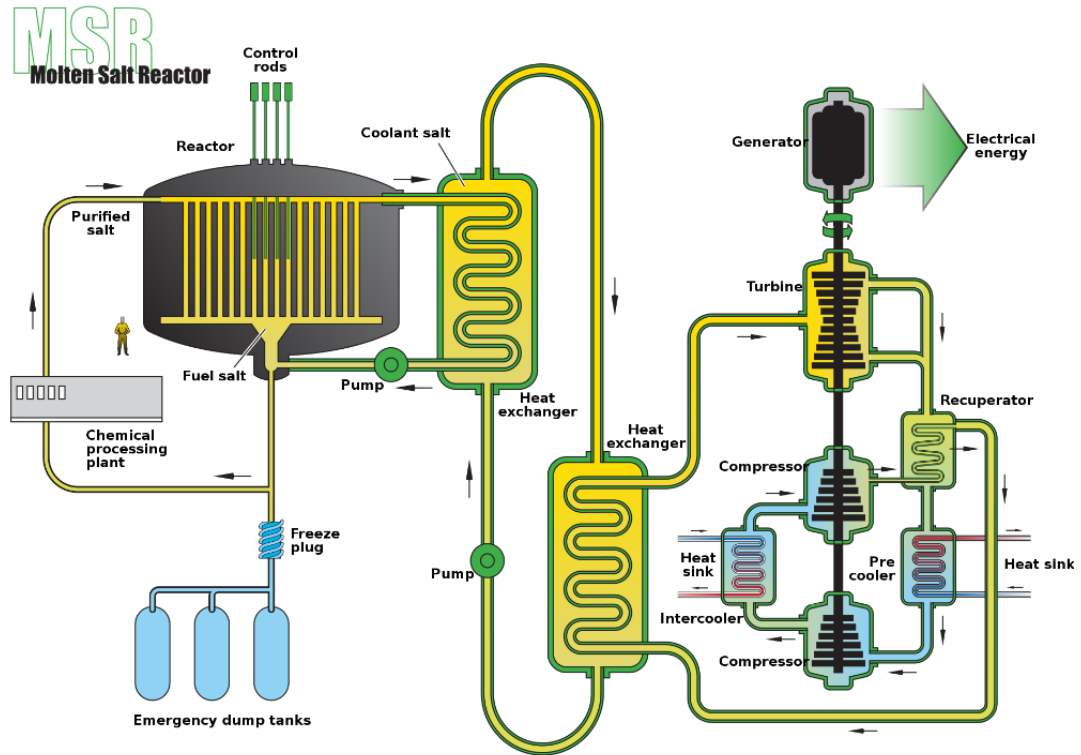


Figure 1.1: MSR Reactor Conceptual Diagram [11]

1.2. Molten Salts in MSR

Molten salt technologies utilize a wide range of salt compounds in which salts with thermophysical properties beneficial to the specific function are selected. For example, thermal molten salt batteries include nitrides, chlorides, or even sulfides that are cheap, abundant, and easy to obtain but have high heat capacity and thermal conductivity. Some of these salts however are not adequate in applications such as MSR reactors, for reasons such as material stability or inappropriate for use with fissile materials. [2]

Mixtures explored for MSR primarily include fluoride and chloride salts, each with their own advantages. MSR systems are designed around the use of molten salts

which can be characterized for two general purposes, each applying to the given section of the reactor. These are the primary coolants (also known as fuel-salt carriers) and secondary coolants (also known as heat transfer salts). Primary coolants are molten salts that contain fissile material, often a uranium (UF_3 , UF_4 , UCl_3), plutonium (PuF_3 , PuCl_3), or thorium (ThF_4 , ThCl_4) salt dissolved into a carrier fluid. The fissile materials' purpose is equivalent to that of a solid fuel in a conventional reactor. While the salt is molten, heat is generated by the fissile material in controlled nuclear fission. This heated salt is continuously pumped from the reactor core to a heat exchanger where energy is removed by the secondary coolant. The secondary coolant salts have no radioactive elements (clean salts) and can more safely transfer the heat to a conventional steam plant system. [2, 5, 11, 12]

During the ARE, the first primary fuel molten salt material used was a mixture of NaF , ZrF_4 and UF_4 (mixture of 53-41-6 mole percent (mol %)). Variations on this salt are still explored today, although the industry has developed a significant interest in a wide range of fluoride and chloride salts beyond this mixture. [13] Fluoride salts are more classically considered for MSRs that utilize thermal-neutron or slow-neutron reactors. One newer example of a reference material for many studies is the LiF-NaF-KF eutectic (46.5-11.5-42 mol%). It and its ternary system are also of interest primarily for secondary coolant applications due to its low viscosity, high stability, and good thermal conductivity. It has also been considered as a fissile salt carrier due to the high solubility of the fissile salts. [11, 14]

More recently, fast-neutron reactors or fast-spectrum reactors have gained traction, and typically use chloride salts as the primary and secondary coolant materials. These salts have been identified as having properties that are better suited for the fast-neutron environment. These salts are generally easier to study because of their lower melting point and lower reactivity. As a result, there is more flexibility in measurement techniques that can be applied to measuring several salts of interest. [8]

1.3. Importance of Thermophysical Properties in Molten Salts

Like any working fluid, molten salts are selected for specific technologies based on desired thermophysical properties. In most cases, properties desired for MSR technology include high heat capacity, high thermal conductivity, low viscosity, high diffusion, and low melting point among others. [7] For molten salts, these properties are less understood than typical working fluids due to lack of available data, as most of it has been collected in academic or research settings. To select optimal materials and create applicable system designs, a more thorough understanding of their thermophysical properties is required.

There is also a deeper understanding of the salt behavior and structure that can be interpreted from thermophysical properties by studying them as a function of temperature. Together with other techniques, such as molecular dynamics modeling and x-ray characterization methods such as x-ray scattering or absorption analysis, a complete map of the salt can be developed. Changes in structure can be correlated with changes in properties as a function of temperature to learn about the speciation and material behavior. This helps to provide better understanding of the mechanisms within the salt

that may make it optimal for certain technologies. Specific to MSR, this can be associated to fissile material interactions with the bulk carrier salt that are critical to operational success and stability of the reactor. Additionally, this information can help to solve issues with the MSR systems, such as corrosion of vessels and piping and improving the fuel-salt lifecycle for recycling spent salt. [7, 15]

As a result, NEUP/DOE have expressed research interest in molten salt research, with one focus being on thermophysical properties for salts specific to MSR applications. [15] The importance of several fundamental properties of interest for molten salts is described in the following sections.

1.3.1. Density

A fundamental material property, density is key for any molten salt system from a fluid system standpoint. In any thermally cycled molten salt systems like MSRs, the liquid density will vary with temperature, which is important for understanding operating conditions within the working fluids because density will vary as heat is exchanged within the fluid. Therefore, Salts with low variability in density over operational temperature ranges would be considered favorable.

Additionally, the density's correlation with structure can be easily identified by its relationship with volume. Based on volume, atomic spacing can be determined. Notably, this property is key for developing accurate MD modeling by looking at structural aspects based on this relationship. [16, 17, 18, 19] Atomic spacing also can correlate to ionic transport properties, is associated with diffusion, and can equate to fissile material density within a working fluid within the reactor. Almost every aspect of molten salt behavior

from a mechanical and materials perspective requires an accurate density measurement, hence, making it a fundamental property of the system.

1.3.2. Viscosity

Viscosity (μ) plays a key role in molten salt behavior, especially for MSR systems. Viscosity is a bulk property that is defined as a fluid's resistance to flow. From a mechanical standpoint, it plays a key role in fluid system modeling and design, for dynamic systems like MSRs. In other technologies, such as molten salt batteries this may not be as relevant if the intent is to only be used for thermal storage. In these cases, as well as MSR, this property can also be used to understand material dynamics and structure. Coordination numbers (CN), or the probability of finding an atom of one element near or around another can be one easy way to identify this relationship. For most salts, coordination numbers between the largest cation and the salt's anion would typically be the dominant relationship when connecting the change of structure and the change of viscosity. This is likely going to be the strongest bond in the system, and therefore correlates the most with the resistance to flow. [20, 21]

In addition, as a representation of thermodynamic transport properties, viscosity can be related to diffusion (D) of ionic species by equations such as the Stokes-Einstein-Sutherland Equation (1) which defines diffusion as a function of molecular radius (r), temperature (T) and the Boltzmann constant k_B . As temperature increases and viscosity decreases, diffusion would be expected to increase (1). [22, 23]

$$(1) D = \frac{k_B T}{6\pi\mu r}$$

Other relationships, such as the Green-Kubo Equation for viscosity (2) can provide additional insight into the interactions of atomic species by simulating viscous behavior by a shearing event through the consideration of momentum (P) as a function of time (t), volume (V) at a particular temperature (T) and the Boltzmann Constant (k_b) as in Equation (2). MD modeling and analysis with this equation can therefore provide additional information on intermolecular interactions within the salt and how the liquid structure might deform from agitation within the fluid. In this situation, experimental results would be an ideal verification of model accuracy. [17, 24]

$$(2) \mu_{shear} = \frac{V}{k_b T} \int_0^{\infty} \langle P_{\alpha\beta}(t) \cdot P_{\alpha\beta}(0) \rangle dt$$

1.3.3. Surface Tension

Surface Tension, or surface energy, is a measure of intermolecular forces over a given surface area of a fluid. As such, it corresponds to intermolecular interactions within the salt at a particular interface. In molten salt systems this correlates to surface forces present at surface interfaces of pipes and vessels in flowing salt systems. These forces can vary between static and dynamic applications, and therefore result in variations between static and dynamic surface tensions values.

Static surface tensions may be more applicable for systems such as molten salt batteries, or metal purification processes, where the fluid is not flowing as readily. In some parts of MSR systems such as the main reactor vessel, which would have minimal flow of the primary salt such behavior may also be present. Dynamic surface tension may be more applicable to other components such as piping surfaces and pump components

within MSR systems. Even so, this property is of lesser interest in molten salt selection for MSRs. [12]

From literature review, surface tension's importance is primarily associated with determination of other thermophysical properties, such as density and viscosity, depending on the measurement method used. Methods for density and viscosity measurements such as the Archimedes method for density and the rotational viscometer for viscosity are both typically effected by surface tension conditions (static versus dynamic). [12, 25]

1.3.4. Other MSR Salt Thermophysical Properties

An understanding of the previously mentioned properties is typically required to measure additional properties such as thermal conductivity, heat capacity, volatility and electrical conductivity. For example, methods for electrical conductivity would be easily affected by surface tension due to changes in surface area due to capillary effects. Wetting on electrode surfaces may also affect these results if inadequate electrical contact is made, increasing resistance. This enforces the need to measure all applicable properties with salts produces under the same procedural conditions.

Research on these properties is largely presented as independent studies of specific material properties depending on research focus of the group. This is in part because many properties are often considered interdependent when taking such measurements and require each to be uniquely identified to obtain an accurate measurement. Corrections are often based on research of specific properties from other research groups, but due to variability in available measurements of such properties, this

can lead to additional error. Rose [26, 27] has identified that procedural variation in sample preparation and measurement techniques can lead to much of this difference. Therefore, measuring several material properties under the same procedural guidelines would result in the most consistent measurements when determining properties and developing a structure-property relationship through experimentation.

1.4. Research Scope

Due to the need for a thorough understanding of molten salt material measurements, this work aimed to improve fluid property measurement techniques for measuring thermophysical properties of high temperature materials. The high measurement rate methods selected measured viscosity, density, and surface tension of samples produced under the same procedure in parallel to studies. These experiments were done as a function of temperature to additionally correlate the change in property values to structural analysis of the molten salts through x-ray and MD techniques as part of parallel and future work. The main objectives of the work here-in include:

1. The design and implementation of a falling ball viscometer for high temperature measurements.
2. The implementation of maximum bubble pressure for the combined measurement of density and surface tension of volatile and reactive materials.
3. The characterization of salt samples using several material characterization methods to identify impurities present before and after employing measurement techniques 1 & 2.

This dissertation will be divided into 5 additional sections. Section 2 will provide an overview of published literature on property measurement techniques applied to

molten salt with a focus on salts explored for MSR technologies. Section 3 describes the general characterization, processing, and handling of candidate molten salts used in this work. This will include the techniques and lessons learned during sample preparation for both property measurements and x-ray experiments that were performed in parallel to this work. Section 4 will discuss the application of the maximum bubble pressure method for tandem measurements of surface tension and density. Section 5 will discuss the design and implementation of the falling ball viscometer for application with molten salts for MSR applications. Characterizations and results specific to each property measurement will be described in each applicable section. Section 6 summarizes the findings. Measurements and work herein were conducted on NaF-ZrF₄ (53-47 mol%) as a surrogate for the NaF-ZrF₄-UF₄ (53-41-6 mol%) and the LiF-NaF-KF eutectic (46-11.5-42.5 mol%). From here-on each salt will be referred to as NaF-ZrF₄ and FLiNaK respectively.

2. OVERVIEW OF EXISTING MEASUREMENT TECHNIQUES

This section summarizes several of the methods that have been utilized to measure molten salt thermophysical properties up until this point. While there are other methods used across many different salts, this mainly focuses on the studies conducted on MSR salts, particularly FLiNaK and the NaF-ZrF₄ system. The methods described herein are identified as being most frequently used for high temperature applications or are the most relevant to the work presented herein. A further comparison of relevant methods is provided in later sections in context of the measurement methods utilized in this work.

2.1. Density Methods

The overwhelming majority of reports on density measurements for molten salts have used the Archimedes method [26, 27, 28], often referred to as the bob or pendent method. A diagram of an example setup is provided in Figure 2.1. This method leverages the Archimedes principle by evaluating the force balance between buoyancy force caused by displaced fluid and gravitational force of a mass as described by Equation 2.1. This is experimentally represented by the difference in observed mass of a non-submerged and submerged pendent (Δm) and the displaced volume of the fluid based on the volume of the bob (V), corrected for thermal expansion. A surface tension (σ) correction term can also be applied to account for some of the variation in mass, although depending on the wire diameter this is often considered negligible. [29]

$$(2.1) \rho_f(T) = \frac{\Delta m + \frac{\pi D \sigma}{g}}{V[1 + \alpha T]^3}$$

Δm → difference in measured mass

D → bob diameter (corrected for thermal expansion)

σ → static surface tension

V → Bob volume

α → thermal expansion coefficient

T → Temperature

ρ_f → Fluid density

g → gravitational acceleration

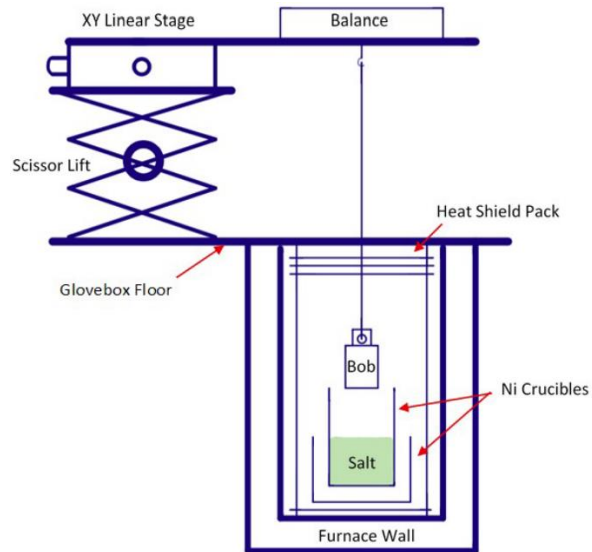


Figure 2.1: Diagram of the Archimedes method as developed by Argonne National Lab for measuring density of molten fluoride and chloride salts for MSR applications. [27]

A few additional studies have used the alternative maximum bubble pressure method for various salts, not necessarily specific to MSR applications [30]. The maximum bubble pressure method is described in further detail in Sections 2.3. and 4.

2.2. Viscosity Methods

Viscosity (μ) of molten salts have been measured by several methods, most notably the rotational rheometer [26, 27, 31] and oscillatory damped viscometer [32, 33]. More recently, rolling ball viscometers have been used to measure viscosity of molten chloride systems [34]. All these methods measure resistance or drag force due to viscous effects, as represented in the Navier-Stokes Equations (2.2). Each effectively uses a different mechanism to observe this force.

$$(2.2) \rho \frac{D\bar{u}}{Dt} = -\nabla P + \mu \nabla^2 \bar{u} + \rho F_E$$

$\rho \rightarrow$ density

$\bar{u} \rightarrow$ velocity gradient

$P \rightarrow$ Pressure

$F_E \rightarrow$ External Force

$t \rightarrow$ time

The rotational rheometer, depicted in Figure 2.2, measures the shear load (τ) on a rotating spindle at a given shear rate (ω) (Equation 2.3). It is a density independent measurement but requires surface tension corrections and several measurements at different shear rates. Shear rates must be applied such that Reynolds Number remains in the laminar region (typically $Re < 60$) to ensure viscous terms dominate the measurable force. This method has been used repeatedly for measuring FLiNaK and originally for NaF-ZrF₄. [27, 34]

$$(2.3) \mu = \frac{\tau}{\dot{\gamma}}$$

$\mu \rightarrow$ viscosity

$\tau \rightarrow$ shear stress

$\dot{\gamma} \rightarrow$ shear rate

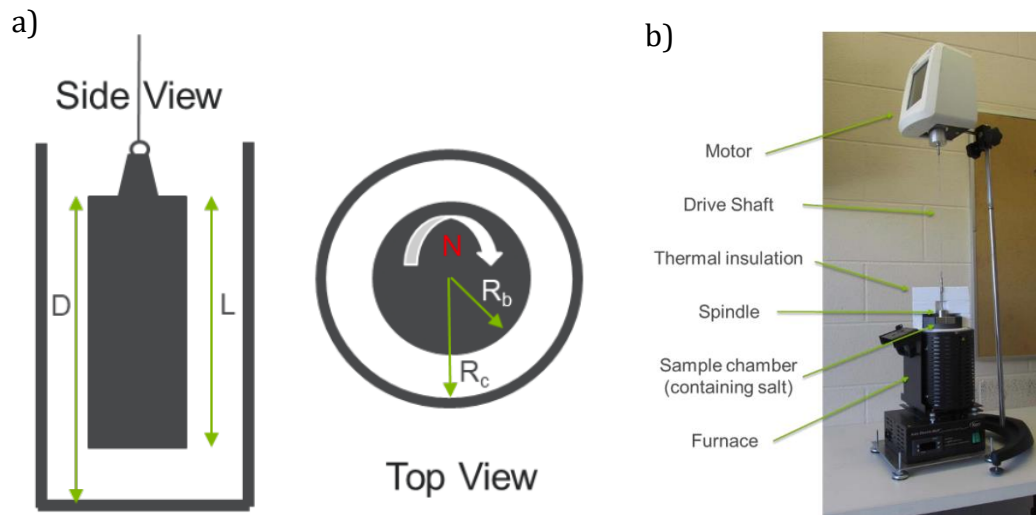


Figure 2.2: The internal diagram (a) and (b) the modified furnace setup and Brookfield rheometer as developed by Argonne National Lab for measurement of molten salts fluoride and chloride salts for MSR applications. [26]

The oscillating damped viscometer, depicted in Figure 2.3, has a much more complex process for analysis due to the need to solve for a numerical constant (x) based on oscillation frequency and dimensional constraints, ultimately resulting in a relationship dependent on density. (2.4) Additional thermal considerations therein are also harder to compensate for, such as additional friction due to differences in thermal expansion. [35] The oscillating damped viscometer has similar Re requirements to the rotational viscometer. This method has been applied on FLiNaK using a procedure that presumably does not require calibration. [36]

$$(2.4)\mu = \frac{2\pi\rho_f R^2}{T_f x^2}$$

$T_f \rightarrow$ Period

$\rho_f \rightarrow$ Fluid density

$g \rightarrow$ gravitational acceleration

$\mu \rightarrow$ *viscosity*

$x \rightarrow$ *numerical constant*

$R \rightarrow$ *cylinder or cup radius*

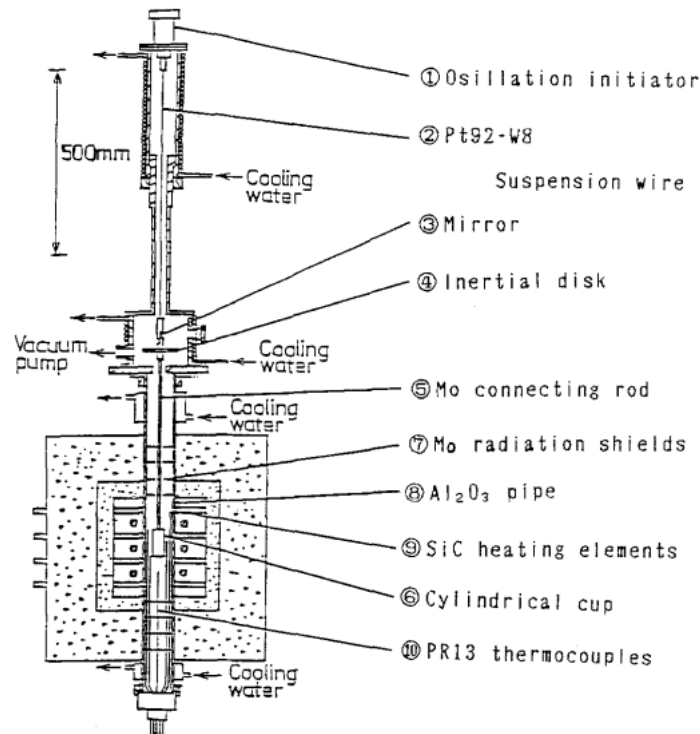


Figure 2.3: The high temperature oscillating cup rheometer method as described by Ito to measure molten NaCl. [32]

Lastly, the rolling ball viscometer [34], depicted in Figure 2.4, utilizes Stokes-Law (Equation 2.5), an evaluation of drag force on the surface of a sphere of radius r_s at low flow for Reynolds number (Re) (Equation 2.6) less than 1 as caused by viscous effects in addition to buoyancy force, and gravitational acceleration to establish a relationship with viscosity. (Equation 2.7) Here the hydraulic diameter of the Reynolds number is described as the diameter of the sphere (D_s). This relationship suggests the terminal velocity (v_z) is correlated to viscosity based on the density difference between the sphere (ρ_s) and the fluid (ρ_f) under gravitational acceleration (g). Additional corrections to account for higher range Re numbers can be accounted for through experimental or analytical determinations of a correction factor k . Reynolds number can

also be controlled by adjusting the tube angle (θ) for slower vertical velocity, and therefore allows for reasonable control over which Re regimes are observed. No reports of this method being applied to FLiNaK or NaF-ZrF₄ are known. These same principles apply to the falling ball viscometer, where θ is 90 degrees such that the ball is no longer rolling along the tube.

$$(2.5) F_{drag} = 6\pi r_s \mu v$$

$$(2.6) Re = \frac{\rho_f v_z D_s}{\mu}$$

$$(2.7) \mu = \frac{2}{9} \frac{g r_s^2 (\rho_s - \rho_f)}{v_z} k \sin \theta$$

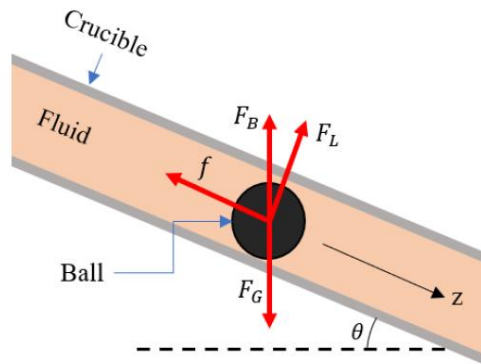


Figure 2.4: Conceptual diagram of the rolling ball viscometer showing the breakdown of applicable forces as described by Biiri, where F_G is the gravitational force, F_L is the lift force, F_B is the buoyancy force and f is the drag force. [34]

2.3. Surface Tension Methods

Surface tension methods observe interfacial interactions by either measuring the contact angle between a solid surface and a fluid or determining the maximum force such an interface can withstand before yielding. [37] Because measurement of contact angles at high temperatures can be difficult due to limited observation ability, a literature search

has found that these methods are not often selected for molten salt study. Contact angle can also change with solid surface material and surface roughness, requiring specific relationships of given materials. Therefore, methods that look at maximum force are optimal for molten salts, although in some cases the following methods described can still depend on contact angle or include contact angle as a source of error which can be corrected. [38, 39]

Additionally, a distinction must be made between static and dynamic surface tension. Typically, methods only provide one or the other with some allowing for procedural adaptations to obtain both. Further, some studies of other properties, such as density, utilize dynamic surface tension measurements in lieu of static surface tension when appropriate measurements are not available. [25] Sometimes, surface tension measurements are performed under very low shear rates to represent static surface tension, but this has not always been taken into consideration across reported results and is not an exact substitute for an actual static measurement. In general, very few studies of surface tension have been conducted on MSR salts since initial experiments were conducted between the 1960s to the 1980s. [11] Those that have been done were typically limited to select salt systems and measurement techniques.

The first identified approach for determining surface tension on molten salts was the Wilhelmy Slide Plate method, involving measuring the force by weight of the plate at the point where the fluid and plate separate as the plate is removed from the fluid (typically by lowering the salt). (8) After initial introduction of this method on halide systems there are few identified studies using molten salts. Different adaptations of this

method can provide either static or dynamic surface tension values. Additionally, the plate can be replaced with other shapes as necessary, such as cylinders or pins, but similar procedures tend to produce similar results. [39] This includes methods, such as the “pin” or “rod” methods that are realistically derived from the Wilhelm plate method and have been occasionally used for some studies on molten salts. [40]

One method that falls into the middle ground between contact angle and force balance methods is the pendant drop approach, requiring specialized furnace systems to create an observable hanging droplet. Here surface tension is determined based on the shape of the droplet. This method has been applied for a few limited molten salts [41], but not NaF-ZrF₄ or FLiNaK. Additionally, it has been used for several molten alloys, demonstrating success at high temperatures. [42] At room temperature, this method has also been used for determining density [43], but no studies have been found using molten salts. In general, this method is not ideal to for high temperature measurements due to the high surface area exposure of reactive materials.

The most common approach for measuring surface tension is the maximum bubble pressure method. This method observes the pressure during the formation of a bubble attached to the end of a capillary to determine the surface tension. As mentioned in Section 2.1. this method can also be used to determine the density of the fluid. This method is the most common because it is generally easy to adapt to high temperature applications and has no direct dependency on contact angle. While this method is a dynamic method, much of the literature for molten salts utilizes this method to represent static behavior with low flow rates, or the resultant reports does not comment on this

distinction except for Rose et al. [26, 27] It has been suggested in using this approach that the gas flow associated with bubble formation should be kept as low as possible to reflect static surface tension behavior. Further details on this method as used in this work are described in Section 4. This is the only known method identified for measuring surface tension of FLiNaK and NaF-ZrF₄.

3. MATERIALS PROCESSING, HANDLING AND CHARACTERIZATION

Prior to taking any measurements, procedures were established and verified to produce consistent samples across all property measurements. This included criteria for the experimental environment, material synthesis, and characterization methods and techniques for prevention and identification of impurities. Characterization techniques included visual inspections, Scanning Electron Microscopy (SEM) with Energy Dispersive X-ray Spectroscopy (EDS), X-ray Powder Diffraction (XRD), Digital Scanning Calorimetry (DSC), Thermogravimetric Analysis (TGA), Inductively Coupled Plasma Optical Emission Spectroscopy (ICP-OES) and Ion Selective Electrode (ISE) analysis for fluoride measurements. Methods established during this work were based on procedures established in published studies and in-house experimental findings as described herein. Parallel studies for establishing handling procedures associated with experiments for x-ray measurement techniques provided additional information and ability to explore the necessary standards required for consistent sample preparation and handling.

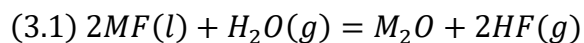
The following sections describe the possible impurities in the salts, equipment used for salt synthesis, how these impurities have been identified in salt samples with

accessible techniques and steps taken to minimize introduction of impurities. Examples are provided from sample preparation, post experiment samples, and samples of parallel x-ray measurement experiments. Additional characterization specific to each property measurement is described in their respective sections.

3.1. Molten Salt Impurities

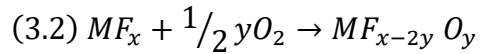
Impurities within molten salts can be introduced in several ways and have been reported in literature as part of the MSR development process. Therefore, these impurities are relatively well known within halogen salt systems, especially MSR salts. [44, 45, 46, 47] For the context of this work, only impurities associated with the salts studied will be discussed. Introduction of impurities in these cases can be classified in three general ways, due to moisture, oxygen, and/or corrosion products.

The first major impurity that can occur within molten halogen salts occurs in the presence of moisture when the salt is at elevated temperatures. A reaction occurs that produces metal oxide and hydrogen fluoride, as shown in Equation 3.1 where M is the cation metal. The metal oxide can either precipitate out of the salt, as is the case with salts that contain ZrF_4 , or stay dissolved in the salt.

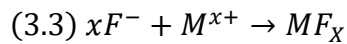


Similarly, the fluoride salts can interact with oxygen gas, however most reports suggest this does not prevent the loss of fluorine in the system as HF cannot form without the presence of hydrogen. Additionally, the formation of other species is not favored. Cases such as this are likely to produce a metal oxyfluoride, as expressed by Equation 3.2. Based on the quantity of oxygen present and salt being considered, the oxygen

content may be low enough such that the impurity stays dissolved in the molten salt. In some cases, such as with ZrF_4 , if oxygen content is high, a high percentage oxygen oxyfluoride can form and precipitate from the system removing the fluoride and cation from the melt. [48, 49, 50] Examples of identified oxyfluoride species are provided in Section 3.4.3.



The last major source for impurities within the salt can come from corrosion products that may form due to contact with other substances, such as Equation 3.3. Many studies have investigated this interaction as it remains a problem for many molten salt technologies. Some literature focuses on this occurrence as a basic diffusion of metal ions into the salt. Others have observed the corrosion is accelerated in the presence of oxygen or from the HF byproduct from the reaction with moisture. The former can cause the formation of metal oxides on a vessel surface that may dissolve into the molten salt more readily and the latter can directly corrode the metal creating additional fluoride species. [11, 51, 52, 53]



3.2. Experimental Environment

Due to sensitivity with moisture and oxygen as described in Section 3.1, molten fluoride salts require dry oxygen-free gas environments. Therefore, either an adequate glove box or sealable vessel is required. In association with this work, the first has been used for salt preparation, synthesis, and property measurements. The latter was employed

for the collaborative work with x-ray measurements. Each environment must have the capability to reach temperatures well above the melting point of the salt used.

Customized furnaces were developed to accommodate both environments due to the unique requirements for the respective experiments performed. The details of these furnaces are described in the following sections.

Information associated with x-ray measurement techniques is being included in this work because several findings were observed during the development process that were critical to the understanding of the interactions between the salts, oxygen and moisture that may have otherwise not been characterized. In addition, the design and implementation of several heating devices exhibit the importance of rectifying procedural differences between several measurement techniques that can lead to sample variation. [26, 27, 47]

3.2.1. Glove Box Testing Environment

For sample preparation and measurement of thermophysical properties, a glove box capable of maintaining less than 1ppm oxygen level and moisture was used (LCPW-125). A small form-factor glove box with a limited space of 86cm wide, 61cm deep, and 76cm, high was used for sample preparation and experiments. To fit in this limited space, a small furnace was designed and built for sample synthesis and property measurements . The requirements of the furnace are predominantly based on the requirements for the thermophysical property measurements, but also include considerations for protecting the glove box operation and user safety. The requirements are:

- a. Ability to reach a temperature of 800 °C or higher.

- b. High thermal stability when holding temperature with little temperature variation across the sampling region.
- c. Well contained thermal output minimizing the amount of heat loss into the glove box to protect temperature sensitive components, which applies to user safety.
- d. Easy disassembly within the glove box for cleaning and maintenance.
- e. A vertical heating zone capable of melting a column of salt at least 4 inches high.
- f. Easy access for loading/unloading of samples.
- g. Fitting within the confines of the small form factor glove box.

Based on these requirements, the dimensions of the furnace were defined to be a 28cm cube, raised slightly off the bottom of the glove box. Insulation bricks with a cylindrical cavity were inserted into a steel framework. The cavity was fitted with a custom heating element. The heating element was made from Kanthal wire, shaped around a cylindrical mold such that the wire is divided into two sets of semicircular windings to reduce electromagnetic interference that the heating element may cause if wound in a spiral. A thermocouple to control the temperature was inserted through the side wall of the furnace. A diagram of the furnace is shown in Figure 3.1, with the glove box and furnace shown in Figure 3.2. The heating element is shown in Figure 3.3.

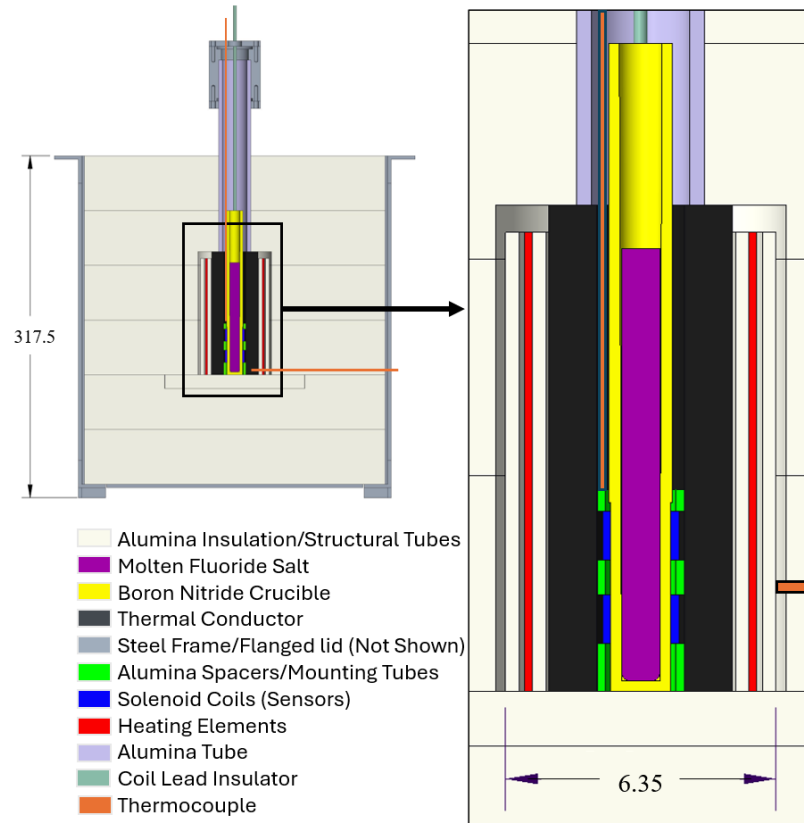


Figure 3.1: Schematic of the Glove box furnace with staged components for viscosity measurement (as described in Section 4).

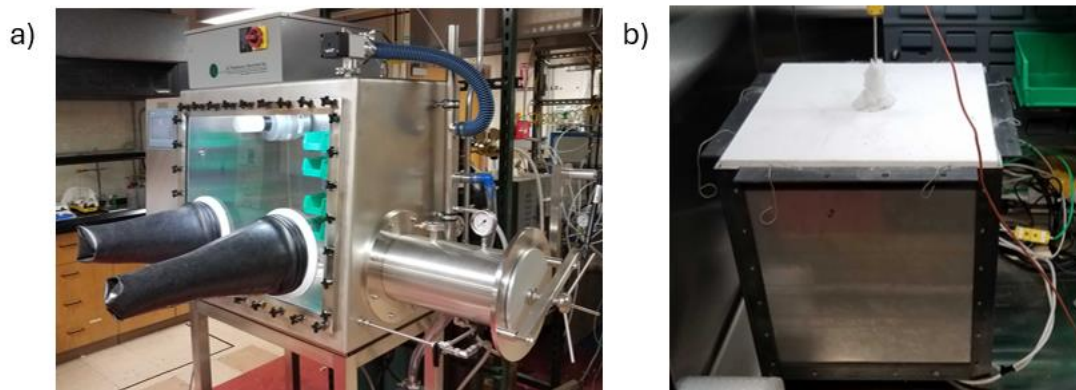


Figure 3.2: Image of the glove box and assembled furnace when first installed.

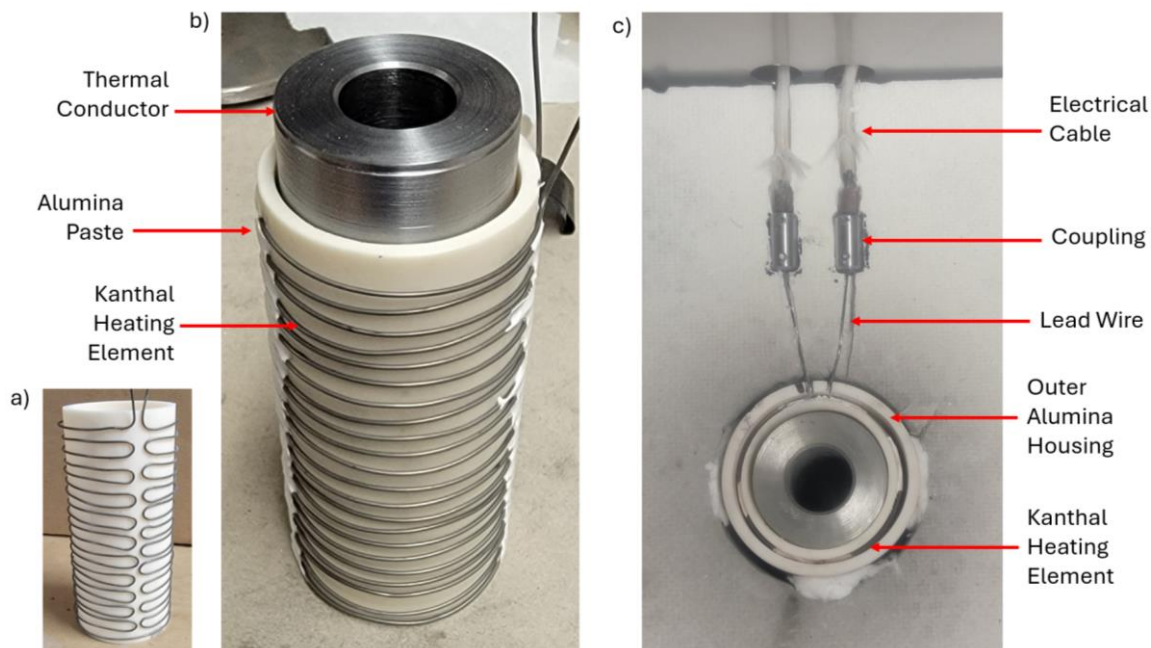


Figure 3.3: The custom heating element for the glove box furnace. a) Depicts the heating element after the Kanthal wire is wrapped and annealed at 1200 °C. b) The wire is then pasted to the alumina tube, and a steel thermal conductor inserted inside. c) The heating element is then installed into the furnace with steel couplings were used to attach the exposed ends of the Kandhal wire (leads) to electrical cables. An outer Alumina tube housing is used to help to support and protect the heating element.

3.2.2. X-Ray Measurement Sample Holder Designs

Sample handling of X-Ray samples and associated furnace design had different requirements than the glove box testing environment. Two different sample holder and heating devices were designed for the Pair Distribution Function (PDF) experiments performed on both salts and the combined Near Edge X-Ray Absorption Fine Structure (EXAFS), and Near Edge X-Ray Absorption Fine Structure (XANES) experiments performed on NaF-ZrF₄. Considerations of the glove box furnace (a) through (d) remained the same with the following additions:

- h. A clear path for x-ray beam to the sample with no obstructions that are not x-ray transparent.

- i. Small but consistent heating zone with accurate temperature measurement at the exposed surfaces
- j. Physically stable structures that will not move during heating.
- k. Be able to establish similar environmental control as the glove box (low oxygen and moisture, 1ppm or less), but without the continuous gas cleaning capability that the glove box provides.

For PDF experiments, a cylindrical holder was developed that could house a small cylindrical glassy carbon crucible, where a schematic and images are provided in Figure 3.4. This holder consists of a 3D printed cylindrical ceramic base that has internal features which allowed for the glassy carbon crucible to sit inside. Two through holes are added to the cylindrical wall in the radial direction, the first for locating a thermocouple at the wall of the glassy carbon crucible. The second lower through hole, which goes through both walls, was for the path of the x-ray beam. The ceramic holder was then held in place with an additional through hole at the bottom, where a pin can be inserted to fix the holder inside a supporting cup. A Kanthal heating wire was wrapped around the top portion of the ceramic holder, leaving the through-holes exposed. The wire was pasted in place with Alumina Paste (AREMCO Ceramabond 552-VFG). Salt, prepared as described in Section 3.2, was melted into the crucible inside the glove box in preparation for the experiment. This crucible was transferred into the x-ray chamber quickly, exposing it to air for as little time as possible, and inserted into the holder.

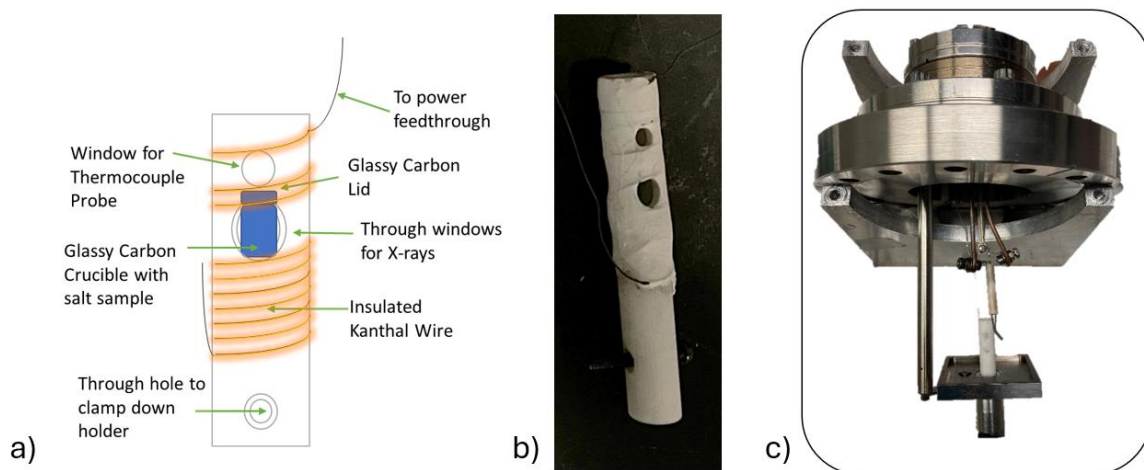


Figure 3.4 a) Diagram of heater and sample holder for glassy carbon crucible designed for PDF scattering experiments. b) The as made heating element and ceramic holder with Kanthal heating wire pasted onto the surface of the Formlabs 3D printed ceramic holder. c) The holder as mounted to the stage as it would be seen in the x-ray test chamber.

For the EXAFS/XANES experiments, which were only performed on NaF-ZrF₄ samples, a separate holder was designed, consisting of two flat plates of hexagonal boron nitride (HBN) with a thin, 100um cavity in one. An additional cavity was cut into the plates to allow the thermocouple to be inserted between them for accurate temperature measurements. These plates were sandwiched together with screws and 316 stainless-steel plates with a Kanthal wire heating element wrapped in such a way to optimize heating of the HBN plates without crossing the wire over the central cavity. A quartz paper sheet was used in between the Kanthal wire and stainless-steel plates as an electrical insulator. A sample was prepared using a mold with the same depression size as the HBN plate. The salt was crushed and melted into the depression with a weight on top to prevent the molten salt from forming as a droplet. When cooled, this formed a thin wafer of the material that would fit into the HBN depression. The sample and components were assembled inside the glove box, minimizing air exposure prior to

transferring it to the chamber. A diagram and images of the as-made holder are shown in Figure 3.5.

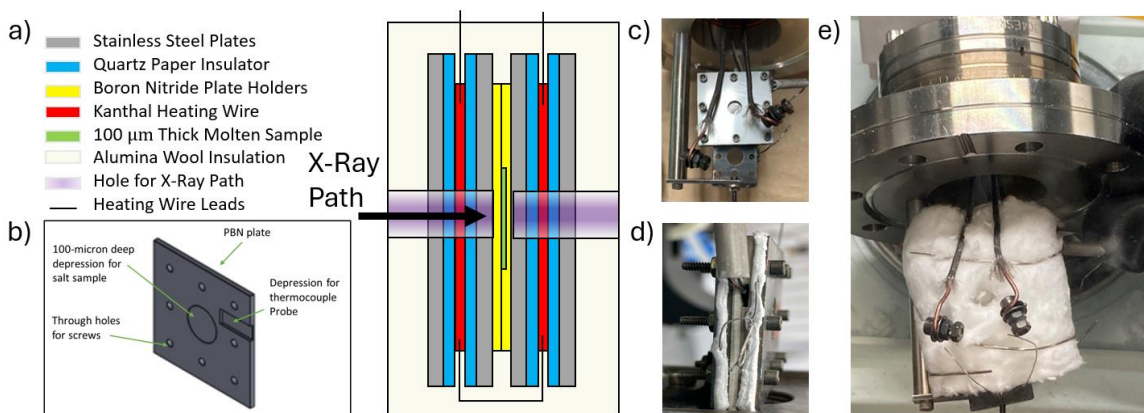


Figure 3.5: a) The EXAFS/XANES thin sample holder as assembled schematic using b) HBN plates with a 100 μm depression. The front (c) and side (d) views of the sample holder as assembled and e) the holder wrapped in Alumina Wool as attached to the stage of the x-ray test chamber.

3.3. Material Synthesis and Handling

As mentioned in Section 3.2.1, salt was synthesized in an inert environment using the glove box furnace. Relevant single-salt precursors were purchased from Sigma Aldrich as needed for production of FLiNaK and NaF-ZrF₄. Salts were prepared similarly to the procedure established by Rose et al from Argonne National Lab [26, 27] with considerations from other reports [47]. First each precursor was baked in a nickel crucible at 300 °C for 2 hours to remove moisture. Higher temperatures likely cause absorbed moisture or residual oxygen to react with the precursor salts during this process. The precursors were then weighed and mixed according to the desired weight percent and added to a cleaned nickel crucible. This crucible was loaded into the furnace, where it was baked for 2 hours at 300 °C prior to melting the salt at 50 °C to 100 °C above their respective melting points. The molten salts were held at temperature for homogenization

for 2 hours before they were cooled. Once the salt had cooled to room temperature, the salt was inspected and analyzed for compositional accuracy and consistency.

3.4. Characterization Methods, Techniques and Procedures

This section describes details of the methods, techniques and procedures used to characterize the salt samples before and after measurement. Representative results are additionally included that support the characterization of these samples.

3.4.1. Visual Inspection

As synthesized with these procedures, each salt displayed several unique characteristics that indicated impurities that could be identified by visual inspection. For most samples, this was important for the context of this work since due to limited access to ICP-OES. This reduced the ability to identify trace element impurities that are not easily identifiable with other methods.

Impurities predominantly formed in NaF-ZrF₄ included an oxide or oxyfluoride. Visual inspection of this salt identified the presence of these impurities. Figure 3.6 shows an image of such a prepared sample. The bulk of the NaF-ZrF₄ sample typically appears as a translucent, and slightly grey in color. The bottom Ni-salt interface of the as made salt sample will typically appear as a chalky grey or white. The white is indicative of the presence of ZrO₂ as produced with a reaction with H₂O. Additional black specks can be seen within the salt, particularly at the top gas-salt interface. These specs are identified as a high oxygen content phase, likely ZrO₂ or Zirconium Oxyfluoride, identified with the techniques described in the following sections.

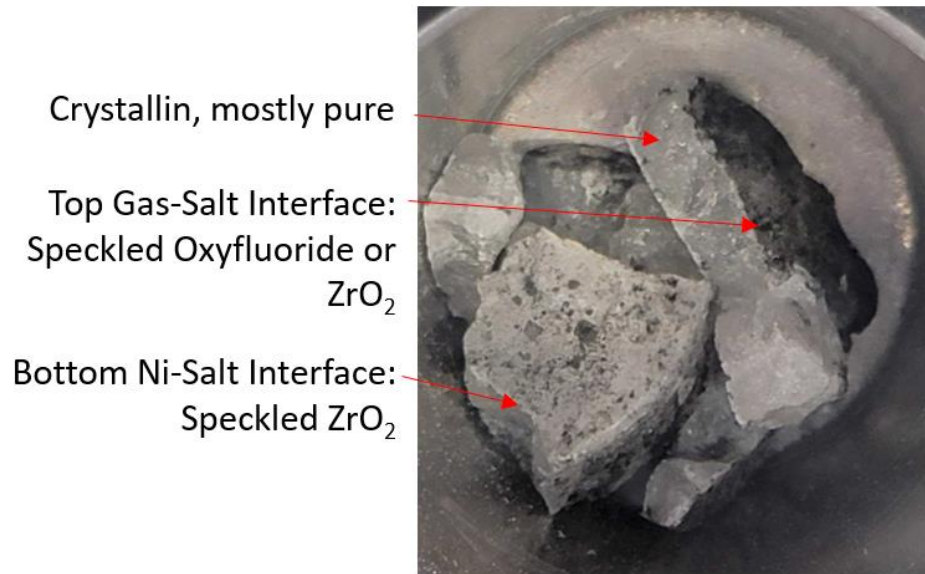


Figure 3.6: Fractured as made sample of NaF-ZrF₄ showing the top (black/gray, gas-salt) and bottom (white, Ni-salt) interfaces as observed after synthesis.

FLiNaK is typically synthesized as a white, opaque crystal. When pure, this salt shows little to no variation in color through its bulk. Impurities can be identified within the salt based on changes in coloring. Coloring can also be seen within FLiNaK where the salt appeared to take on the color of metal oxides, oxyfluoride, or fluoride corrosion products dissolved in the molten salt during experiments. With the techniques available, specific evidence could not be found to identify exactly which of these were present, but comparing colors of these presumed species and associating them to materials used provides a reasonable correlation.

Images of these FLiNaK colors are shown in Figure 3.7. Pure, as-made FLiNaK is depicted in Figure 3.7.a. FLiNaK exposed to an impure environment of oxygen and moisture takes on a pink, purple or orange-red color, is shown in Figure 3.7.b. Testing associated with this color was performed in a glassy carbon crucible (so no metal contact) in the x-ray chamber in conjunction with XRD analysis as described in Section 3.4.3.

With these results and observations of color changes as the fluoride hydrates in air (described in Section 3.4.3), the color is expected to be associated with the potassium fluoride component of FLiNaK, possibly producing oxide or hydrated KF (K_2O or $KF \cdot H_2O$). While not well recorded in published literature, this color is commonly identified in association with various impurities, usually some metal oxides. [54] These experiments clearly identified that this coloration change may not only be associated with such impurities.

Figure 3.7.c. depicts a greying of the FLiNaK during surface tension measurements using 304 Stainless Steel, likely due to the presence of metal species within the salt. The exact cause could not be determined with available techniques; however, it is likely low levels of oxygen or moisture are present since no additional fluoride compounds could be identified.

Lastly, Figure 3.7.d. shows a green-blue color sometimes observed in the salt during surface tension measurements using 300 Series Stainless Steel tubes. Corrosion of the 304 and 316 Stainless Steel tubes, described in further detail in Section 4, most likely introduced chromium species into the salt, possibly forming chromium oxide (Cr_2O_3) or chromium fluoride (CrF_3). This indicates higher levels of oxygen and moisture are present during these measurements, or such a reaction is not likely to occur in such a short period of time. In addition, this color is also occasionally identified in literature in association with various impurities observed in the salt, although ones not necessarily present in these experiments. [55]

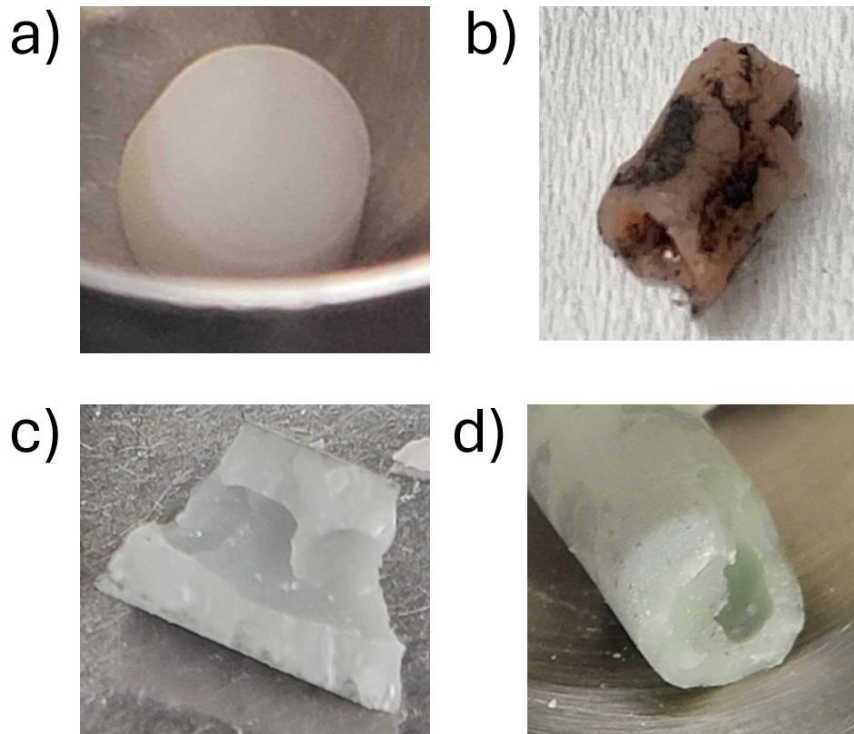


Figure 3.7: FLiNaK coloration of various salt samples as exposed to different conditions. a) An as-made sample with no impurities b) a sample exposed to an inadequate gas environment (high oxygen content). c & d) a sample tested after surface tension measurements using Stainless Steel bubbling tubes that show indication of dissolved metals, metal oxide or metal fluoride possibly due to reaction of chromium in the stainless steel with trace oxygen/moisture impurities in the glovebox.

3.4.2. Digital Scanning Calorimetry (DSC) & Thermogravimetric Analysis (TGA)

DSC analysis & TGA was performed on the salts to verify the melting points and to determine if they matched samples from other studies. Tests were performed using the TA STD Q 600 in an Argon gas environment with oxygen and moisture removed by a heated copper-copper oxide and Drierite column traps, respectively. Samples were held in platinum crucibles. For FLiNaK, similar heating procedures used for sample preparation utilizing a baking step at 300 °C were used to release any absorbed moisture. Analysis of the melting point by DSC was compared to melting points of respective compositions as provided by phase diagrams in the literature for NaF-ZrF₄ (Figure 3.8)

[56] and FLiNaK [14]. Additionally, the phase diagram for FLiNaK using the database FactSage [57] (Figure 3.9) was generated for comparison. The available data in the FactSage database or available similar databases did not include enough thermodynamic information to generate similar phase diagram of NaF-ZrF₄.

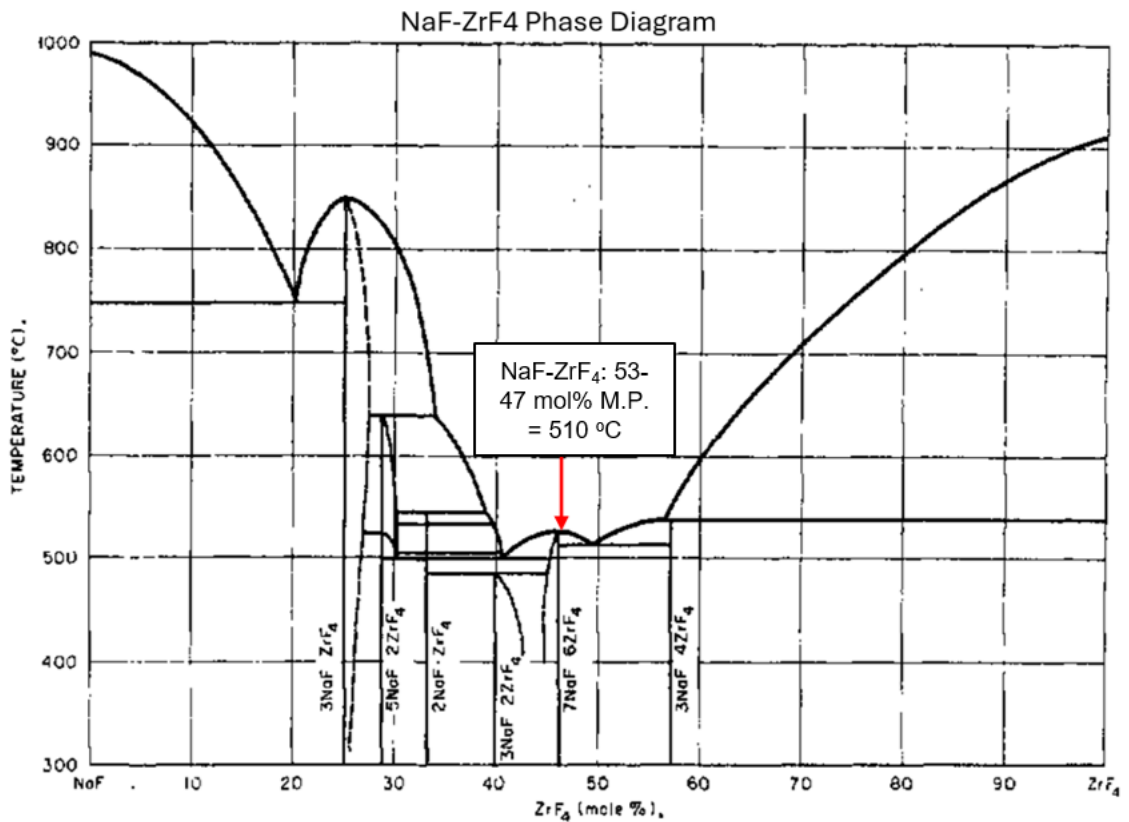


Figure 3.8: NaF-ZrF₄ phase diagram with relevant composition labeled. [56]

LiF-NaF-KF Phase Diagram

Projection (A-Salt-liquid), 1 atm

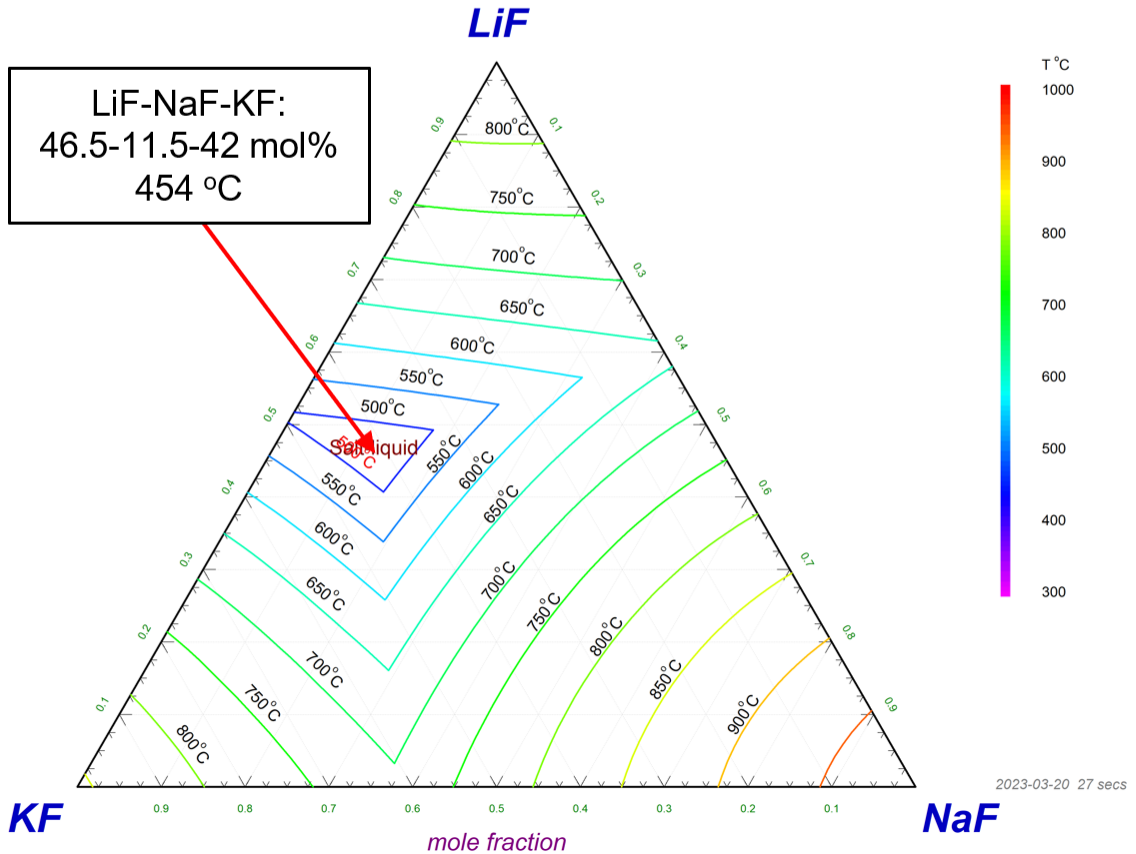


Figure 3.9: LiF-NaF-KF Phase diagram as generated using the FactSage thermodynamics database with the eutectic composition labeled.

Phase diagrams show the eutectic composition of FLiNaK has a melting point of 454 °C and NaF-ZrF₄ has a melting point of around 510 °C. This is within a reasonable margin of error as those measured by DSC analysis, with FLiNaK showing approximately 446 °C (1.76% Error) and NaF-ZrF₄ showing approximately 501 °C (1.76% Error). Full scan results are shown in Figures 3.10 and 3.11 respectively.

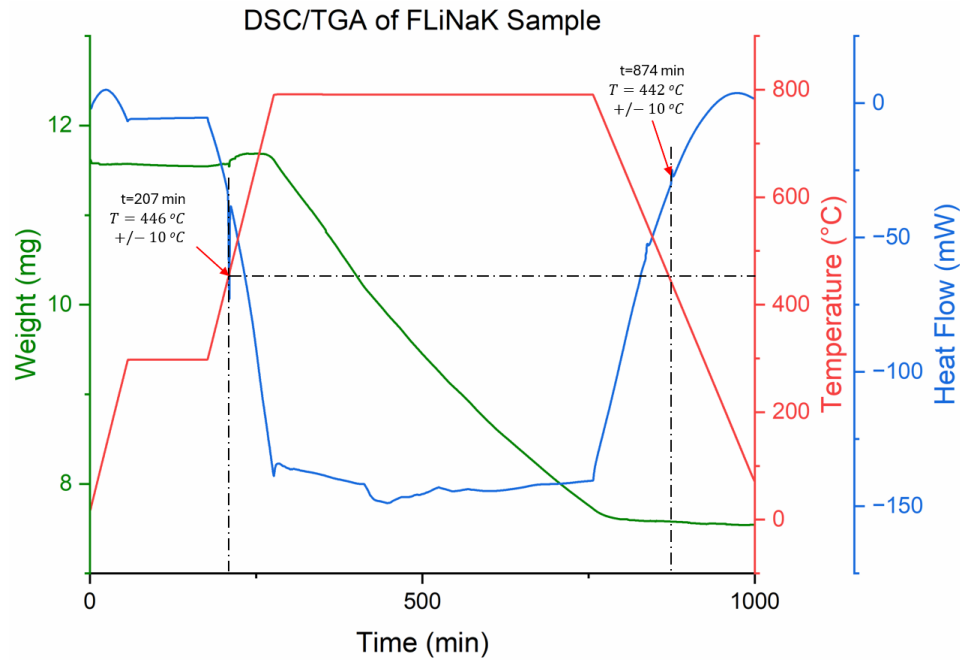


Figure 3.10: DSC/TGA of FLiNaK. Approximate melting and solidification temperatures are labeled, 446 °C and 442 °C, respectively. It is comparable to the theoretical melting point of 456 °C.

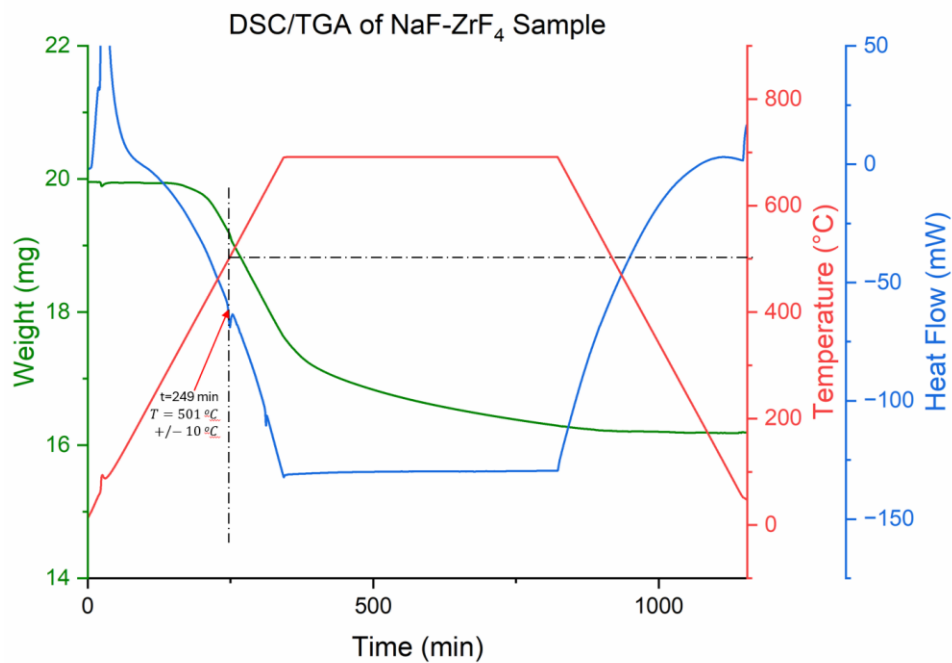


Figure 3.11: DSC/TGA Analysis of NaF-ZrF₄. Approximate melting point is 501 °C, it is comparable to the melting point identified in literature of 520 °C.

In addition to melting point, this analysis also provides some potential indications for salt volatility during the TGA measurements. As shown in Figures 3.10 and 3.11, each salt exhibits a loss of mass when held at 800 °C for FLiNaK and 700 °C for NaF-ZrF₄.

Additional testing was performed on FLiNaK to investigate the possible mass loss due to volatility as a function of temperature. The data shows an increasing trend in mass loss with an increase in temperature as shown in Figure 3.12. It is not clear if this is because of the presence of oxygen and moisture, which could be introduced by continuous gas flow, or if this is due to the formation of gaseous species from the salt. These gaseous species may also be removed by continuous gas flow. It is for this reason that gas flow was stopped when melting the salt during the x-ray measurements as described in Section 3.5. It must be noted that due to the age of the DSC/TGA instrument, some of this variation could be an effect of mass drift within the scale of the instrument, and therefore actual mass loss values may not be reliable.

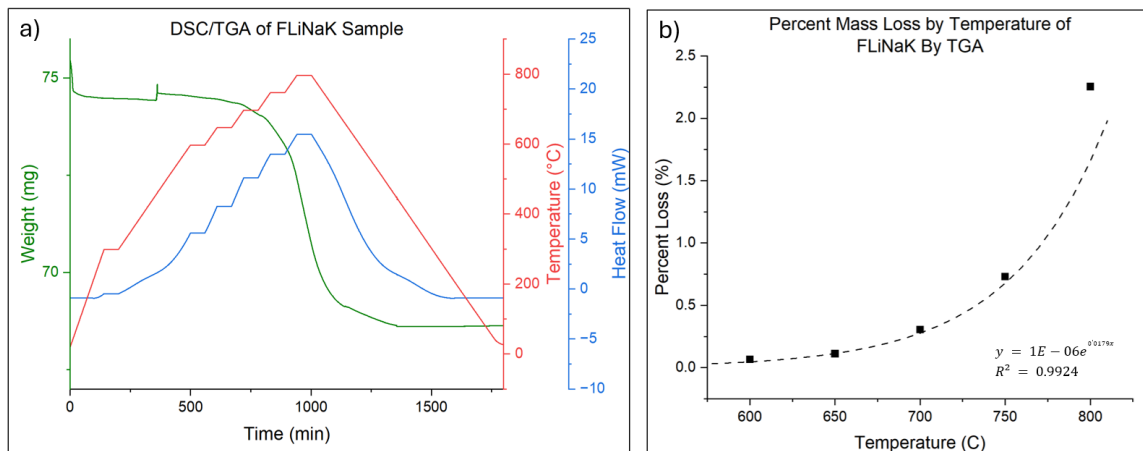


Figure 3.12: TGA mass loss data of FLiNaK as a function of temperature, where a) is the initial collected data and b) is the analyzed percentage loss at each set temperature by evaluating the slope of the weight change as a function of time.

Validation testing for the x-ray chamber on NaF-ZrF₄ shows similar behavior. In addition, similar compositions were identified to have the same behavior as reported in literature [45] [58]. As a result, specific TGA tests were not performed for this salt, however experiments with the X-Ray chamber provide examples of volatile behavior and are described in more detail in Section 3.5.

3.4.3. X-Ray Powder Diffraction (XRD)

XRD analysis of powder samples of both FLiNaK and NaF-ZrF₄ were performed on a Bruker D2 Phaser. Samples of both salts were first crushed to powder before packing them in appropriate sample holders. XRD scans were matched to documented materials in the Crystallography Open Database 2018 (COD) and PDF-2 Release 2020 RDB (PDF-2). Handling of each sample for XRD analysis had a few differences.

Because of the hygroscopic nature that FLiNaK exhibits, as depicted in Figure 3.13, the sample must be covered to prevent prolonged exposure of the salt.

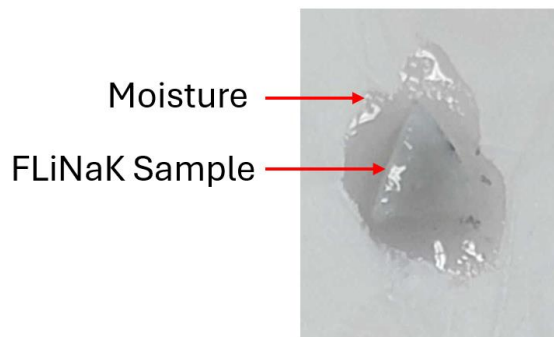


Figure 3.13: Example of hygroscopic behavior exhibited by FLiNaK when exposed to air for 5 minutes or less.

If left for 5 minutes or less, the FLiNaK powder becomes hydrated as the salt appears to partially dissolve into the water. Figure 3.14 shows example XRD samples of as-made clean FLiNaK with a plastic-domed sample holder (Figure 3.15.a), and samples

tested with Kapton over the top of the salt (Figure 3.15b, used in later measurements due to the easier removal of background in the scans and higher intensity signals from the salt). To confirm the compositional analysis of the salt, FLiNaK was compared to diffraction patterns of its precursor salts, LiF (PDF-2: 00-004-0867), NaF (PDF-2: 00-036-1455) and KF (PDF-2: 00-036-1458), as they appear to remain as separate phases when solidified. Any concentrations of impurities present in as-made salt samples were too small for the D2 Phaser's detector to provide any contribution to the diffraction pattern.

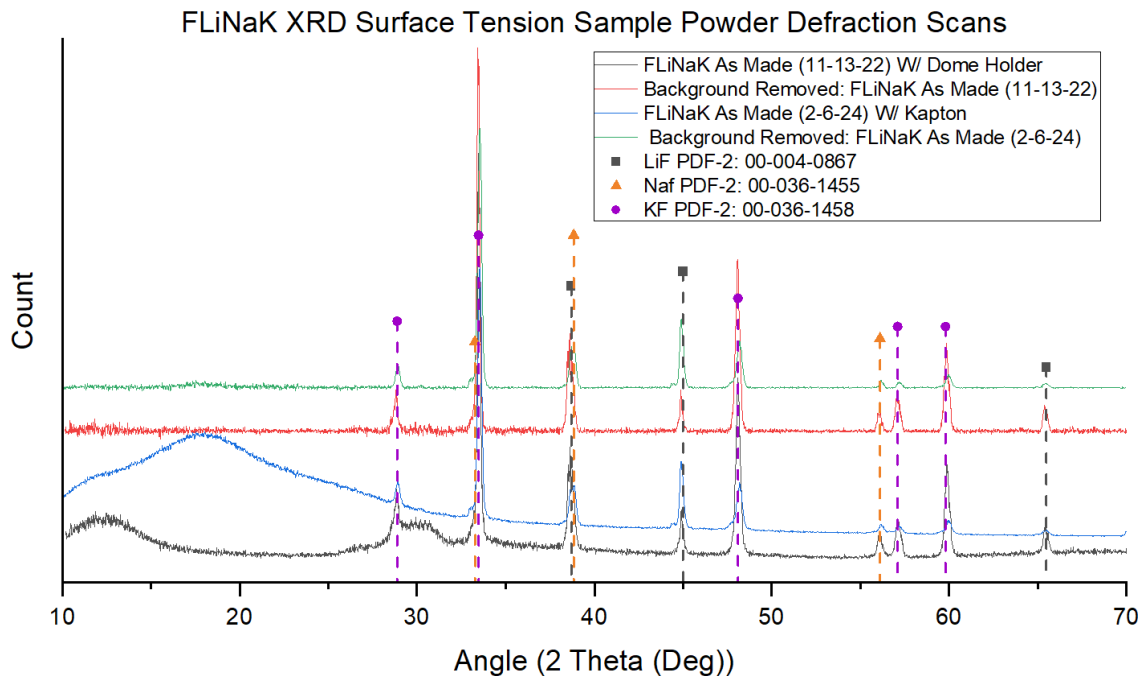


Figure 3.14: XRD diffraction patterns of as-made FLiNaK samples prepared with Domed holder as shown in Figure 3.15.a and Kapton tape as shown in Figure 3.15.b. Signals are shown with the background included and the background removed to compare the effect of each holder.

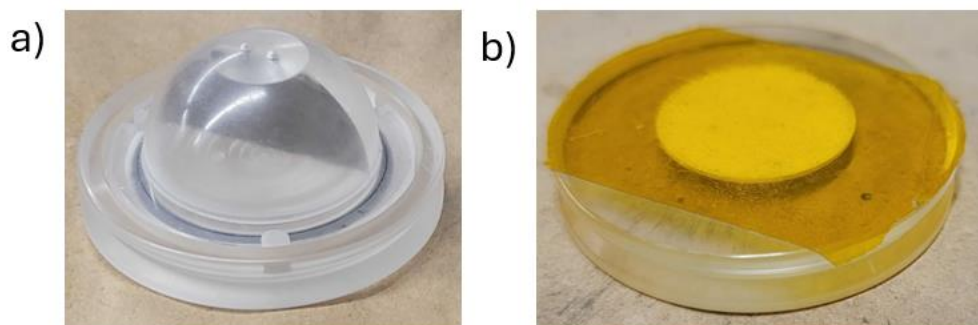


Figure 3.15: Example sample holder methods for performing FLiNaK XRD scans, a) the domed cover available from Bruker and b) a regular sample holder covered with Kapton tape.

In addition, the effect of hydration on FLiNaK can be observed by XRD, indicating how moisture may affect the salt. Figure 3.16 shows the XRD scans under various testing conditions as an example of the effect of humidification on FLiNaK in various stages of hydration. Testing conditions were determined to be based on the room's environmental humidity at the given time of testing and the duration. In these cases, the hydrated salt matches $\text{KF}\cdot\text{H}_2\text{O}$ (PDF-2: 00-32-0783), indicating the KF component of the salt is the more moisture-sensitive component within FLiNaK. If the salt becomes overly hydrated, as depicted in Figure 3.13, the moisture appears to dissolve KF out of the solid, leaving LiF and NaF behind. In these cases, if the sample starts as white, the color can temporarily change to pink, like the one shown in Figure 3.7.b., before returning to white after the salt is fully hydrated. Pink samples also lose their coloration, returning to white after they become hydrated.

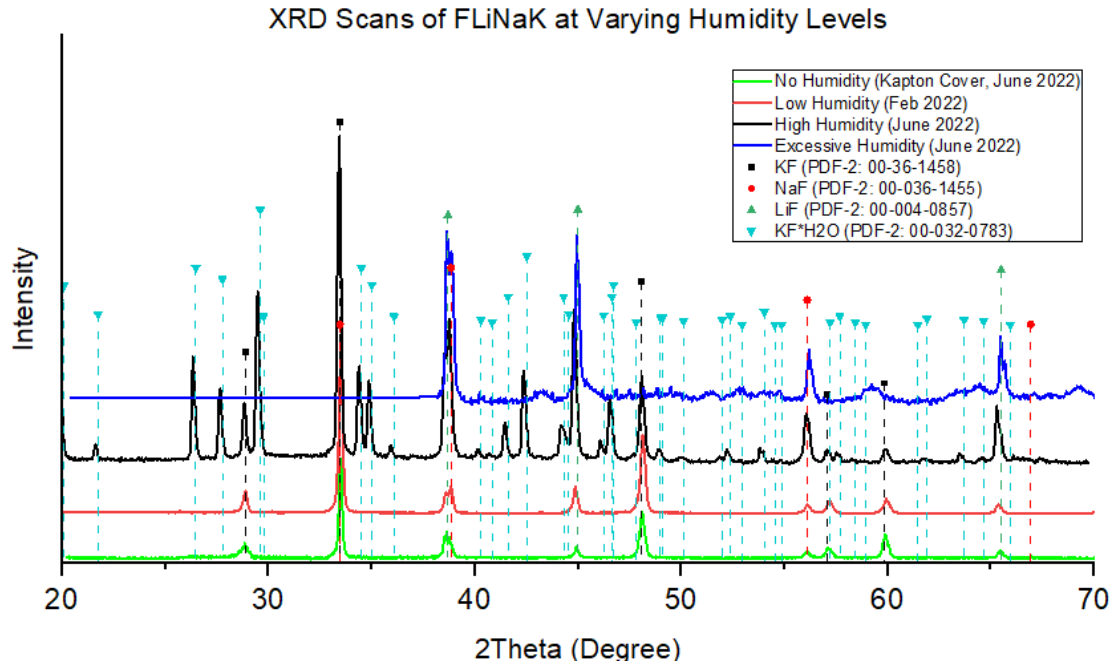


Figure 3.16: XRD scans showing the effect of hydration of FLiNaK samples as exposed to moisture in the air on days of varying humidity levels. They are compared to a sample with no humidity, sealed with a Kapton tape cover.

Samples of NaF-ZrF₄ were analyzed without protective barriers, as the salt is not as readily affected by oxygen and moisture at room temperature. XRD scans of this salt were compared to the closest composition available in accessible databases, Na₇Zr₆F₃₁ (PDF-2: 00-022-1417, 53.9-46.2 mol%). Often additional peaks of low intensity can often be observed in as-made samples. These peaks are easily identified as ZrO₂ by matching the respective diffraction pattern (PDF-2: 00-037-1484). Figure 3.17 shows an example of the diffraction pattern of as made NaF-ZrF₄ by XRD analysis with minimal ZrO₂ impurities. Impurities are additionally verified by SEM/EDS analysis as described in Section 3.4.5.

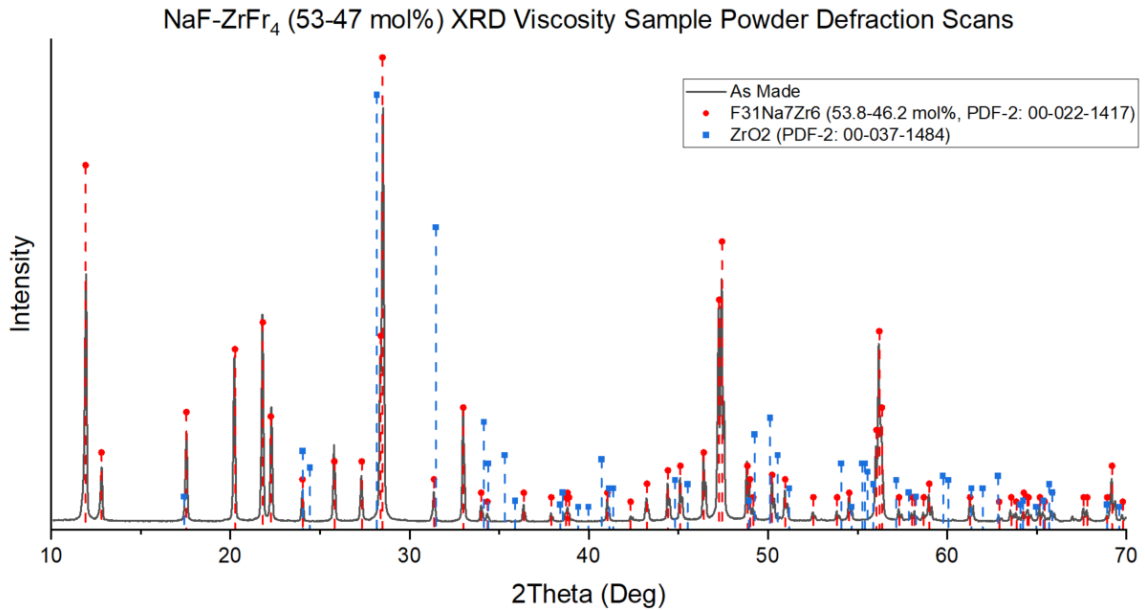


Figure 3.17: XRD diffraction patterns of NaF-ZrF₄ (53-47 mol%) with comparable PDF cards for similar composition F₃₁-Na₇-Zr₆ (53.8-46.2 mol%) and potential impurity ZrO₂. No ZrO₂ peaks are observed.

Other reaction product impurities in NaF-ZrF₄ include Oxyfluoride which has several identifiable phases depending on the oxygen concentration. Distinguishable phases in measured samples typically appear to contain higher oxygen concentrations, such as one identified (Zr₇F_{9.71}O_{8.79}, Figure 3.18.a.) in a sample from surface tension measurements described in Section 4. An additional phase has been identified after inadequate baking of precursor salts which resulted in formation of oxyfluoride (ZrF_{3.33}O_{0.33}, Figure 3.18.b.). XRD analysis of clumps formed during low temperature baking tests show distinct scattering patterns of low oxygen oxyfluoride. The presence of oxyfluoride at this stage effects the salt composition during salt synthesis. If additional oxyfluoride phases are present, low concentrations and similar scattering patterns to the base salt (NaF-ZrF₄) and ZrO₂ have made them difficult to identify.

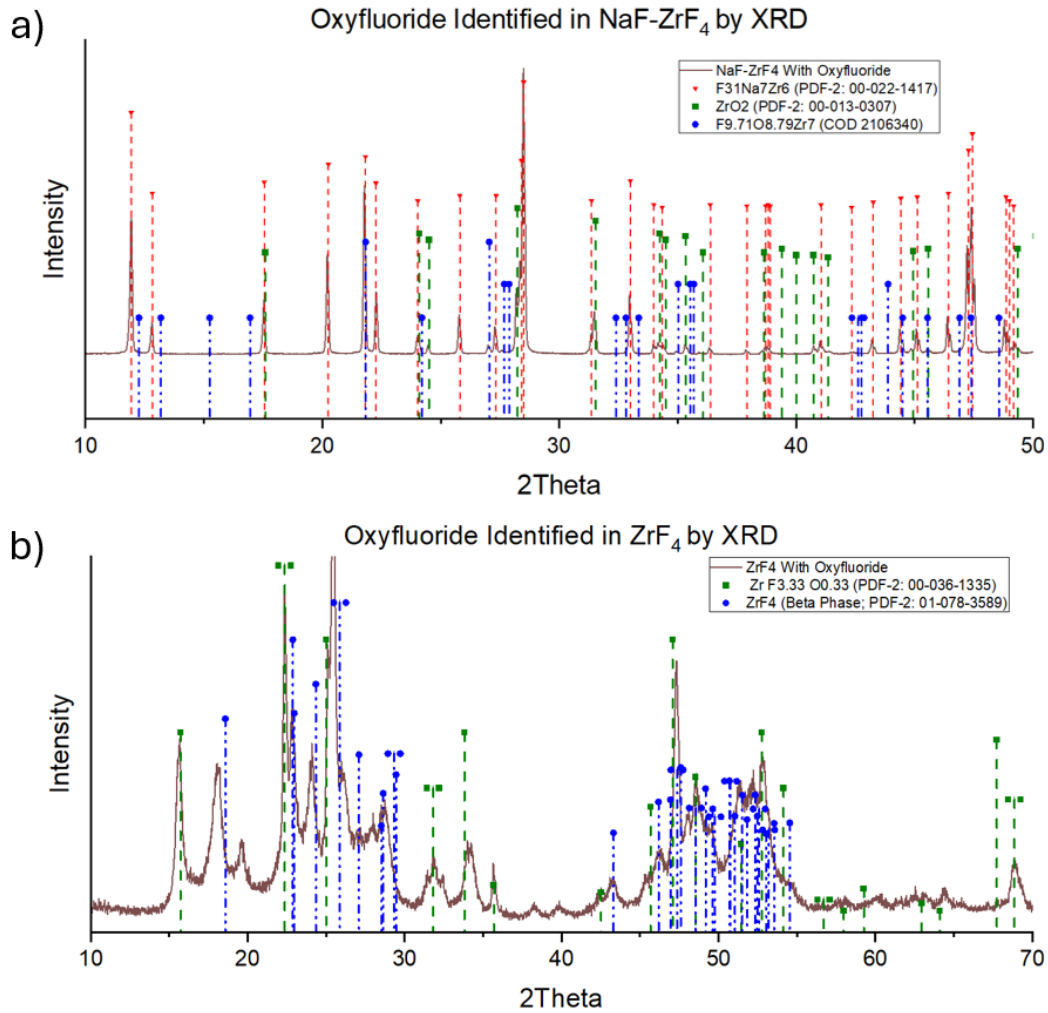


Figure 3.18: XRD Scan of a) Oxyfluoride identified in NaF-ZrF₄ sample including higher levels of ZrO₂ and b) low oxygen content oxyfluoride identified in baked ZrF₄ under inadequate conditions. Additional peaks not identified are potentially additional oxyfluoride phases.

3.4.4. Inductively Coupled Plasma Optical Emission Spectroscopy (ICP-OES) and Ion Selective Electrode (ISE)

To verify procedural consistency, several samples were analyzed with ICP-OES and ISE methods by Argonne National Laboratory. As a result, not every sample synthesized was able to be analyzed with this method. ICP-OES provides accurate cation contents, while ISE is used to provide reasonably accurate fluorine content. The averages

of these for each salt are provided in Tables 3.1 and 3.2 where results provided have a reported accuracy of within +/- 5% of the reported values.

Table 3.1: ICP-OES & Fluorine Results Compared to Ideal Composition of FLiNaK

Element	Ideal (LiF-NaF-KF 46.5-11.5-42 mol%)	Average ICP-OES (mol%)
Na	23.3	21.6
Li	21.0	20.7
K	5.8	5.8
F	50.0	52.4

Table 3.2: ICP-OES & Fluorine Results Compared to Ideal Composition of NaF-ZrF₄

Element	Ideal (NaF-ZrF₄ 53-47 mol%)	Average ICP-OES (mol%)
Na	15.5	17.1
Zr	13.8	15.5
F	70.7	67.4

To guarantee consistency with samples not tested with this method, the synthesis procedure was followed closely to minimize potential variation. In addition, samples of NaF-ZrF₄ were analyzed with SEM/EDS to compare compositional accuracy. A comparison of results from SEM/EDS on NaF-ZrF₄ is described in Section 3.4.5.

3.4.5. Scanning Electron Microscopy (SEM) with Energy Dispersive X-ray Spectroscopy (EDS)

Only salt samples of NaF-ZrF₄ were able to be analyzed by SEM/EDS. Sample pieces of NaF-ZrF₄ are mounted in epoxy and sequentially wet polished (using water) with sandpaper of increasing grit sizes of 180, 360, 600 and 0.5um alumina suspension.

Because low vacuum requirements and stable samples are necessary for proper SEM imaging, FLiNaK's hygroscopic behavior and solubility in water associated with polishing in air means meeting these requirements is not possible. Humidity still causes hydration of the FLiNaK, as described in Section 3.4.3, even if an oil-based suspension is used during the polishing step.

After samples of NaF-ZrF₄ are polished, imaging is performed using the Supra V55 with an EDS detector and later a Phenom PROX Desktop SEM, regions were analyzed for composition with EDS detectors at 15eV. In these samples, the bulk composition of the salt was examined for compositional consistency. These measurements were primarily compared to the ideal cation ratio and ICP-OES results described in Section 3.4.4. Example images of regions of impurity-free salt scanned with EDS are shown in Figure 3.19, with compositions determined by EDS provided in Table 3.3. As shown the Phenom PROX compositions are comparable to those of the Supra V55, although the Phenom tends to show slightly higher values for the observed cations (Na & Zr) then anions (F & O) than the Supra V55. Both present values within a similar margin of error to what might be expected by typical EDS analysis.

In addition, the zirconium oxide impurities are observed through SEM/EDS analysis. Analysis of as-made samples produced in Ni crucibles found ZrO₂ located at the nickel-salt and gas-salt interfaces. The bulk composition of salt between these impurities is additionally analyzed to check for any compositional variance. Examples of salt near the nickel-salt interface is shown in Figure 3.20. As typical with most samples, no additional impurities were identified in the region shown. Only a few occasions have

shown signs of Aluminum impurity. This was a byproduct of dust from the furnace’s insulation entering the salt (not shown).

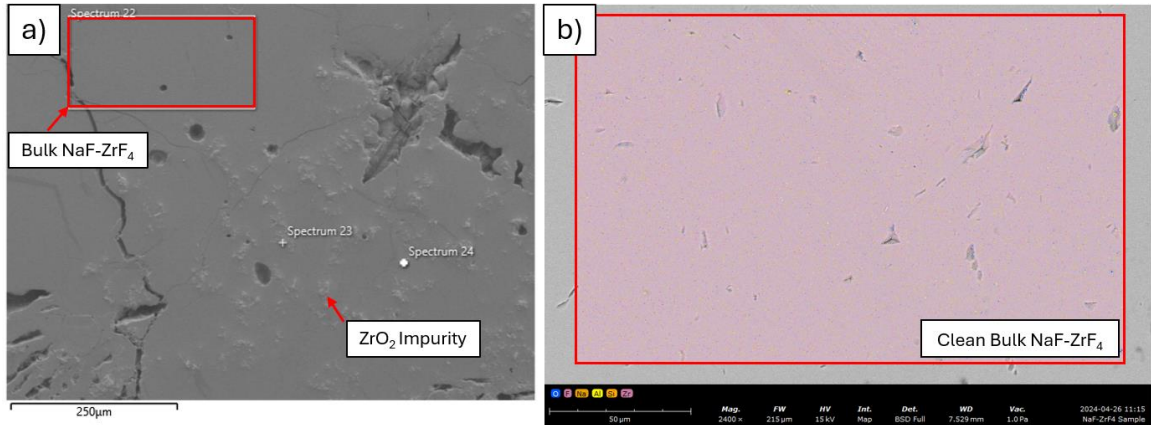


Figure 3.19: Comparison of SEM/EDS as performed on the SUPRA and Phenom RPOX Desktop SEM with EDS values reported in Table 3.

Table 3.3: Composition of Supra 55VP and Phenom of As Made salt samples

Element	Ideal %	Spectrum 22 (Atomic %)	Phenom Region (Atomic %)
F	70.7	69.2	65.63
Na	15.5	14.8	17.17
Zr	13.78	12.4	15.75
O	0	1.2	0.78

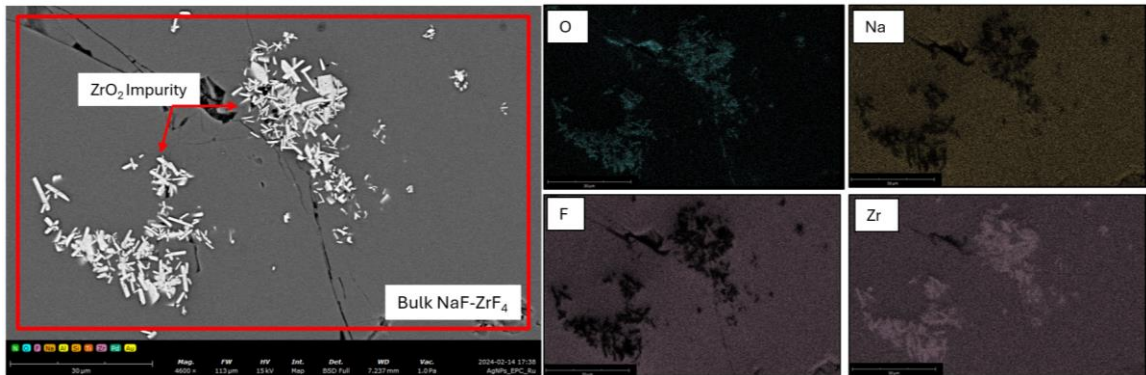


Figure 3.20: Mapping of as made NaF-ZrF₄ region near Ni-salt interface showing formation of ZrO₂ collecting in the salt.

Later sections describe additional results from SEM/EDS analysis performed on components and samples from each particular property measurement.

3.5. X-Ray Sample Handling Procedure and Relevant Lessons Learned

To produce the same conditions within the glove-box samples in the x-ray chamber, additional steps were required after preparing the sample holders and loading them into the x-ray chamber as described in Section 3.2.2. These steps were based on the necessary requirements for clean salt synthesis.

The purging and heating procedure in X-ray Sample Holder is as follows.

- a. An 80 to 110 mTorr vacuum was drawn on the x-ray chamber. Once the vacuum was reached, UHP Argon gas that was cleaned using a Drierite Column and oxygen trap heated to 300 °C was allowed to flow at roughly 10mL/min for one hour. This was done to establish a dry, oxygen-free environment within the chamber like that in the glove box.
- b. The vacuum was turned off and the chamber is backfilled with Argon gas to obtain a positive pressure 2 PSIG while still allowing a continuous Ar gas flow of 10ml/min. The sample was then heated to 300 °C at 2 to 5 °C/min and held for 2 hours. During this time, any moisture or oxygen absorbed by the salt was released and removed from the system, mimicking the baking step of the salt synthesis.
- c. The chamber was closed, and gas flow stopped, leaving the chamber isolated. This prevents any additional contaminants from entering the chamber that may affect the small sample size required for the x-ray measurements. In addition, this allows equilibrium vapor pressures of salt species to be established within the

chamber. This deviates from the conditions within the glove box but is deemed necessary due to small sample sizes required for the x-ray experiments.

Development of this procedure presented clear examples of the effects of inadequate environmental conditions on salt samples, some of which were already identified in previous sections.

Using as-made samples such as the SEM image in Figure 3.21.a. as a control, Figure 3.21.b. shows a SEM/EDS image of a NaF-ZrF₄ sample tested in the glove box chamber without adequate gas-purification steps. The salt shows signs of a significant reaction, where porosity indicates gas bubbles were present due to rapid production of HF. In addition, large amounts of ZrO₂ or Oxyfluoride formation have occurred.

Figure 3.21.c. depicts the SEM/EDS results of the second condition determined through x-ray chamber testing, a need for maximum operating temperature and limitation of vacuum use. Tests in the glove box chamber were initially performed at temperatures up to 800 °C on both salts. In addition, vacuum levels were initially kept as low as possible until the salt was at the desired set temperature. Between these two conditions, volatility of certain salt species, mostly identified as ZrF₄, were lost without any sign of a reactive byproduct such as ZrO₂. A literature search found evidence of excessive mass loss due to volatility to be the most likely culprit at temperatures above 700 °C at atmospheric pressure. [45] [58] Obviously, vacuum conditions would accelerate this loss. The results of testing NaF-ZrF₄ strongly agree with these conclusions, showing very low Zr levels by EDS analysis. This is the same behavior identified in FLiNaK, as shown by TGA in Figure 3.12, but the extent of which is difficult to determine due to the

uncertainty in the results.

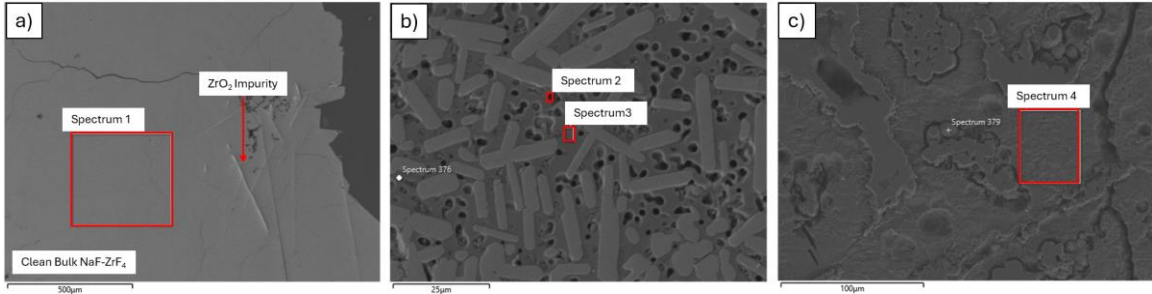


Figure 3.21: Associated samples from x-ray chamber procedural testing. A) The as made sample as produced in the glove box environment. This image shows higher levels of ZrO_2 as produced at an interface of the salt sample, also more common in earlier samples. B) A sample tested without the Drierite column and oxygen trap. C) A sample tested at 800 °C for 2 hours resulting in low Zr content. These samples are often difficult to polish, resulting in uneven surfaces.

Table 3.4: Sample composition by EDS analysis of x-ray chamber testing on NaF-ZrF₄

Element	Ideal Mole %	a) Spectrum 1 Mole %	b) Spectrum 2 Mole % (Oxyfluoride Phase)	b) Spectrum 3 Mole % (ZrO_2 Phase)	c) Spectrum 4 Mole % (Low Zr Phase)
F	70.7	70.9	19	1.6	67.7
Na	15.5	15.2	15.8	1.1	18.3
Zr	13.78	12.8	7.9	32.3	11.1
O	0	1.2	57.2	65.1	2.9

The last condition was to determine the necessary levels of oxygen content ($\ll 1$ ppm), more specifically the need to use an oxygen trap even with Ultra-High Purity Argon (< 5 ppm gas impurities of Oxygen and Moisture). FLiNaK samples tested in dry conditions without the use of the oxygen trap led to mass loss and a change in color from white to pink or red (Figure 3.7). It was not until the oxygen trap was introduced that the mass loss was negligible, and the color remained white after heating. In addition, samples of NaF-ZrF₄ often showed signs of mass gain under these conditions, identified by the

formation of oxyfluoride, but no formation of ZrO_2 . After the introduction of the oxygen trap, mass gain was no longer observed. Table 3.5 shows a set of tested variables and the outcome.

Table 3.5: Selected tests (incomplete) of various conditions on both salts showing possible indication of effect of different environmental conditions

Test Number	1	2	3	5	6	7
Salt	NaF-ZrF ₄	NaF-ZrF ₄	NaF-ZrF ₄	FLiNaK	FLiNaK	FLiNaK
Result						
Weight Loss (%)	-25.9	33.87	1.02	25.0	Not Recorded	0
Salt Color	-	-	-	Red	Slightly Pink	White
Variable						
Crucible Type	Graphite	Graphite	Glassy Carbon	Glassy Carbon	Glassy Carbon	Glassy Carbon
Drierite Column	Y	N	Y	N	Y	Y
Oxygen Trap	N	N	Y	N	N	Y
Gas State	Flowing	No Flow	No Flow	Flowing	Flowing	No Flow

3.6. Material Processing, Synthesis & Characterization Summary

Using the techniques available, several major impurities can be identified. While exact values of these impurities were not determined, characterization of the materials provides an indication that the salts remain reasonably pure, and close to the ideal composition. More importantly, the procedures used offer consistency in the samples synthesized and minimizes these impurities within the limits of the equipment available. These same procedures and analysis techniques are additionally used for samples in viscosity, density, and surface tension measurements, the results of which are described in later sections.

4. SURFACE TENSION & DENSITY DEVICE AND MEASUREMENTS

4.1. Introduction

Density measurements as a function of temperature for molten salts are quite common, and established procedures have produced repeatable results across multiple studies. By far the most common density measurement method for use with molten salts is the Archimedes method due to its simplicity and repeatability. [29] Additional surface tension corrections can be used to identify the property's contribution to density measurements. [27] Reported density measurements of FLiNaK predominantly use this method providing a reasonable range of values, some including a surface tension correction. [27, 59, 60, 28] Additionally, the limited reports on density of NaF-ZrF₄ predominantly use this method, however surface tension corrections are not mentioned in these reports. [59, 14, 61]

A less common method for measuring density is the maximum bubble pressure method. This method is typically known for measuring dynamic surface tension at the gas-liquid interface of a hemisphere at the end of a capillary (the bubble) at the point where the radius of curvature of the bubble at the edge of the tube is minimum. By taking these measurements at multiple depths, the density can be evaluated by determining the change in maximum pressure between two or more depths while generating bubbles. This relationship can be seen from evaluation of the Young-Laplace Equation (4.1). This evaluation identifies the maximum pressure obtained during bubble formation (P_{max}) as a function of depth (h) as having two components, pressure due to surface tension (P_{st}) and head pressure (P_{hydro}). Surface tension (γ) is then determined based on the capillary

diameter (r_{in}) while density is associated with the change in pressure with respect to height of the fluid under the effect of gravity (g). [30, 62, 39]

$$(4.1) P_{max}(h) = P_{st} + P_{hydro}(h) = \frac{2\gamma}{r_{in}} + \rho gh$$

Surface tension measurements as a function of temperature using the maximum bubble pressure method were reported by Janz in 1988. [11, 63] These measurements are predominantly used for surface tension corrections in density measurements of FLiNaK using the Archimedes Method. [28, 25] One additional study was identified confirming these surface tension results. [60] In another, it is not clear if the results are measured as part of the published work or used in reference for this work. [64] Only one study by Rose et al. at Argonne National Lab was identified as having reported an alternative evaluation of surface tension associated with error analysis on measurements of density with the Archimedes method. [27]

Only one reported value for surface tension using the maximum bubble pressure method was identified for NaF-ZrF₄ (53-47 mol%) in conjunction with density measurements using the Archimedes Method. This study also happens to be the one that confirmed the results of FLiNaK. While no surface tension corrections for density were mentioned. [60]

This connection between using surface tension and density poses a possible source of error if not properly considered. One measurement must be made prior to determining or correcting the second if two separate measurement methods are used. In addition, it is important to note the surface tension presents in the Archimedes method measurements as static, not dynamic (or near static) as obtained by the maximum bubble

pressure method. It is generally accepted that very low gas flow rates (1 bubble every 30 seconds) would approximate static surface tension. [39] This distinction between static and dynamic surface tension has not been addressed in reported density measurements for either salt aside from Rose et al. [27] Additionally, surface tension values reported by Janz do not include comments on this distinction, in part because the report is just a compilation of reported data. [63] The original study could not be identified and is generally not referenced in other work. In addition, no reported values of density using the maximum bubble pressure method were identified for either FLiNaK or NaF-ZrF₄.

Additionally, performing both measurements with the same technique is also a reduction in overall time since only one experiment is required. Because accurate measurements of both properties are dependent on each other, performing only one experiment would be optimal.

With these points in mind, this work utilizes the maximum bubble pressure method on FLiNaK and NaF-ZrF₄ (53-47 mol%) to provide new density and surface tension measurements as a function of temperature. Both measurements are determined from the same data set to avoid the possible error associated with separate measurements for both properties across different methods. Comparisons are made to previously reported values to see if measuring the properties together provides any difference in measurement results.

4.2. Sample Preparation

Samples for use with the maximum bubble pressure method were synthesized as closely as possible to the standardized procedure of Argonne National Lab [27] with

additional considerations from other past reports [47] as described in Section 3. Samples for both NaF-ZrF₄ (53-47 mol%) and FLiNaK (46.5-11.5-42 mol%) were prepared in an Argon filled glove box with 1ppm or lower of O₂ and H₂O. Precursors were obtained as single component powders from Sigma Aldrich with the highest purity possible. Each precursor is baked on a hot plate at 280 °C for 2 hours in a Ni-200 crucible that was polished with high grit sandpaper and then cleaned thoroughly to remove oxides. After baking, the reagent salts are weighed and mixed. The mixture is added to a similarly polished and cleaned Ni-200 crucible and melted in a furnace in the glove box, first additionally baking the sample at 280 °C for 1 hour then raising the temperature to 100 °C above the respective melting point for 2 hours. Samples are crushed to powder using a nickel mortar and pestle to help guarantee uniformity for next steps.

The crushed salt mixture was then added to fill a Boron Nitride (BN99 or HCBN) crucible that was 150mm tall with 9mm ID and 14mm OD. Enough salt was added to fill the crucible up by 75mm high. The salt was then melted inside the glovebox at approximately 100 °C above the respective melting point and held for 2 hours before returning the BN crucible to room temperature.

4.3. Maximum Bubble Pressure Testing Setup

The experimental setup was designed similarly to several other studies utilizing the maximum bubble pressure method on various molten salts. [62, 64, 65] The diagram of the system used in this work is shown in Figure 4.1. The maximum bubble pressure method probe was a 304 or 316 stainless-steel tube long enough to reach well into the crucible (although not to the bottom) from the top flange connection, about 10 in. (254

mm). The tube had a nominal OD and ID of 0.125 in. (3.175mm) and 0.085 in. (2.159mm) respectively. The end of the tube was prepared by grinding the end with a belt grinder or cutting the end with a sectioning saw so the end of the tube is as perpendicular to its length as possible given the methods. The end of the tube was then lapped with sandpaper of increasing grit sizes until any burrs were removed. Lastly the inner edge of the tube was sanded slightly to remove any remaining burr.

Dimensions were chosen based on compatibility with the glove box furnace, designed for use for multiple property measurements. Additionally, a thermocouple was placed parallel to the bubbling tube to determine the temperature of the salt. The tube is run through a lid piece and held in place with an additional support connected to the flange. This lid was to help mitigate temperature and mass loss due to volatility at higher temperatures but does not completely seal against mating components such as the crucible and bubbling tube to allow gas used to form bubbles to escape. The lid also acted as a guide piece for keeping the crucible straight, and the bubbling tube concentric to the crucible. Lastly a reference wire was inserted through a parallel alumina tube. The wire was left exposed past the end of the bubbling tube to act as an electrical reference for probing the liquid surface. The upper end of the wire and tube were connected to a multimeter. Further details of this assembly are shown in Figure 4.2 a through c. It is important to note that the end of the thermocouple is set approximately 1mm before the end of the tube. The reference wire is also bent in such a way that it stays further away from the end of the tube. This was to ensure that the thermocouple and reference wire would not interfere with bubble formation, as verified during room temperature testing

described in Section 4.6.1.

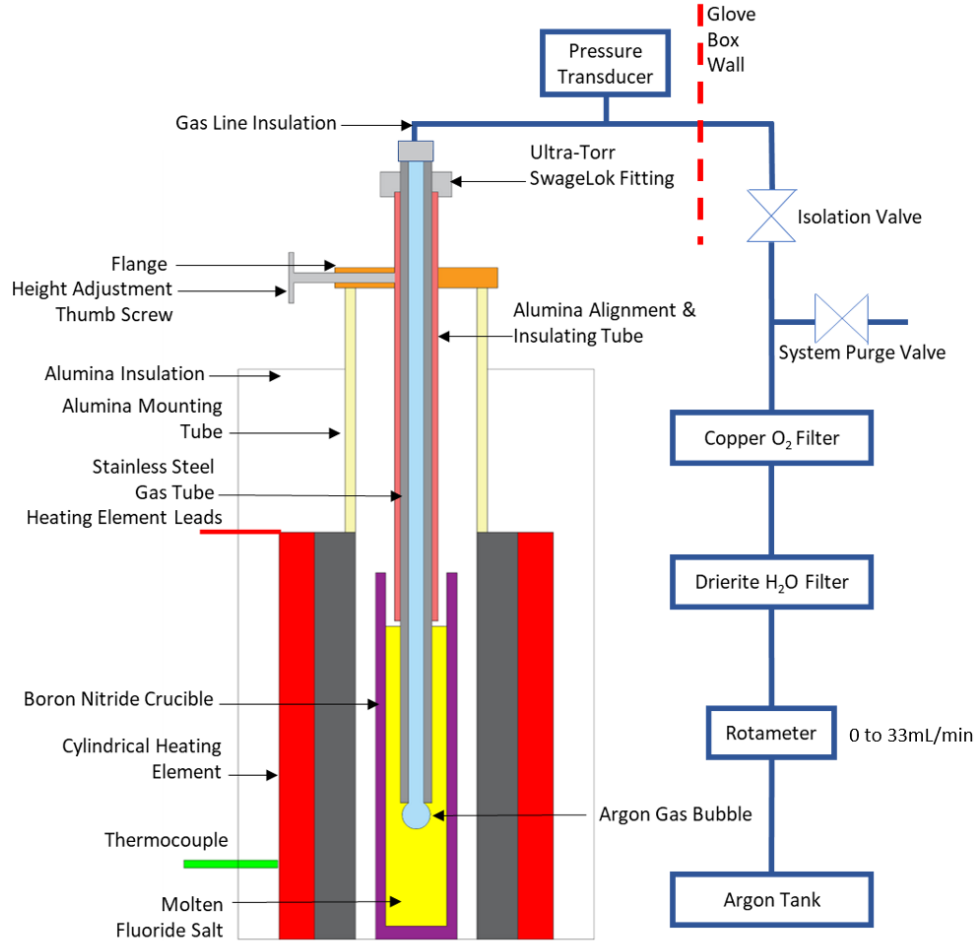


Figure 4.1: Diagram of bubbling tube and plumbing schematic used for surface tension.

This assembly was then inserted into the glove box furnace, as depicted in Figure 4.2.d. The top end of the bubbling tube was attached to a gas line that includes a digital pressure transducer (PX409-USBH-453852). Data was collected using Omega's Digital Transducer Application. The transducer has a reported accuracy of 0.08% best fit straight-line (BFL) accuracy, with no specific pressure variation of given points provided. Obtained baseline signals, as shown in Figure 4.3, show a variation of approximately +/- 4 Pa. A sampling rate of 40 samples per second was chosen within the program to

optimize sensitivity. The pressure transducer was installed inside the glove box, so the measured pressure differential of the transducer uses the glove box pressure as the baseline “atmospheric” pressure. This also allows for the transducer to adjust to any changes in pressure inside the glove box during data collection.

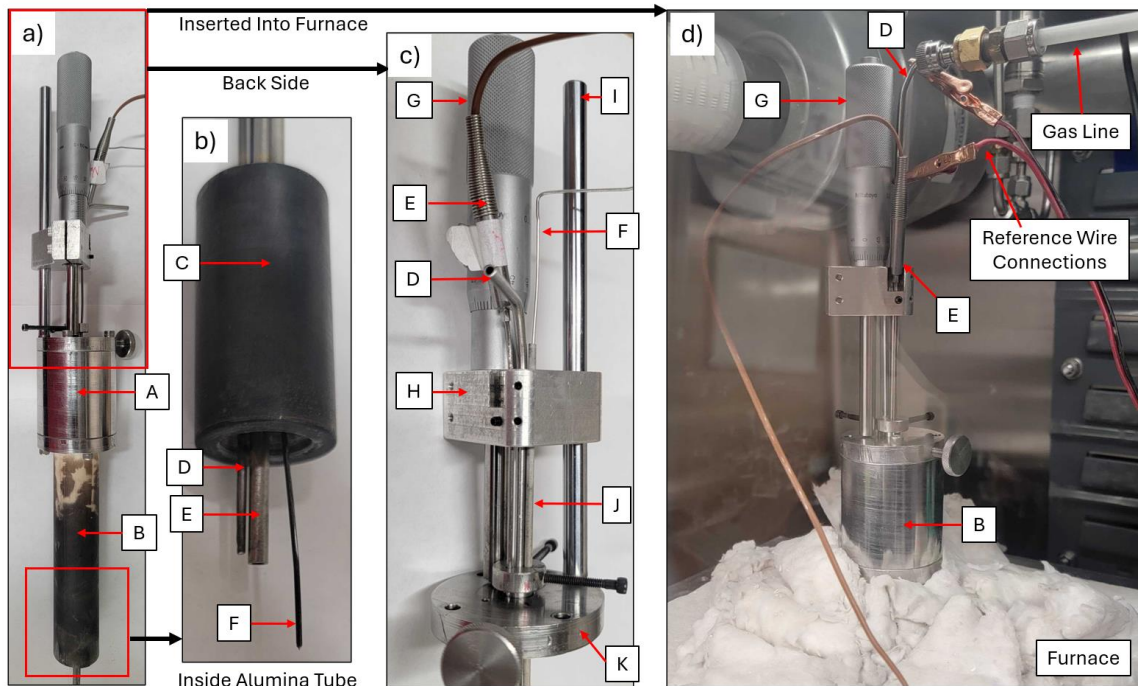


Figure 4.2: Pictures of the surface tension probe where a) shows the entire assembly prior to inserting it into the furnace. The flange (A) and alumina tube (B) for mounting the tube sub-assembly are clearly visible. The internal bottom portion of the assembly is shown in b) where the lid and guide (C) have the bubbling tube (D) thermocouple (E) and reference wire (F) with alumina sheathing interested through it. The top half of the assembly is clearly shown in c) showing the screw micrometer (G) as assembled with the movable guide block (H). The top portion of the bubbling tube (D) thermocouple (E) and reference wire (F) are also visible. The reference wire for the alumina sheath (J) is not attached to the moving block (H). A guide (I) is used to prevent the moving portion from twisting. The top of the flange (K) is used to mount to the flange body (A). The entire assembly is inserted into the furnace as shown in d) where the gas line and reference wire connections are attached.

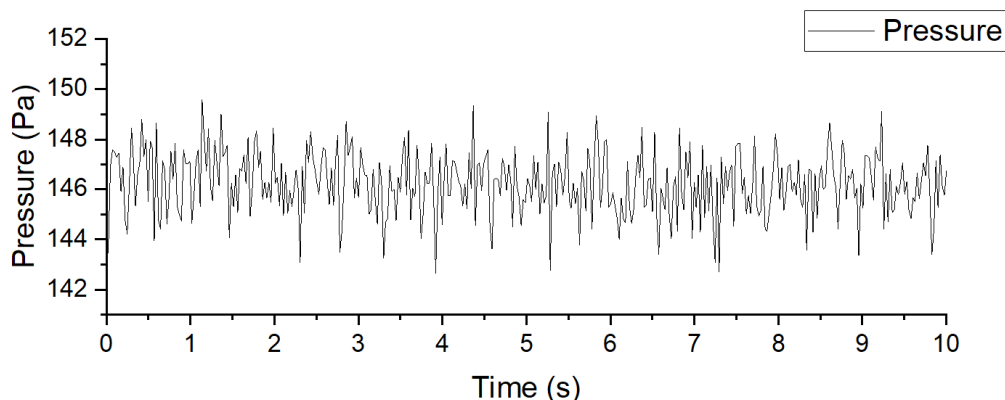


Figure 4.3: Baseline pressure reading of uncalibrated signal of PX409 pressure transducer while installed into glove box with flowing gas.

The gas line also includes a Drierite moisture trap, and a copper-copper oxide oxygen trap operated around 300C (+50, -10). Lastly a low flow rate rotameter was installed, with a 33 mL/min maximum (FLDAR3505G) to control the flow rate. A flow rate of 1 mL/min was held for most runs. A few measurements on NaF-ZrF₄ were done with a higher flow rate (6 mL/min) to test the effect on surface tension results. The pressure transducer was calibrated, setting the relative pressure to zero when gas is flowing, mitigating possible pressure from gas flow. Density and surface tension (γ) values are determined by observing the maximum pressure recorded by the pressure transducer as a function of immersion depth of the bubbling tube into the molten salt.

4.4. Maximum Bubble Pressure Experimental Procedure

Once the system is assembled, the gas line is purged with ultra-high purity (UHP) Argon. Then, with the gas turned off, the furnace is brought up to temperature. At any given set temperature, the temperature is allowed to stabilize for 30 minutes with no gas flowing into the furnace.

Next the liquid-salt surface position needs to be identified. First, the reference

wire was lowered into the salt. With the multimeter on, the bubbling tube was slowly lowered down towards the surface of the salt using the mounted screw micrometer. When it contacted the fluid, an increase in pressure was observed, indicating the end is touching the fluid. This position was verified by observing a connection via the multimeter simultaneously. The position on the micrometer was recorded as the reference for the zero-depth position ($h_{surface}$).

With the gas still flowing, the tube was then additionally lowered 3-5 mm into the salt to the first depth (h_{depth}) where the temperature was stable. With the position of the fluid surface, uncorrected depth ($h_{uncorrected}$), or the depth that does not account for displaced salt, was determined based on the set depth position on the screw micrometer and previously recorded surface position (4.2).

$$(4.2) \quad h_{uncorrected} = h_{depth} - h_{surface}$$

From here measurements were started, verifying that bubble formation was consistent by watching the change in pressure on a continuously updating plot within in the transducer application. This was repeated for a minimum of 5 depths, in 1 to 2 mm increments.

The pressure with respect to time was recorded for a minimum of 30 seconds or a minimum of 5-10 bubbles at each depth to be used for analysis later. Most data sets were collected for longer intervals. An example of good data for a particular set temperature is shown in Figure 4.4. As shown, the data shows a clear increase in pressure as a function of depth. Some variability in peak height was additionally observed. In addition to pressure, temperature is recorded at each depth to verify temperature consistency. This

procedure was performed at multiple temperatures on a single sample.

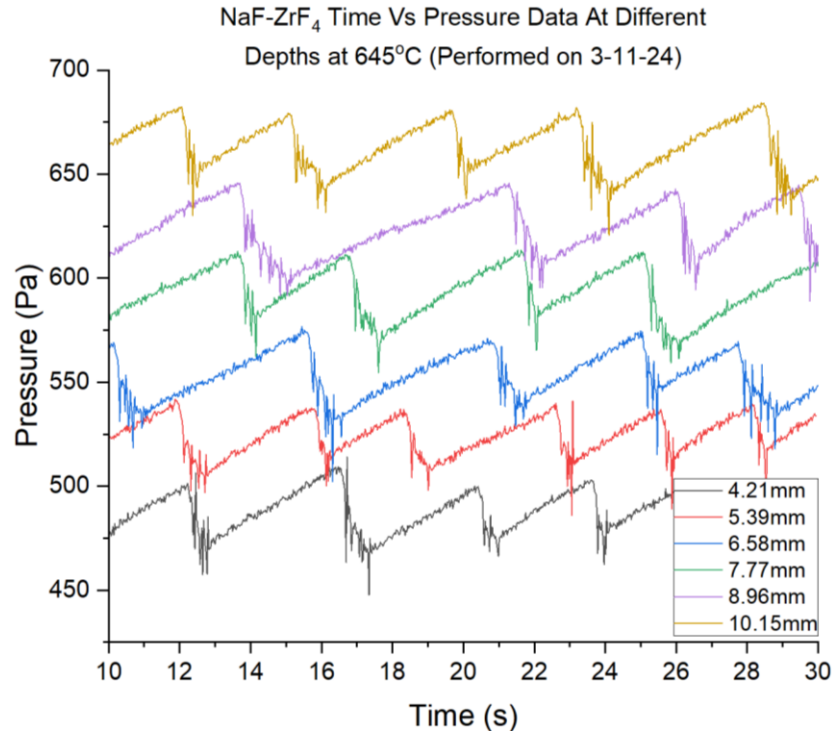


Figure 4.4: Pressure data as a function of depth as collected at 645 °C on the NaF-ZrF₄ showing distinct pressure changes at each depth.

4.5. Maximum Bubble Pressure Data Analysis

To determine properties from the collected data, the maximum pressure during bubble formation needed to be identified, as described by Equation 4.1. To extract these maximum values the “find peaks” function in the Signal Processing Python library (`scipy.signal`) was utilized. [52] Parameters were adjusted as needed for the program to properly identify the maximum pressure peak locations. Inaccurate peak locations were then manually removed. These primarily include inconsistent spikes in pressure described in Section 4.6.1. (very high values with very little ramp in pressure). Others include signs of early bubble release, indicated by very low relative maximum pressure with very short bubble formation time, an example of which is shown in Figure 4.5. Peak values at a

particular set depth are then averaged and used for further analysis.

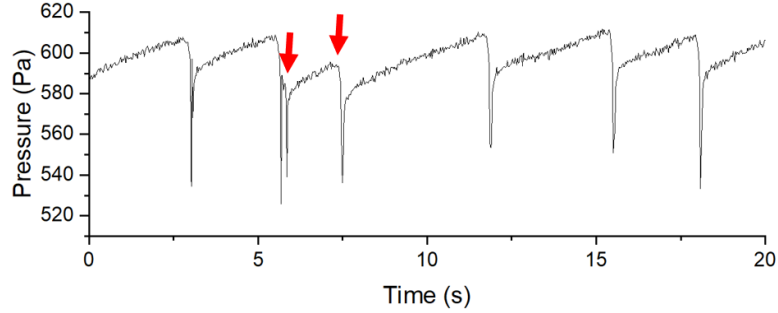


Figure 4.5: An example of data collected that includes early bubble release identified by short bubble formation times with outlying low peak pressure. These bubbles are indicated by the red arrows.

First density was determined by noting variation of bubble maximum pressure as a function of depth. This was identified by taking the derivative of maximum pressure (P_{max}) with respect to depth (h) of Equation 4.1. The derivative (4.3) indicates that the slope of a linear regression fit to the maximum pressure values correlates to density.

$$(4.3) \frac{dP_{max}}{dh} = \rho g$$

The correct slope was obtained by correcting the depth ($h_{corrected}$) to account for the increase in fluid height ($h_{increase}$) (4.4) based on the outer radius of the bubbling tube (r_{tube}), the radius of the thermocouple (r_{TC}) and the inner radius of the crucible (r_c) (4.5). All dimensions were corrected for thermal expansion (4.6) based on the respective material's thermal expansion coefficient (α) and measured temperature in the salt ($T_{measured}$). Nominal tube dimensions were used for evaluation.

$$(4.4) h_{corrected} = h_{uncorrected} + h_{tube,v} + h_{wire,v}$$

$$(4.5) h_{tube,v} = h_{uncorrected} \left(\frac{r_{tube}^2 + r_{TC}^2}{r_c^2 - r_{tube}^2 - r_{TC}^2} \right)$$

$$(4.6) r_{effective} = r + r\alpha(T_{measured} - 298[K])$$

Similarly, increased height due to the reference wire with radius r_w was also accounted for but instead was based only on the increased height due to the tube submersion since the wire remains static. (4.7)

$$(4.7) h_{wire,V} = h_{tube,V} \left(\frac{r_w^2}{r_C^2 - r_{tube}^2 - r_{TC}^2 - r_w^2} \right)$$

Note that the thermal expansion due to the tube length was predominantly accounted for by probing the surface of the salt. This could additionally be corrected for based on the temperature between the surface and submersion depth, but this correction was expected to provide minimal error.

With these considerations to obtain the density, the intercept of the same linear regression is already corrected accordingly assuming the identified surface position was accurately obtained. This provided P_{st} , where dynamic surface tension (γ) was determined based on the inner radius of the bubbling tube corrected for thermal expansion (r_{in}) (4.8).

$$(4.8) P_{st} = \frac{2\gamma}{r_{in}}$$

Example data analyzed with these methods is provided in Figure 3.6, which includes uncorrected and corrected linear correlations between depth and pressure. Using the linear regression for the corrected depth, the slope and intercept were used to evaluate density and surface tension based on Equations 4.2 and 4.8 respectively.

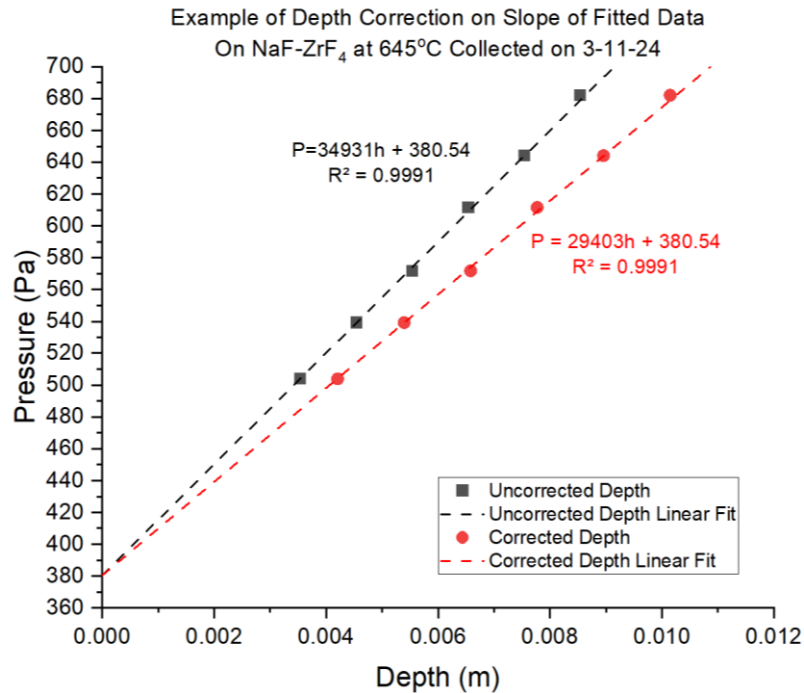


Figure 4.6: The average maximum peak plotted as a function of uncorrected (black) and corrected (red) depths at 645 °C. Note that the intercepts remain constant, as the density can be evaluated independently from surface tension.

4.6. Maximum Bubble Pressure Results

This section provides results from room temperature verification testing of the procedure and analysis as described in previous sections. These results show successful measurements at room temperature, as described in Section 4.6.1. Following, the results obtained on FLiNaK and NaF-ZrF₄ are presented along with specific characterization of the salts and components post measurement in Sections 4.6.2 and 4.6.3 respectively.

4.6.1. Room Temperature Testing and Verifications

Prior to performing high temperature experiments, verifications on system procedure and accuracy were performed at room temperature. Room temperature (20 °C ±1) water was used in a clear acrylic tube with the same diameter as the crucible for high temperature experiments (9 mm). Images of bubble formation at different stages are

shown in Figure 4.7, depicting proper bubble formation. The corresponding observed pressure change in association with each stage of bubble formation is additionally provided in Figure 4.7 with a labeled a time vs pressure plot of an example bubble. The room temperature experiments showed consistent values in density and surface tension, with averaged data and standard deviation shown in Table 4.1.

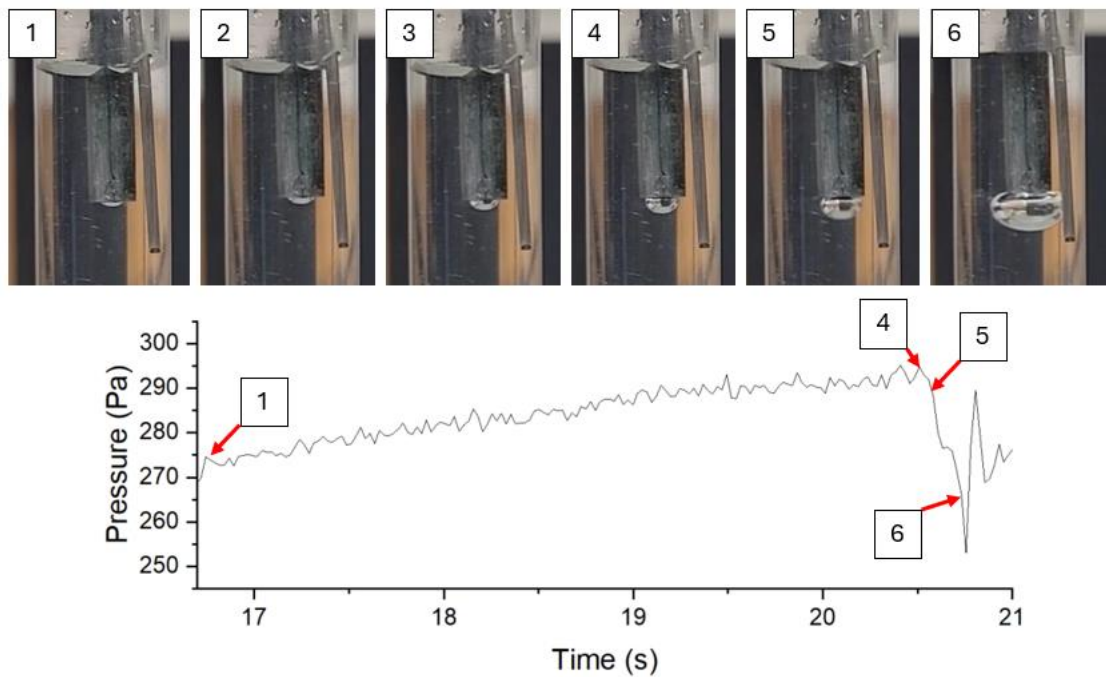


Figure 4.7: Stages of bubble formation as observed with collected data in this study. The bubble starts forming initially (1) with slow pressurization slowly increasing bubble size (2,3) and reaching a maximum pressure as a hemisphere (4). Bubbles are then detached from the inner radius of the tube (5) and rapidly expand while the pressure decreases (6) before releasing from the tube.

Table 4.1: Room Temperature Water Surface Tension and Density Verification Measurements

	Ideal at 68 (°C)	Measured (Average)	Standard Deviation	Percent Error from Ideal
Density (kg/m ³)	998	1004.55	8.16	0.66
Surface Tension (mN/m)	72.74	70.91	1.48	2.52

Furthermore, these experiments were used to test additional parameters, primarily the tube's inner diameter. During this testing, the presence of a secondary spike after bubble release was observed. Larger spikes were observed using a smaller ID tube size (0.055 in). While seen with both diameters, the effect is more prominent with the smaller ID tube, as shown in Figure 4.8. As described by the capillary rise (h_{cap}) Equation (4.9), a decrease in effective inner diameter (or inner radius, r_{in}) is expected to cause an increase in capillary rise. This effect is additionally dependent on contact angle (θ), fluid density (ρ_f) and gravitational acceleration (g). This pressure spike was therefore associated with capillary forces that would be expected to have more influence with a decrease in inner diameter.

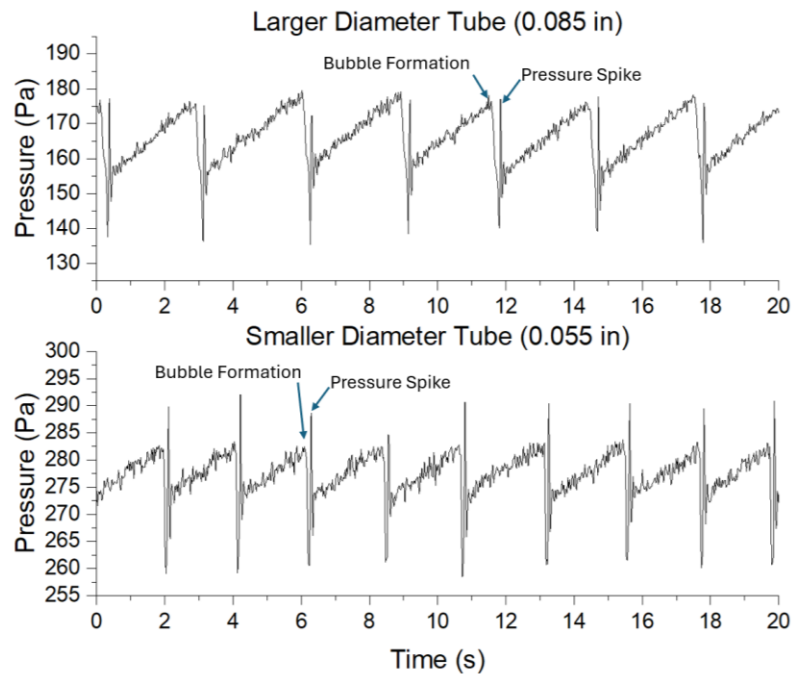


Figure 4.8: Comparison of spike anomalies during bubble formation between different size diameter tubes.

$$(4.9) h_{cap} = \frac{2\gamma\cos\theta}{r_{in}\rho_f g}$$

As a result, it was determined that the larger diameter tube is necessary due to the higher surface tension of the molten salts. In part this is offset by the increase in density, however the presence of these spikes was occasionally still observed during measurements of the molten salts. This does not seem to effect measurement results if pressure spikes are carefully excluded as part of the analysis process.

4.6.2. Molten Salt Measurement Results

Results for density and surface tension across several measurement runs were averaged together and compared with literature studies of the same salts. Average density measurements for FLiNaK as a function of temperature are shown in Figure 4.9 with comparisons to selected studies. Additionally, the trend coefficients are provided in Table 4.2 based on Equation 4.8.

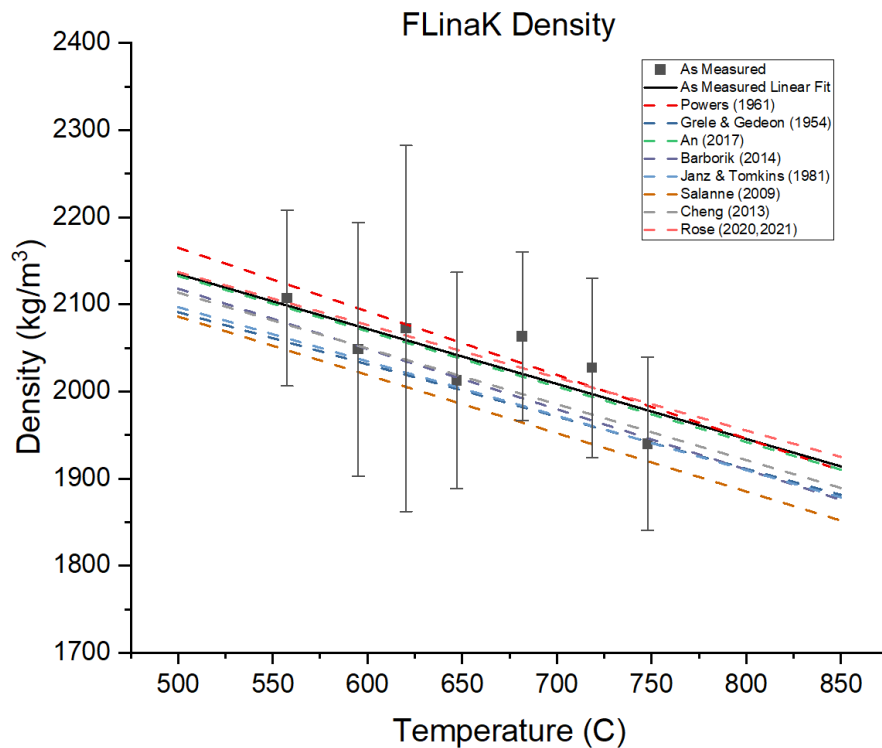


Figure 4.9: As measured FLiNaK density compared to select studies from literature.

$$(4.8) \rho = A - BT[C]$$

Table 4.2: FLiNaK Density kg/m³ Coefficients

Source	Surface Tension Correction	A	B
Grele & Gedeon (1954) [11] [K]	Not Mentioned	2555	0.060
Powers (1961) [59, 25] [C]	Not mentioned	2530	0.73
Salanne 2009 [59, 25] [K]	Not mentioned	2603	0.669
Cohen & Jones (1954) [59, 25] [K]	Not mentioned	2655.64	0.68
Vriesema (1979) & Williams (2006) [59] [K]	Not mentioned	2729.29	0.73
Janz & Tomkins (1988) [11] Samuel (2009) Chrenkova (2003) Cibulkova (2006) [25] [K]	Not mentioned	2579	0.624
Cheng (2013) [25] [C]	Corrected	2434	0.641
An (2017) [25] [C]	Corrected	2450	0.634
Barborik (2014) [60, 25] [C]	Measured, unclear if it was corrected	2464	0.692
Rose (2021) [27, 25] [C]	Corrected	2440	0.587
This Work [C]	Corrected	2450	0.6313

The average surface tension measurements as a function of temperature for FLiNaK are plotted in Figure 4.10. The representative trends are shown in Table 4.3 based on Equation 4.9. Comparable studies on surface tension measurements of FLiNaK are limited in comparison to density, with one report possibly having not actually measured the property themselves just referencing former work (values are not plotted but are included in Table 4.3). [64]

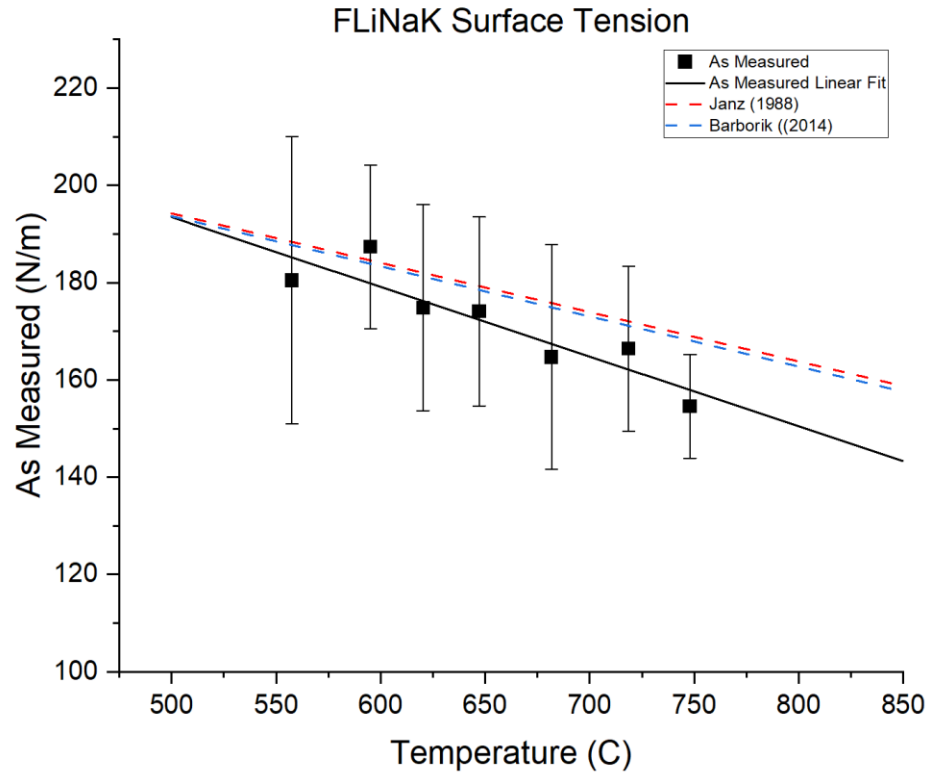


Figure 4.10: As measured FLiNaK surface tension compared to available published studies.

$$(4.9) \gamma = C - DT[C]$$

Table 4.3: FLiNaK Surface Tension (mN/m) Coefficients

Source	C	D
Janz (1988) [63] [K]	272.6	0.1014
Kubikova (2009) [64]*[K]	272.6	0.1014
Barborik (2014) [60] [K]	273.265	0.103
This Work [C]	213.5	0.1029

*Not clear if this is measured or referenced

Similarly, average density measurements for NaF-ZrF₄ are plotted in Figure 4.11 and average surface tension measurements plotted in Figure 4.12. Coefficients for the fitted values along with reported coefficients from previously performed studies and for NaF-ZrF₄ are provided in Table 4.4 and surface tension measurements with the only identified reported study is included in Table 4.5. Values used for density include

measurements from flow rates at 1mL/min and 6mL/min. Inclusion of these measurements is considered acceptable since flow rate has no effect on the head pressure, the component of pressure associated with density as described in Section 4.4. Density measurements of NaF-ZrF₄ appear to be closer to compositions of lower Zr content (Cohen 57-43 mol%).

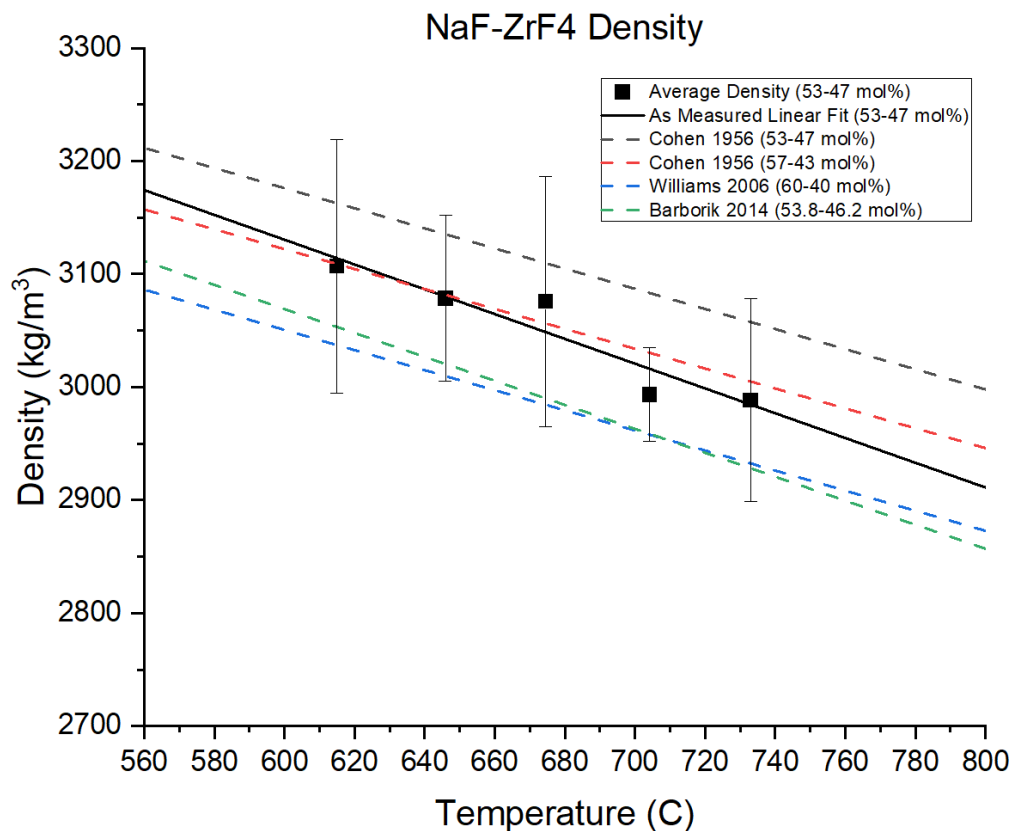


Figure 4.11: As measured NaF-ZrF₄ Density compared to selected studies from literature of varying compositions.

Average measurements for surface tension are separated by flow rate. Surface tension measurements with 6mL/min flow rates show a different trend with respect to temperature than measurements utilizing 1mL/min. These higher flow rate values cannot be accurately compared to reported literature as they utilize either near static methods or

low flow rates to obtain property values. Exact flow rates were not mentioned in those reports.

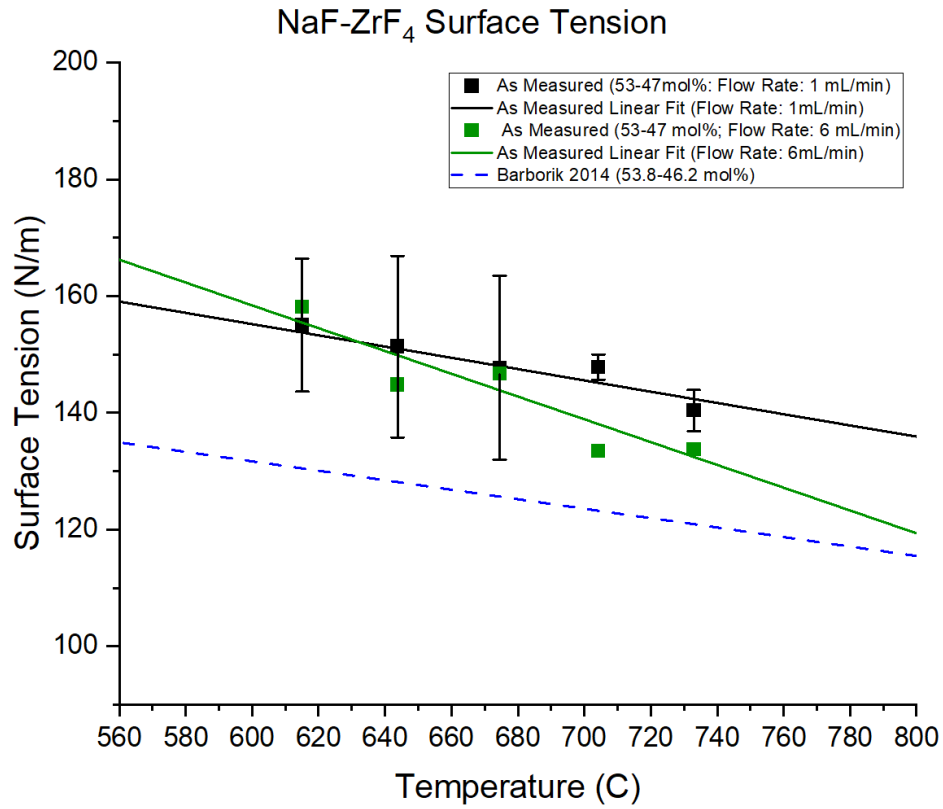


Figure 4.12: As measured NaF-ZrF₄ surface tension compared to available published studies.

Table 4.4: NaF-ZrF₄ Density kg/m³ Coefficients

Source	A	B
Cohen 1956 (53-47 mol%) [59]	3710	0.89
Cohen 1956 (57-43 mol%) [59]	3650	0.88
Williams 2006 (60-40 mol%) [59]	3584	0.89
Selanne 2009 (57-43) [59]	3935	0.918
Barborik Na ₇ Zr ₆ F ₃₁ (2014) [60]	3995	1.06
This Work	3788.1	1.096

Table 4.5: NaF-ZrF₄ Surface Tension (mN/m) Coefficients

Source	C	D
Barborik Na ₇ Zr ₆ F ₃₁ (2014) [60]	202.39	0.081
This Work (1mL/min)	222.8	0.1102

4.6.3. Post Measurement Characterization

Characterization was performed after each set of measurements on both salts and the ends of the bubbling tubes. Salts are weighed before and after for any mass loss. Minor mass loss can be expected due to salt wetting to the tube and splatter from the bubble popping.

First, crushed samples of as made and post measurement salts are analyzed by XRD analysis utilizing the Bruker D2 Phaser. Bragg peaks are matched to known materials in the Crystallography Open Database 2018 (COD) and PDF-2 Release 2020 RDB (PDF-2) database. FLiNaK is compared to its precursor components, LiF (PDF-2: 00-004-0867), KF (PDF-2: 00-036-1458), and NaF (PDF-2: 00-036-1455). NaF-ZrF₄ (53-47 mol%) is compared to the salt of closest composition available (Na₇Zr₆F₃₁ PDF-2: 00-022-1417). Examples of scans for each salt are shown in Figures 4.13 and 4.14 respectively. For NaF-ZrF₄, samples are taken from different regions in the salt: the top, middle, and bottom. ZrO₂ (PDF-2: 00-013-0307) created during the synthesis of the salt settles at the bottom and is additionally observed in the XRD scans. For successful runs, no additional impurities were identified. Any runs with additional impurities as described in Section 3 were excluded.

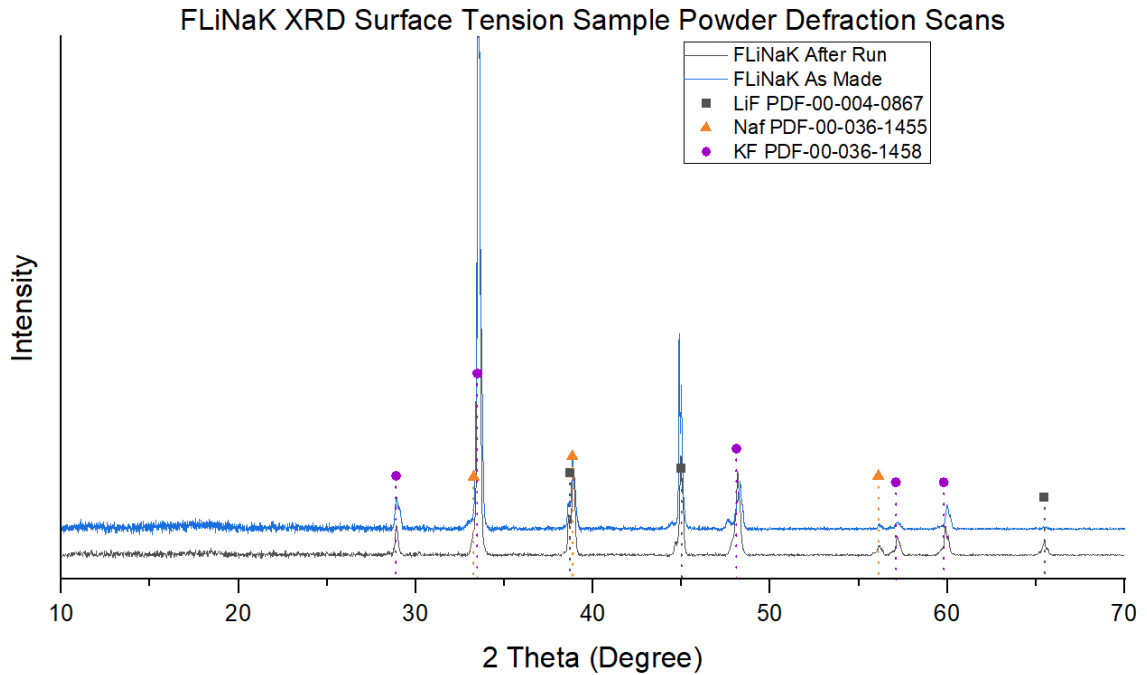


Figure 4.13: XRD scans of as measured FLiNaK. For this salt, samples are only taken from near the top of the crucible. Samples are compared to salt precursors the as made salt scan.

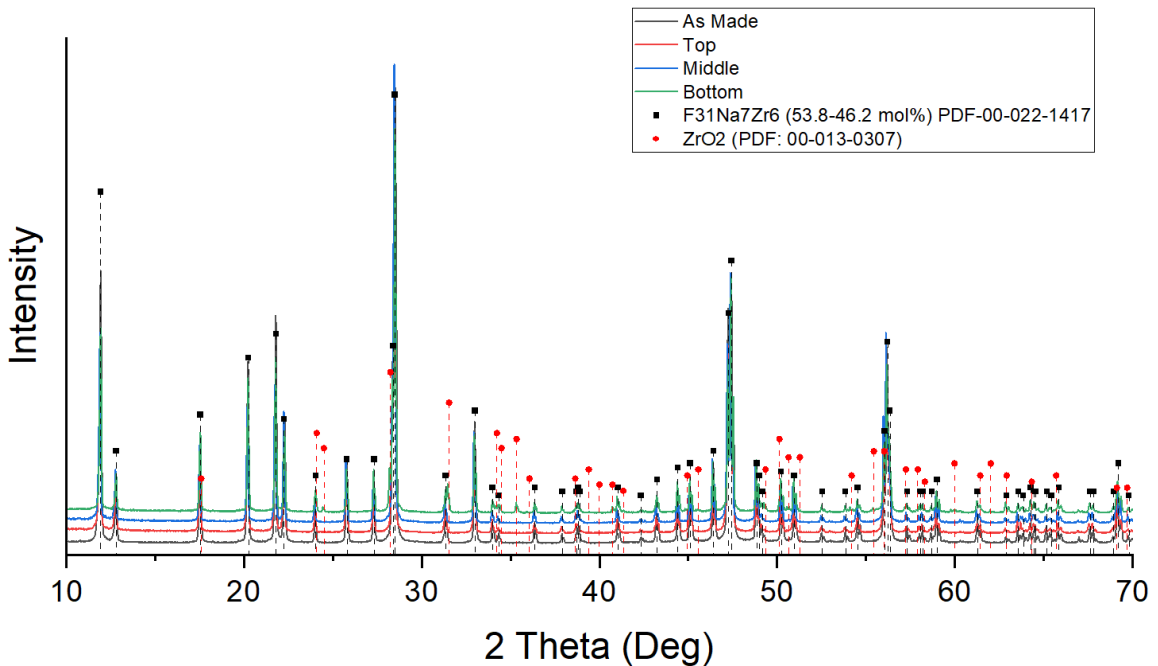


Figure 4.14: XRD Scans of as measured NaF-ZrF₄ samples taken at different depths, near the top, middle, and bottom of the sample to look for indications of high oxyfluoride content. Scans are compared to Na₇Zr₆F₃₁ and the as made salt scan.

Additionally, after each set of measurements, the ends of the bubbling tubes were checked for excessive corrosion by SEM/EDS. Qualitative analysis was used since precise cross sections along the length of the tube were not possible due to the hand polishing procedure performed as described in Section 3. Due to this, dimensions taken based on the SEM images are not comparable to nominal values and tolerances of the tube. Additionally due to the small ID of the tubes and wetting of salt to the surfaces, calipers or micrometers would not provide accurate measurements of the ID or wall thickness.

Tubes are compared to images of a Stainless Steel 304 tube segment to act as a control, as provided in Figure 4.15.a and 4.15.b, for qualitative analysis. The end of the tube was prepped with the same procedures as ones used for measurements. Images show a relatively consistent surface on the outer wall of the tube seen by a straight edge in the SEM images. In comparison, the inner surface shows higher surface roughness and non-uniformity as manufactured on an additional segment of the tube, shown in Figure 4.15.c. The wall thickness of the open end of the control tube has a 4 μm variation at the last 400 μm of the tube. Other segments show as much as 14 μm variation.

In comparison, tubes exposed to FLiNaK and NaF-ZrF₄, such as examples provided in Figure 4.16, show pitting on the outer surfaces that have the most contact with the salts. This includes the end surface of the tubes. Some additional corrosion is also observed at the inner corners of the tube ID, as shown in Figures 4.16.a and 4.16.b. Corrosion in these regions is likely higher since there is a gas-liquid-solid interface, or a region where oxygen and moisture may react with both the molten salt and the tube.

Some tubes, such as the FLiNaK example in Figure 4.16.c, show deformation of the tube possibly caused during tube end preparation. This is not expected to cause issues with bubble formation as it remains consistent around the diameter of the tube.

Additionally, some minor cracking was sometimes observed on the inner walls that was not present in the control, best shown in Figure 4.16.d. Looking further along the inner walls of the tubes (away from the tube end), no obvious signs of pitting are identified. These surfaces, as shown in Figures 4.16.e through 4.16.f, appear to have the same inconsistency as observed in the control tube.

When comparing variation in wall thickness and outer wall conditions near the ends of the tube, minor differences can be identified. In the same regions on tubes exposed to both salts, slightly higher variability in wall thickness was observed. Examples in Figure 4.16 show indication of some minor losses of around 5-6 μm when comparing wall thicknesses between the used and unused tubes (about 0.98% to 1.18% of the nominal wall thickness of 508 μm). It must be noted that this does not accurately represent the possible loss as some regions of the as-made tubes show much higher variation in wall thickness (Figure 4.15). It can however be an indicator of possible changes to the ID at the very end of the tube that might affect evaluation of surface tension. In this case, as in most cases, this change was minimal, suggesting an increase in ID of approximately 0.45% to 0.55%. Based on that analysis, it can be concluded that changes to the ID of the tube due to corrosion are minimal and do not significantly impact results.

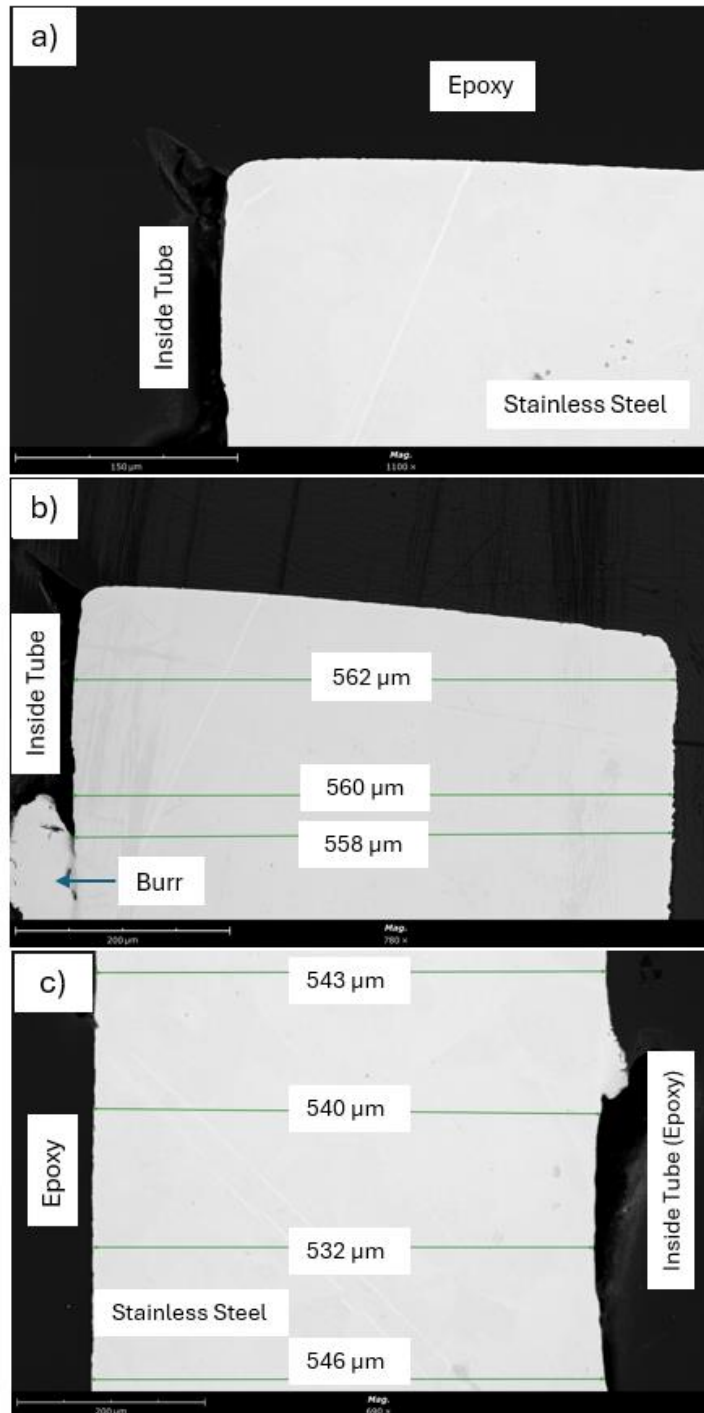


Figure 4.15: Example SEM images of tube cross sections a) A cross section of a prepared tube ends inner corner. b) A cross section of a tube end after exposure to FLiNaK. Note the heavy radius is as prepped, not from corrosion. c) A cross section of a tube with sharper corner between the inner edge and bottom surface end after exposure to NaF-ZrF₄. Note, the heavy corrosion on the sharp corners of the tube.

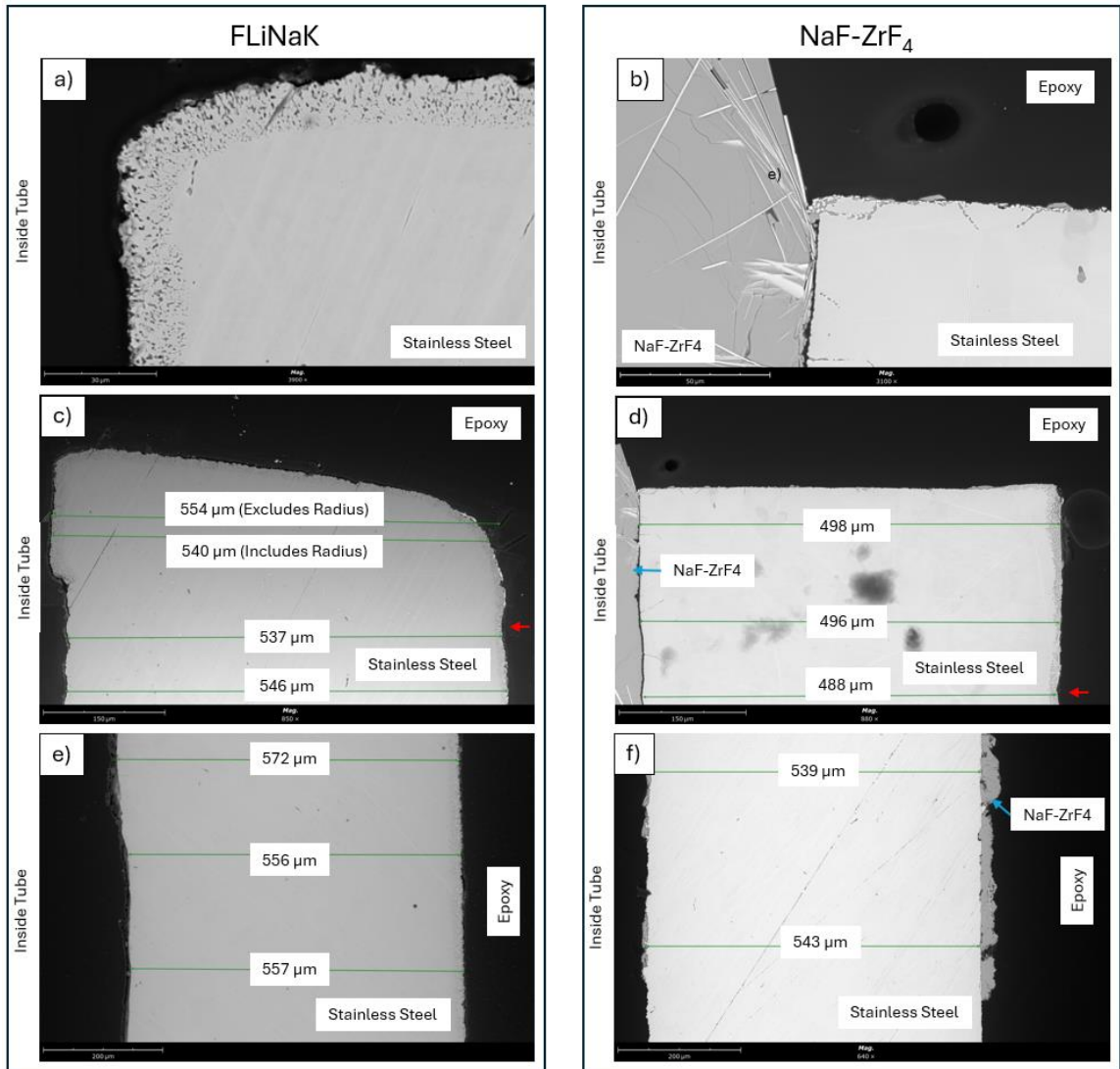


Figure 4.16: Comparison of segments of (a) a Control Tube Stainless Steel 304 tube and (b) a Stainless Steel 304 tube exposed to FLiNaK. Tube segments are away from the tube end but show similar variation in each (maximum difference of 11 μm and 15 μm respectively). Note the outside surfaces remain straight for both tubes.

Along with SEM images, EDS line scans were additionally performed on the corroded regions of the tube going from uncorroded steel to the encapsulating epoxy housing the stainless-steel tubes during SEM imaging. These corroded regions show a decrease in chromium content compared to the outer surface of the tube. Example results for the control tube and those used with FLiNaK and NaF-ZrF₄ are provided in Figure

4.17, 4.18 and 4.19 respectively. Original EDS scans collected were analyzed for all expected major elements from both the stainless steel and respective salts (K, Na, Zr, F, O, C, Ni, Cr, Zr, Mn). For clarity, results presented in Figures 4.17, 4.18 and 4.19 only include Fe, Ni and Cr. Zr was also included for NaF-ZrF₄ as the salt does not dissolve away in the presence of water during sample polishing like FLiNaK. Values are recalculated with the removal of carbon content since an unknown carbon contaminant was present on the surface of the sample after preparation. The contaminate resulted in high carbon concentrations where carbon is expected to be low, such as the steel regions. If carbon was not included in the scans, other elements appeared to be inaccurately determined. Re-calculated values are additionally normalized to the regions of uncorroded stainless steel. As a result, relative values across the scanned region are only considered. Initial scans of all elements are provided as supplementary information in the Appendix.

As shown in the scans, chromium is the primary element lost during measurements for both salts. For FLiNaK, this is much clearer as the salt no longer remained inside the pores. When the salt is left behind, such as the case for NaF-ZrF₄, the results show a decrease of iron in these regions as well, likely due the residual salt blocking surfaces of the tube. Based on this, there is likely some Fe loss on the tube surface in both salts. Some indications of higher iron losses were also observed closer towards the outer wall of the tube where Ni content (green) appears to increase.

For each tube, the maximum quantity of impurities that could be introduced into the salt was determined based on the estimated volume of the pitted region and the

expected composition of Stainless Steel 304. In the FLiNaK tube example provided, the region is estimated to have a $15\mu\text{m}$ deep corroded section 25mm long. If all the Cr in this region (18 mol% of the steel) were to be present in the salt after measurement, an estimated maximum chromium content of $2.86\text{E-}5$ molar percent could be expected. Similarly, the same analysis on the NaF-ZrF₄ tube estimated a maximum possible Cr content of $1.91\text{E-}5$ molar percent based on a $10\mu\text{m}$ deep corroded region 25mm long. In addition, the EDS results for the NaF-ZrF₄ tube suggests an average Fe is of this region approximately 50%, suggesting the maximum Fe content in the salt would be approximately $3.6\text{E-}5$ molar percent (where Fe is 68 mol% of the 304 Stainless Steel). Because this analysis overestimates the possible impurity content, the impurity level is expected to be much lower. As a result, the change composition due to corrosion product impurities is expected to have no noticeable effect on measurement quality.

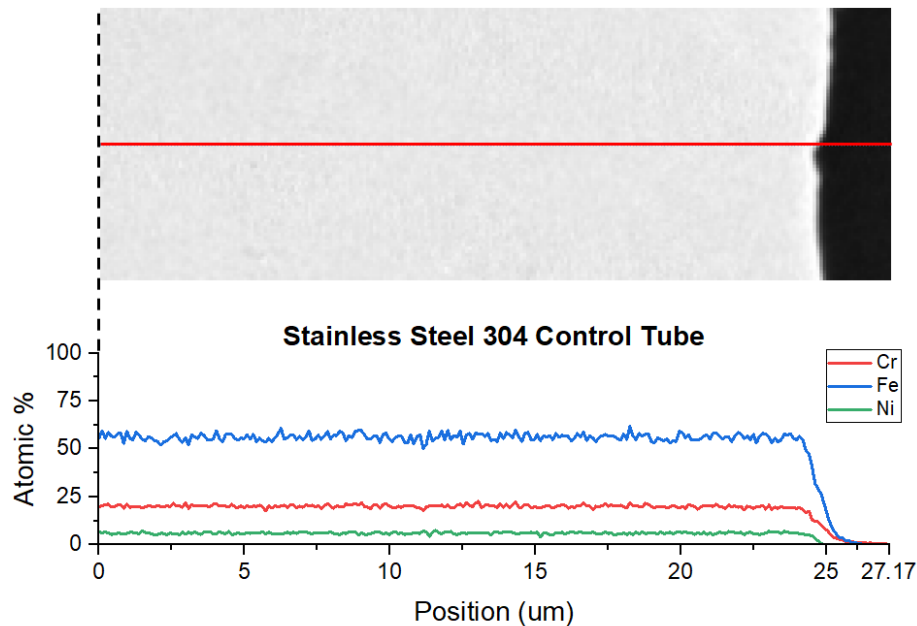


Figure 4.17: EDS Line scan of outer edge of a Stainless Steel 304 control tube showing only Cr, Fe and Ni content.

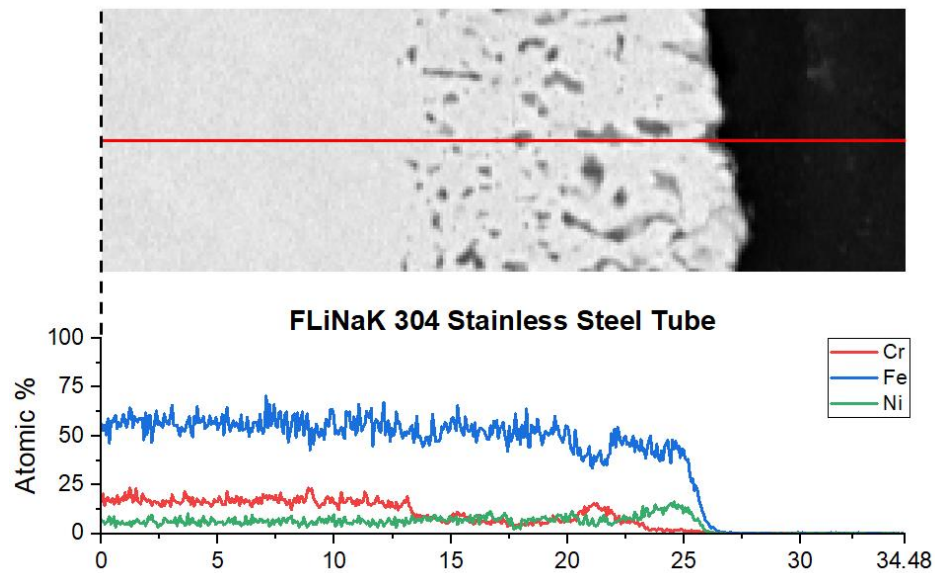


Figure 4.18: EDS Line scan of outer edge of a Stainless Steel 304 control tube showing only Cr, Fe and Ni content.

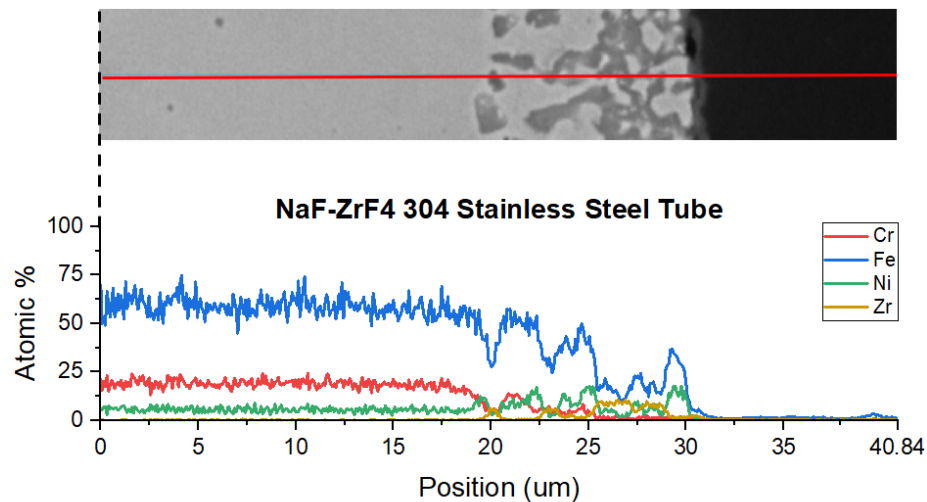


Figure 4.19: EDS Line scan of outer edge of a Stainless Steel 304 used with NaF-ZrF₄ showing only Cr, Fe and Ni content. Cr and Fe content appear to decrease in corroded region where pitting occurs. Where Fe decreases Zr increases, indicating Fe results are affected by the presence of Zr on the surface.

4.7. Discussion

The density measurements for each salt mostly coincides with previous measurements, with lesser agreement for both sets of surface tension values.

Density measurements of FLiNaK agree very well with studies that consider surface tension corrections. Surface tension values show lesser agreement with FLiNaK measurements. The surface tension values are generally lower and have a steeper decrease with increase of temperature.

Compared to FLiNaK, density values for NaF-ZrF₄ do not agree as well with former studies, however recent studies of this composition are limited. The measured values have better agreement with lower Zr content salts with lower error but have fewer measured temperatures compared to FLiNaK; therefore, effecting the accuracy of the trend line with temperature. Surface tension measurements as a function of temperature for NaF-ZrF₄ share a similar slope to values reported by Barborik (a slightly different composition) but have slightly higher overall values.

It is likely that any measurement uncertainty from both salts is associated with instabilities at the solid-liquid or gas-liquid interfaces during bubble formation. Corrosion identified on the tubes could have also caused inconsistent bubble release due to change in salt composition at these interfaces or may have affected its property values.

Additionally, the effect of corrosion may be inconsistent over different temperatures where the corrosion rate is likely to increase with an increase in temperature. It must be noted that an increase in capillary diameter is likely to be minimal based on the observed corrosion, and most likely isn't a major source of error in surface tension values.

Additional capillary interactions of the salts, reference wire, and bubbling tube may have also affected results, adding to variability in salt height as the tube was lowered. These capillary forces may also affect the identification of surface location due to the curvature

of the meniscus at the top of the fluid. If the tube is not perfectly centered, the upper portion of the curvature is likely to be touched first.

Lastly, flow rate is known to affect surface tension results. Even a 1mL/min flow rate may have not been low enough to provide comparable values to those from other studies. As many examples in this work show, bubble formation times are usually 2-6 seconds, not the formerly suggested 30 seconds or longer. Even though this is the case, surface tension values for room temperature experiments match expected values at these faster formation times, suggesting this may not be an issue. Even higher flow rates, such as 6 mL/min flow rates may be required to produce a large enough difference. More data at higher flow rates would be required to draw a concrete conclusion, especially with minimal data collected using the 6mL/min flow rates.

4.8. Maximum Bubble Pressure Measurements Summary

The goal of this study was to measure density and surface tension at the same time to account for the influence of surface tension. This was done using the maximum bubble pressure method. Measurements on salts suggests that this approach works well considering similarities in the density values while results showed some differences in surface tension values. Similar findings were observed in the recent report provided by Rose et al. [27] which provides data that suggest a different method to account for surface tension when using the Archimedes method. This also agrees with the findings of this work showing differences in the acquired surface tension values could be associated with dynamic vs static measurement conditions. Because surface tension typically provides minimal error in the Archimedes method when small wire diameters are used for density

measurements, small variations in density are likely not associated with surface tension, or approximate surface tensions are considered acceptable. For the most accurate measurements, further investigation in this matter would be worth considering, especially on salts with fewer published measurements, such as NaF-ZrF₄.

5. HIGH TEMPERATURE FALLING BALL VISCOMETER & VISCOSITY

5.1. Introduction

There is a resurgence of interest in molten salts in energy sector technologies [1, 3, 66] including Molten Salt Reactors [45, 67] bringing a need for rapid material research on these systems. Thermophysical properties such as density, surface tension, heat capacity and thermal conductivity are key areas of study for these materials, both experimentally and theoretically. Viscosity is one thermophysical property that is highly correlated with molten salt speciation and structure, and influences the salt lifecycle and recycling, and general mechanical design of the reactor system [15].

Two common methods for measuring the viscosity of these molten salts employ rotational rheometer [26, 31] and oscillatory damped viscometer [32, 38]. While both methods have been proven to be reliable, they pose inherent issues for use with molten salts. Rotational rheometers typically follow the cheaper method of purchasing a commercial instrument and modifying it with a furnace to accommodate the high temperature needs or purchasing the more expensive system with the furnace together [68]. These systems require multiple load measurements to be taken at different angular velocities of a rotating spindle in a steady state condition. Due to the number of individual data points, these measurements can take more time at a given set temperature and have varying levels of accuracy based on operating parameters.

An oscillatory damped viscometer measures the damping effect of the molten salt on an oscillating cup at a known rotational frequency. Since these systems still require appropriate steady state behavior, multiple test frequencies are not necessarily required

like rotational viscometers. However, rotational variance due to friction and environmental damping can lead to error due to other effects if not appropriately accounted for, especially when factoring thermal effects of temperature.

Both methods require vessel and spindle, and containments need to be carefully considered for use with the molten salts. These customizations and commercial high temperature versions can considerably increase the cost and complexity of these systems.

More recently there is additional work on a rolling ball viscometer with a controllable incline to control the rate, and therefore Reynolds Number (Re). This method shows initial promise since it allows for high control over a range of Reynolds conditions, in this case using a calibration method to relate specific Re conditions to viscosity over a range of Re above the Stokes flow or creeping flow regime ($Re > 1$). System material and sensing mechanisms can also be easily changed based on salt requirements. [34]

Like the rolling ball viscometer, the classic falling ball viscometer is one alternative that has not yet been fully explored in depth for measuring molten salts. This method typically depends on Stokes Law for the estimation of drag force on the ball. For fluid samples bound in a tube with a circular cross section, like most examples for this method, the Faxen Correction Equation is utilized to account for the effect of a circular vessel wall on the fluid flow, often called the wall effect [69]. While this method has been shown to be highly accurate under Stokes Flow conditions, the low Re regime highly limits the effective use of this method. To maintain low Reynold's numbers, the fluid either needs to have a high viscosity, or have a minimized difference between the

sphere (ρ_s) and fluid (ρ_f) densities. Unlike other methods, falling ball viscometers do not require various testing states, and most of the effect of temperature can easily be accounted for by simple thermal expansion changes. They are also easily adaptable to a wide range of materials and measurement methods [70, 71].

Additionally, there is significant research in flow around a sphere at a wide range of Re numbers. Because of this there have been many attempts at designing formulas and methods to apply this concept to higher Re ranges, including calibrating the systems to unbound Reynolds number (Re_∞) behavior, or creating fitted trends to experimental data [72, 73]. Because of the wide span of flow behaviors observed over varying Re ranges, including flow separation, attached and unattached eddy currents and flow oscillations [74], most empirical models don't reflect all regions of flow accurately or are represented by a complex relationship between viscosity and velocity. Additionally careful design considerations must be made to ensure these flow regimes do not become dominated by inertial or velocity dependent drag as flow becomes more complex.

This work presents a low-cost, high-measurement rate falling ball viscometer method adapted to take high-temperature viscosity measurements that minimizes sample size, shortens measurement time compared to existing measurements at each temperature (focusing on actual measurement time, not temperature settling time) and is easily adaptable to various material requirements. This method expands on the classic falling ball viscometer method, using experimentally validated computational fluid dynamic methods (CFD) [75, 76] to represent the relationship between velocity and viscosity for a higher range of $Re_{ball}(<325)$ with a custom-made solenoid coil sensor for velocity

measurements. Like density and surface tension measurements, two fluoride salt candidates for Molten Salt Reactors (MSR) were tested as a proof of concept. The first is a well-studied general fluoride salt, eutectic LiF-NaF-KF (46.5-11.5-42 mol %, FLiNaK), used as a general application fluid including primary and secondary coolant applications [14]. The second is the lesser studied NaF-ZrF₄ (53-47 mol%) representing the fuel salt carrier candidate NaF-ZrF₄-UF₄ (53-41-6 mol%) used in the Aircraft Reactor Experiments from the 1950s [6, 22, 23] with different variations still considered today. The accuracy of this method is demonstrated by comparing experimental results to simulated viscosities from MD modeling and results from previously reported studies.

5.2. Material Synthesis and Analysis

Materials are synthesized with procedures mostly follow those used by Argonne National Lab [26]. Samples for both NaF-ZrF₄ (53-47 mol%) and FLiNaK (46.5-11.5-42 mol%) were prepared in an Argon filled glove box with 1ppm or lower of O₂ and H₂O. Precursors are obtained as single component powders from Sigma Aldrich. Each precursor is baked on a hot plate at 280 °C for 2 hours in a Ni-200 crucible that was polished with high grit sandpaper and then cleaned thoroughly to remove oxides. After baking, the reagent salts are weighed and mixed. The mixture is added to a similarly polished and cleaned Ni-200 crucible and melted in a furnace in the glove box, first additionally baking the sample at 280 °C for 1 hour then raising the temperature to 100 °C above the respective melting point for 2 hours. Samples are crushed to powder using a nickel mortar and pestle to help guarantee uniformity for next steps.

The crushed salt mixture is then added to fill a Boron Nitride (BN99 or HCBN)

crucible that is 150mm tall with 9mm ID and 14mm OD. Enough salt to have 4 inch (100mm) high column is then melted inside the glovebox at approximately 100 °C above the respective melting point and held for 2 hours before returning the BN crucible to room temperature.

Representative samples of as prepared and post measurement salts were analyzed for impurities and composition with XRD, examples shown in Figure 5.1 and 5.2. Only NaFZrF₄ was analyzed with SEM/EDS and not FLiNaK because it is found to be too hygroscopic, as described in Section 3. Some representative samples were also analyzed by DSC/TGA. Additional measurements on some samples were analyzed with ICP-OES methods to guarantee procedural accuracy. At each melting step mass is measured to verify no mass loss occurs due to reactions or volatility. Additionally, samples are visually inspected for any discoloration or obvious particulate in the samples that could indicate impurity interactions. Additional results are as described in Section 3.

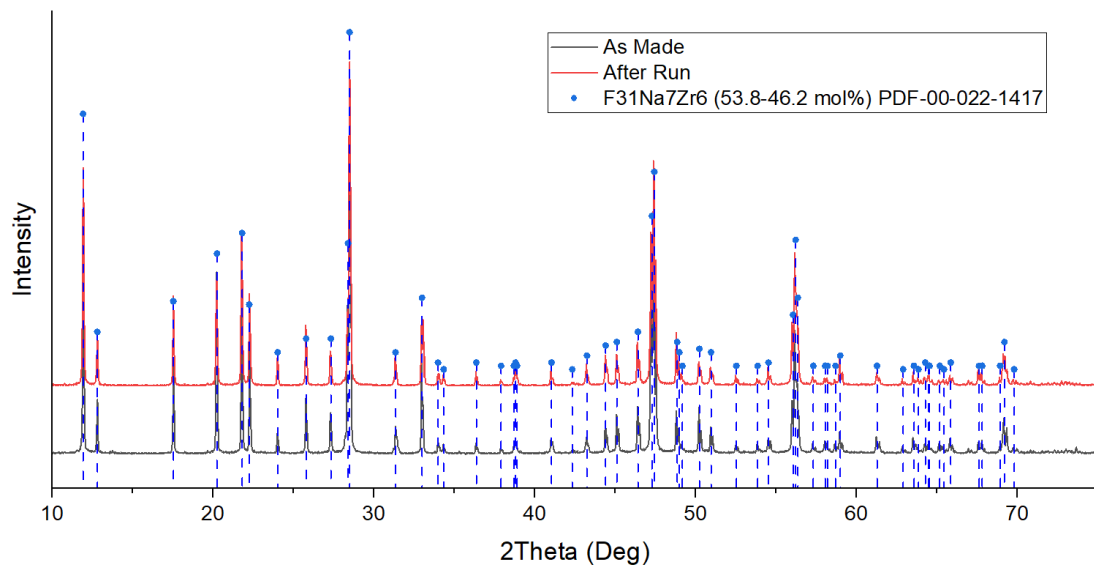


Figure 5.1: XRD of NaF-ZrF₄ (53-47 mol%) of as made salt sample compared to after run sample, with Na₇Zr₆F₃₁ PDF used as a baseline for comparison.

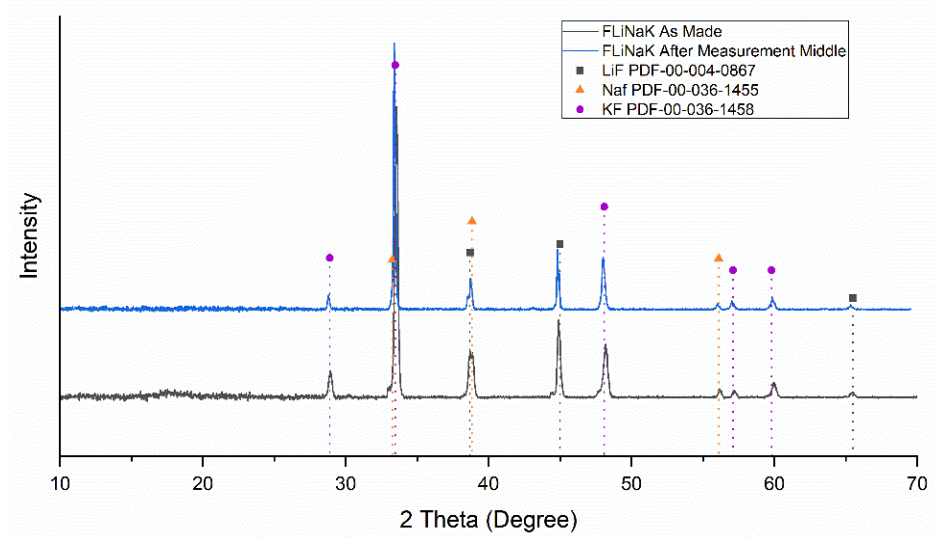


Figure 5.2: XRD of FLiNaK of as made salt sample compared to after run sample with appropriate precursor PDF comparison.

5.3. Falling Ball Viscometer Theory, System and Calculations

The falling ball viscometer is designed for use in a small form factor inert glove box environment. A customized furnace was developed to support the required temperature stability and viscometer geometry needed. Additionally, this furnace was designed around the need for sample preparation and to accommodate additional future property measurements. Functionality of the furnace additionally must not interfere with the operation of a small form factor glove box. The viscometer, as shown in Figure 5.3, consists of a ball drop mechanism to quickly load and drop the 3mm Ti spheres (balls) into the molten salt near the fluid surface. Two solenoid coils with calibrated spacing are used to detect the presence of a metallic sphere [24] by measuring the change in voltage through the coils using a detection circuit driven by an Arduino Uno microcontroller. The voltage signals are then post processed and a velocity is determined. Using the fluid flow model representing the physical relationship, the measured terminal velocity is used to

derive the corresponding viscosity at each temperature. Each component is described further in the following sections.

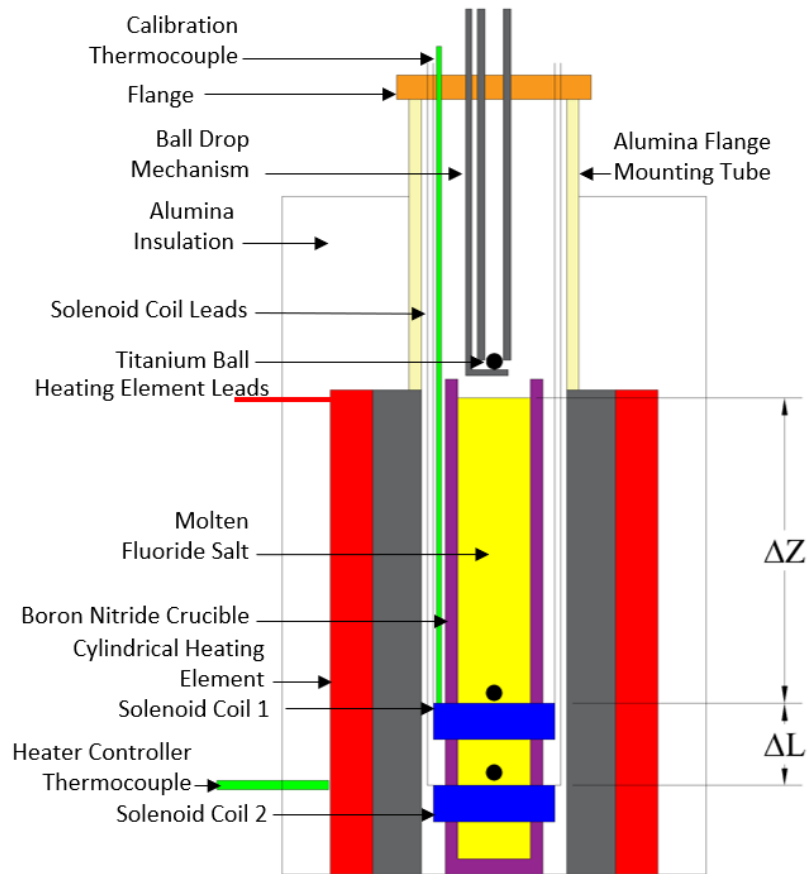


Figure 5.3: Diagram of high temperature falling ball viscometer design (not to scale) illustrating the basic setup of the vertical cylindrical heater, thermal conductor with cavity for the sample and solenoid sensors as positioned inside the glove-box sized furnace.

5.3.1. Velocity – Viscosity Relationship: Modeling & Validation

The typical viscosity (η) - velocity (U) relationship that utilizes Stokes Law to represent drag force in the Creeping Flow Regime or Stokes Flow is used to inform the numerical model. For a sphere of radius (r_s), a force balance relationship (5.1) is used, showing drag force F_D (5.2), buoyancy force F_B (5.3) of a fluid with density ρ_f , and gravitational acceleration F_g (5.4) of the sphere with density ρ_s . For flow with Reynold's

Number (5.5) beyond Stokes Flow an additional factor for the drag force due to flow separation and increasing turbulence K is often applied. [77]

$$(5.1) F_D - F_B = F_g$$

$$(5.2) F_D = 6\pi\eta r_s UK$$

$$(5.3) F_B = \frac{4}{3}\pi r_{bs}^3 \rho_f g$$

$$(5.4) F_g = \frac{4}{3}\pi r_s^3 \rho_s g_z$$

$$(5.5) Re = \frac{2\rho_f U r_s}{\eta}$$

An accurate representation of the K factor requires a reasonable solution of the Navier-Stokes equations (5.6) across a range of different flow behaviors that present as Re increases. [77]

$$(5.6) \rho_f \left(\frac{\partial \vec{v}}{\partial t} \right) + \rho_f (\partial \vec{v} \cdot \nabla \vec{v}) = -\nabla P + \rho_f \vec{g} + \mu \nabla^2 \vec{v}$$

To eliminate the need for experimental determination for K , a numerical model with these considerations is utilized. In COMSOL, using the Laminar Flow fluid module, the force components from Stokes Law are applied to represent the appropriate flow. With a fixed reference frame at the center of the sphere, a no slip condition is applied to the surface of the sphere. A translating wall with a no slip condition is applied to the crucible surface. The inlet of flow is assigned to the bottom of the crucible with the outlet at the top, indicating flow in a positive axial direction. Global weak constraints are applied to establish the correct relationship between displacement (5.7), velocity (5.8) and gravitational acceleration (g). [78]

$$(5.7) \mathbf{X}(t) = \mathbf{X}(t-1) - t\dot{\mathbf{X}}(t)$$

$$(5.8) \dot{\mathbf{X}}(t) = \ddot{\mathbf{X}}(t) - \left(\frac{F_D}{V_s \rho_s} - \frac{F_B}{V_s \rho_s} \right) t$$

Fluid temperature is represented by density at the given temperature, $\rho_f(T)$.

Geometric parameters are defined to reflect nominal or as measured values of the physical system with thermal expansion corrections for the sphere and crucible respectively (5.9).

$$(5.9) r_{eff} = r_{nom} + r_{nom} \alpha \Delta T$$

The resultant drag force (5.10) and local velocity is then determined through COMSOL's solver. Based on the calculated results, the maximum possible velocity of the ball is determined to be the velocity of the flow at the inlet.

$$(5.10) F_{drag} = \iint_{S_{sphere}} \tau_{wz} dS_{sphere}$$

Shear force is determined in COMSOL by first determining the friction velocity matrix along the surface (u_τ) (5.11) based on the local shear at the wall, then finding the direction component of the shear (τ_{wz}) (5.12). [79]

$$(5.11) u_\tau = \sqrt{\frac{\tau_w}{\rho}}$$

$$(5.12) \tau_{wz} = \rho u_\tau^2 \frac{u_z^T}{u^T}$$

Using this model, a lookup table is generated by solving for a velocity over a range of viscosities at a given fluid density. The measured velocity is then used with this table to interpolate the corresponding viscosity value. To check the accuracy, the model can be re-run using this derived viscosity, and the resultant terminal velocity can be

compared to the measured velocity.

Validation of this model was performed using water (1cPs) and Brookfield silicon oil standards (PN) with viscosities of 4.8 cPs, 9.4 cPs and 96 cPs using a room temperature version of the viscometer. Different ball materials including Aluminum (Alloy 2017) and Titanium (Alloy Gr-5) with a 3.175mm (1/8") diameter and acrylic tube diameters (5mm and 9mm) were used to reach a range of Re regimes to represent the expected range during the high-temperature experiments. It was found that the overall average remained accurate to the standards with good agreement between the COMSOL model and room temperature experiments for Re up to 257 (limitation set by room temperature properties of available materials), as shown in Figure 5.4. Some high-temperature experiments may exceed this Re range slightly (Re = 300) but since the flow regime is similar, the error is expected to be acceptable from the model in those ranges; the regime correlates with the start of turbulent flow from other studies focusing on flow regimes around a sphere [77, 78]

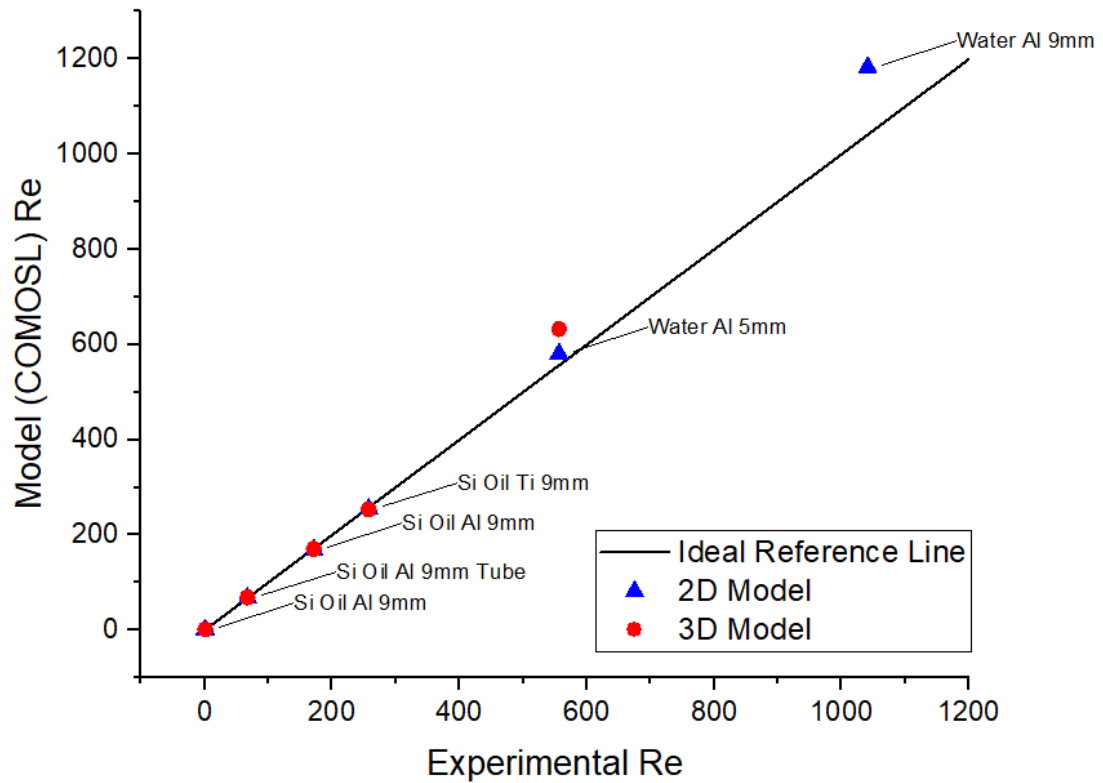


Figure 5.4: COMSOL derived velocities of Brookfield Standards compared to room temperature experimental results.

The similarity in flow conditions further validated with COMSOL. Additional simulations were performed using a 3D version of the axisymmetric simulation with the same boundary conditions. Simulations showing several of these higher Re ranges are shown in Figure 5.5. For a Re of 257, the highest condition where experiments and simulations match, the flow regime remains axisymmetric. As Re increases slightly, such as for a Re of 276, only a slightly deviation in symmetry is observed. It is not until the Re greatly exceeds these values, around a Re of 556 where the 2D and 3D models begin to show extreme deviation from experimental values (around 4% difference). This higher Re condition shows that more periodic or turbulent flow is observed, indicating this Re region would not be accurately represented by the laminar COMSOL simulation package.

From this evaluation, it was determined that using the COMSOL model for Reynolds numbers near 300 was likely to provide minimal error in results compared to room temperature experiments. This means that the upper limits of the Re numbers expected for high temperature experiments (FLiNaK: $Re = 329$; NaF-ZrF₄: $Re = 217$) are within a range that the COMSOL model can represent, where the upper limits of FLiNaK will start to deviate from experimental values minimally.

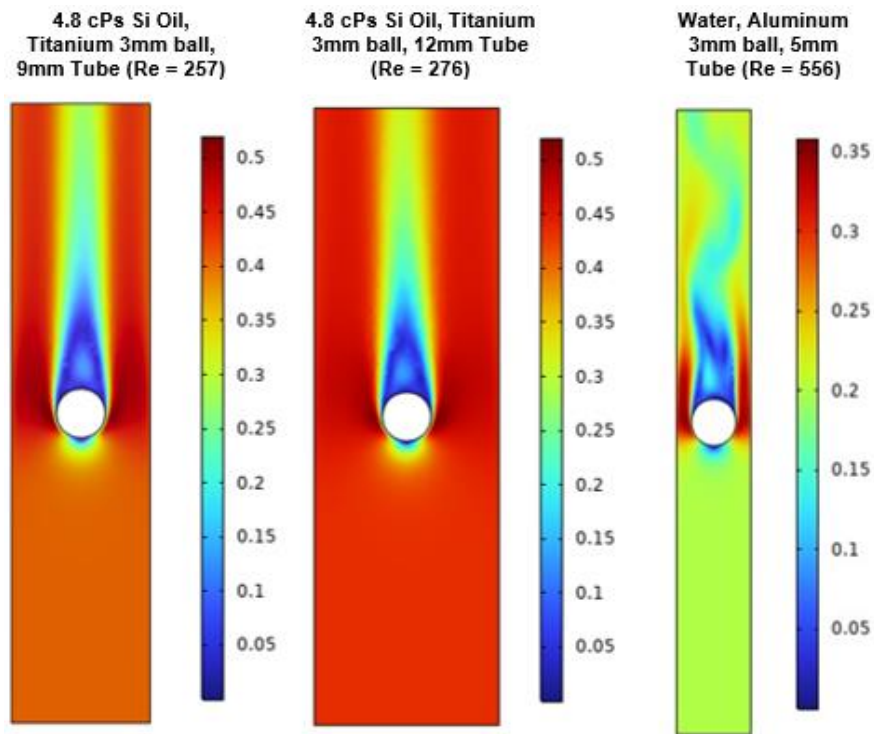


Figure 5.5: Extended verification of model using COMSOL simulation to evaluate the flow conditions of different Re numbers.

5.3.2. Ball Drop Mechanism

The drop mechanism, shown in Figure 5.6, is made from a combination of 304 and 400 series stainless steel that allows multiple balls to be loaded prior to loading the assembly into the furnace. A carousel mechanism is rotated 180 degrees to load an individual ball from the loading tube to the dropping tube, which has the lower end

positioned directly over the molten salt inside the BN crucible. A lever is then actuated to drop the ball from the dropping tube (opened condition). When complete, the lever can be reset (closed condition), and another ball loaded without opening the furnace. This helps to maintaining temperature stability, minimizing impurities in the salt and optimizes the data collection rate.

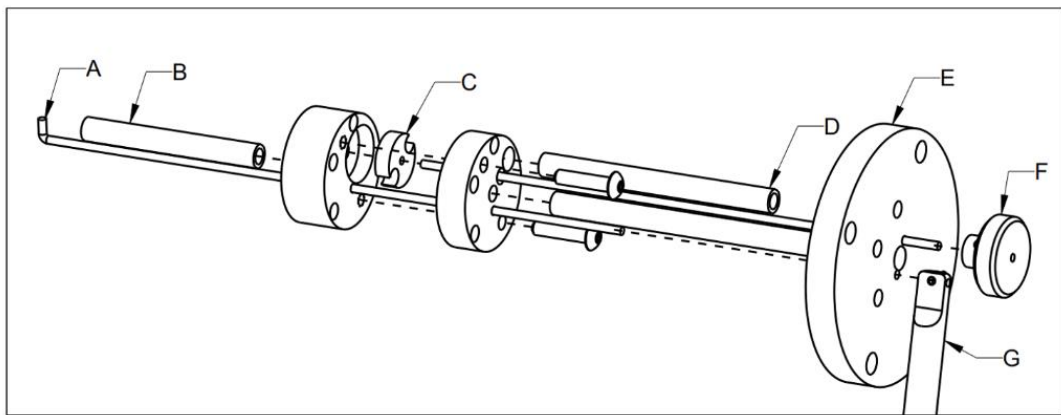


Figure 5.6: Ball Drop assembly exploded view A) Dropping rod B) Load ball in this tube before dropping C) Loading Mechanism D) Tube for balls waiting to be loaded E) Mounting Flange F) Knob for loading balls G) lever for turning dropping rod.

5.3.3. Sensing Device: High Temperature Solenoid Coils

The sensor component consists of two solenoid coils made from 30-gauge Ni-200 wire. Other easy to form wire materials including copper or stainless steel were shown to have higher levels of corrosion or significant loss of yield strength resulting in lead breakage.

To fabricate the coils, steps depicted in Figure 5.7 are employed. The wire is wrapped around a 14mm blank, the same diameter as the crucible. This way the coils are tight against the crucible, maximizing signal sensitivity. The coils are each made with approximately 12.4mm (1/2") long wires leaving a gap approximately the size of the wire

gauge between each turn to prevent shorting, resulting in about 18 to 20 turns for each coil. To hold the coil shape, the wire is encapsulated with ceramic paste (AREMCO Ceramabond 552-VFG). After drying of the ceramic paste, the space between the two individual coils is 2 to 5mm apart. Excess wire is left unwrapped to act as leads for each coil and fed through 1/8" double bore alumina tubes. The alumina tubes are pasted in place, parallel to the axis of the coil. The whole assembly is then fired in an Ar atmosphere following the curing procedure of the paste.

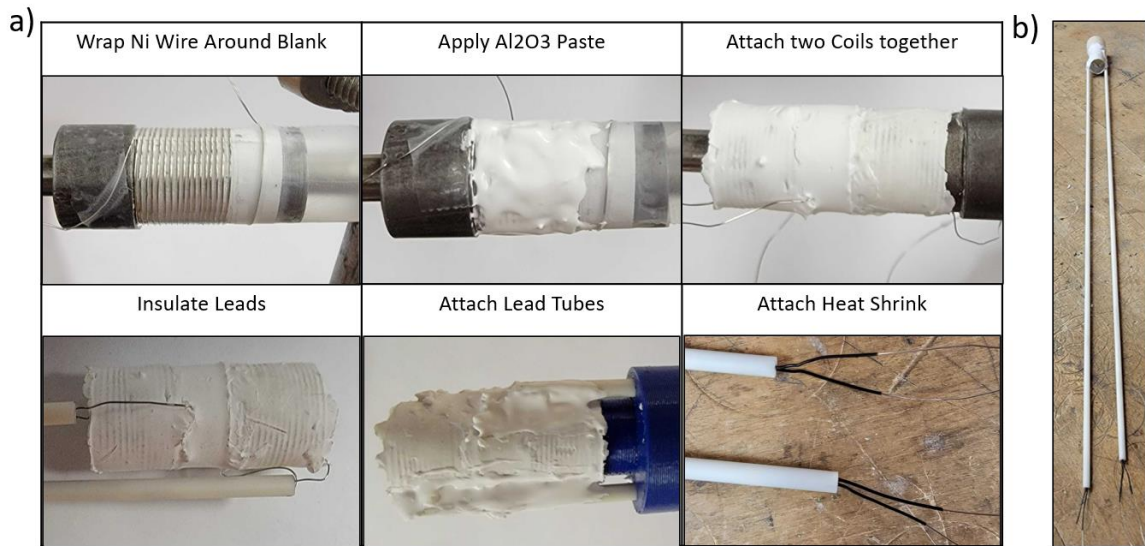


Figure 5.7: Assembly of (a) solenoid coils from start to finish, excluding the curing steps and attachment of the bottom spacer and (b) the finished assembly.

The finished two solenoid assembly is then calibrated at room temperature using a linear actuator driven by a stepper motor with a set velocity expected from the same Brookfield viscosity standards used to validate the COMSOL model. The spacing between the coils (ΔH) is calculated from the set or expected velocity. (5.13) The same principle is applied for determining velocity from the measurements using the calibrated ΔH .

$$(5.13) \Delta H = v_{expected} \Delta t$$

When the ball is at the center of one of these coils, the signal observed using the detection circuit is observed to be the minimum point. The circuit and signal analysis for determination of the minimum point are described in Section 3.4.

5.3.4. Ball Detection

To determine the time for the ball to fall between coils centers, each coil attached to an LC circuit, modified with a diode between the inductor and capacitor, as shown in Figure 5.7. Both circuits are controlled with an Arduino Uno as a micro-controller and excited with several square wave pulses for each measurement interval.

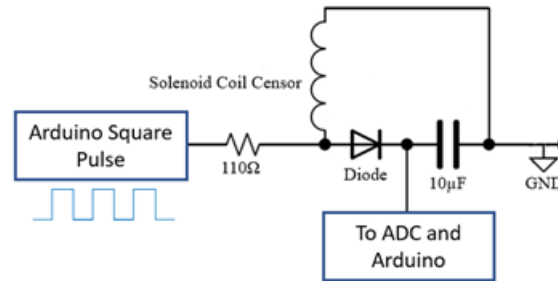


Figure 5.8: Circuit loop of modified tank circuit for proximity detection of metallic balls.

When the ball falls through the coil, a change of inductance ΔL is caused due to sphere material's volume percent in the magnetic field of the coil with N turns, cross sectional area A and axial length (h). It causes a change in the coil's average relative permeability $\Delta\bar{\mu}_r$ (5.14) and a change in the resonance frequency Δf (5.15) based on the capacitance (C).

$$(5.14) \Delta L \propto \frac{\mu_o \Delta\bar{\mu}_r N A}{h}$$

$$(5.15) \Delta f \propto \frac{1}{2\pi\sqrt{\Delta LC}}$$

This is observed as a change voltage ΔV due to a change of impedance ΔX_L (5.16) (5.17) with constant current (I). Additionally, frequency may also change based on the change of inductance.

$$(5.16) \Delta V_L = I\Delta X_L$$

$$(5.17) \Delta X_L = 2\pi\Delta f\Delta L$$

The change of impedance reduces the charge (Q) of the capacitor of capacitance C , indicating the presence of the sphere in the coil. Since the circuit is driven by frequency-based signal from the Arduino, the capacitor charge is built up after several pulses. The charge of the capacitor then amplifies the change in voltage from the inductor due to the dependence of voltage drop (ΔV_c) based on capacitor charge (5.18). Response time and sensitivity are optimized based on the capacitor size.

$$(5.18) Q = C\Delta V_c$$

The voltage over the capacitor is measured by passing the signal through a 16-bit ADC (PN: TLC4541) and recorded by the microcontroller. The time dependent series of data averages is then sent and saved to the PC for additional signal processing; the averages are saved to minimize data transfer through serial communication.

A post processing code is then used to find the relative minimum voltage, or the point when the ball is assumed to be at the center of the coil with respect to the z axis. Here, a low pass filter is implemented to remove much of the noise. (Signal Example: Figure 5.9) The low pass cutoff frequency is determined to be slightly higher than the

expected terminal velocity and 2 times the length of one coil (the sphere's position with respect to time represents $\frac{1}{2}$ a period in the signal), nominally 12.4mm (1/2") (5.19).

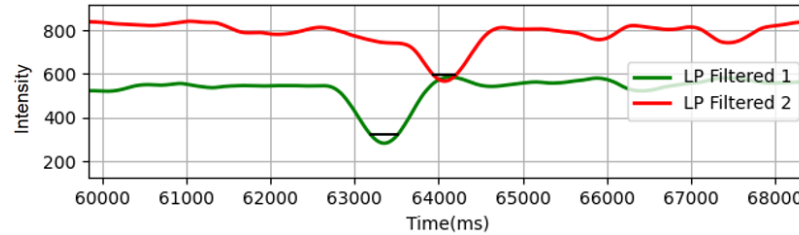


Figure 5.9: Dual coil signals example after post processing with Low Pass Filter for the appropriate frequency.

$$(5.19) f_{cutoff} = \frac{v}{2L_{coil}} = \frac{1}{t_{coil 2} - t_{coil 1}}$$

The expected velocity is determined with the COMSOL model and properties from previously reported studies, but the measured velocity must also agree with the cutoff frequency. The standard deviation is expected to be minimized at the point where frequency and velocity agree for a set of data points at a given temperature, showing agreement between measurements. (Figure 5.10)

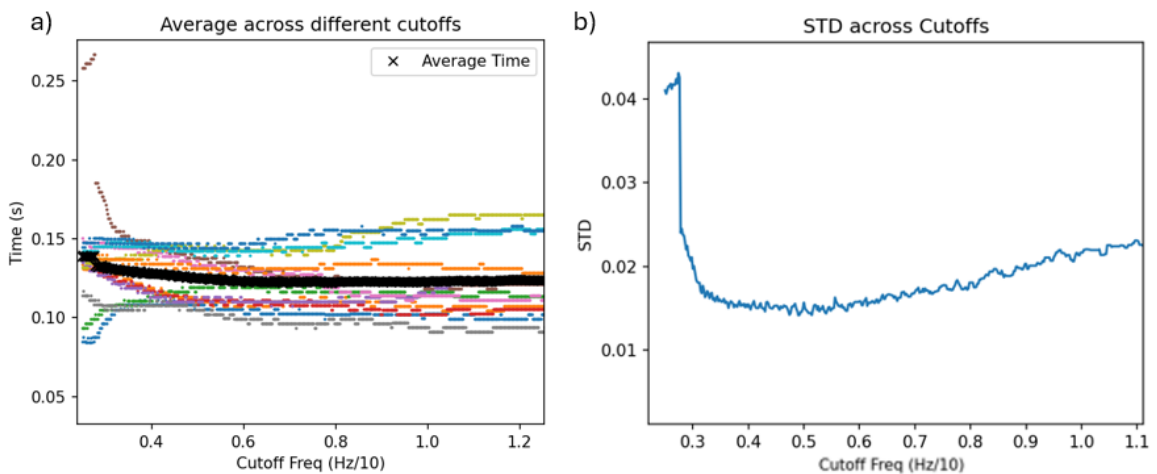


Figure 5.10: Example Data of 579 °C average temperature looking at all cutoff frequencies for the low pass filter. Data demonstrates convergence of Sample at the approximate cutoff frequency (0.47 Hz) as seen in the Standard Deviation.

5.3.5. *Falling Ball Viscometer Experimental Procedure*

The ball drop mechanism, sensor and Boron Nitride sample filled crucible are assembled as shown in Figure 5.11. This is inserted into the glove box furnace.

Temperature is then increased to the desired measurement temperature at 2C/min.

Temperature is held at the set temperature to stabilize prior to starting measurements. An additional thermocouple is inserted adjacent to the outer surface of the crucible just above the solenoid coils. Temperature of this thermocouple is observed during this stabilization period for changes. If no significant changes are observed, measurements are started.

Additionally, this temperature is digitally recorded as the fluid temperature. For each temperature, 2 to 3 spheres are dropped into the salt, restarting the data gathering program in between. It takes approximately 1 to 2 minutes to load and drop the ball. After completing measurements at each temperature, the temperature is raised or lowered to the next set point. Ball dropping is stopped when space beneath the bottom coil fills up, and the balls start to collect in the region detectable by the bottom coil. This is observed as the bottom coil signal starts to represent a step function or the signal not returning to the same baseline after the ball is detected by the coil.



Figure 5.11: Fully assembled ball drop mechanism with coil assembly A) Coil Assembly B) Ball Loading and dropping mechanism C) Lead Attachment to connect to Arduino circuit.

The minimum measurement temperature was 30 °C above the expected melting point. The maximum measurable temperature was determined by analyzing the variation

of ball velocity in the salt as a function of temperature. If terminal velocity is not being reached, the velocity begins to decrease with an increase in temperature. The point where this begins to happen is determined to be the maximum possible temperature due to an inadequate distance available in the column to attain terminal velocity because of limited drag from lower density and viscosity (Figure 5.12). This has been further verified with the laminar flow model (Figure 5.13).

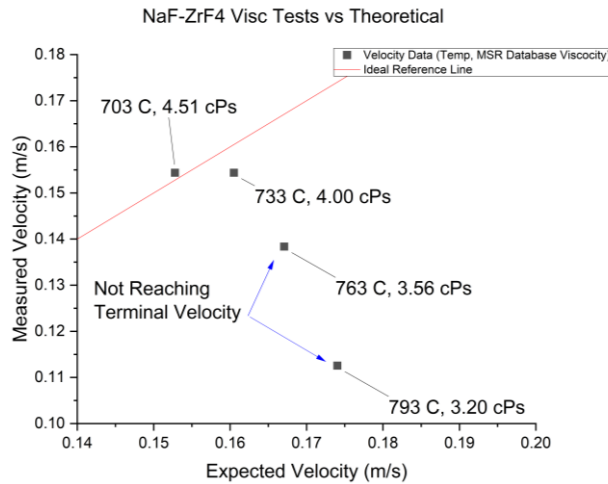


Figure 5.12: Results from validation testing of terminal velocity of NaF-ZrF₄ at elevated temperatures.

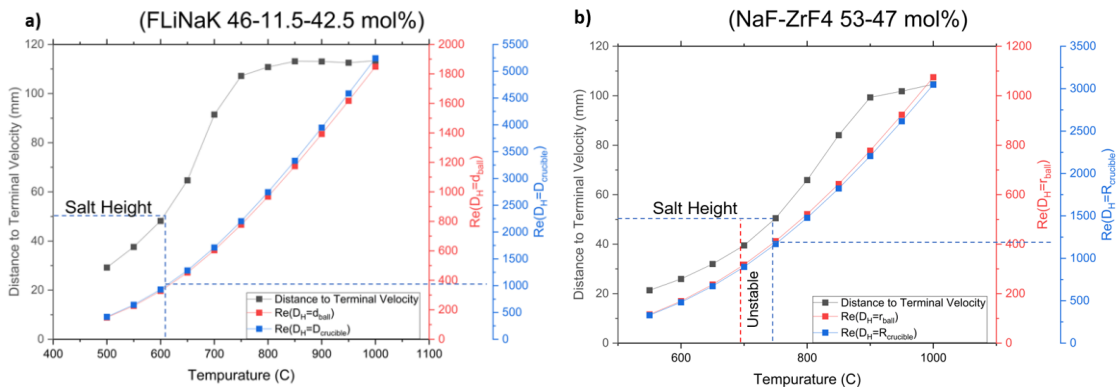


Figure 5.13: Prediction from COMSOL model of distance to reach terminal velocity and respective Reynold’s number as a function of temperature for FLiNaK (a) and NaF-ZrF₄ (b). Reynold’s Number confirms if the predicted velocity is in a reasonable range for the laminar flow model, and peak salt height is determined to be the salt height of the available molten salt at a given temperature based on weighed mass and reported density.

5.3.6. Molecular Dynamic Methods

Simulated viscosity values were determined using MD methods for both salts. Using the Matlantis platform, a universal neural network potentials (NNP) called Preferred potentials (PFP) [66] is used to evaluate the interatomic forces between ions in supercell. MD simulations are performed for eutectic FLiNaK and NaF-ZrF₄ 53-47 mol% ranging from 525 °C to 850 °C.

The initial configurations are generated from Packmol [29] with random structure and avoiding atomic overlap, which contains a total of 432 and 1056 atoms for FLiNaK and NaF-ZrF₄, respectively. The equilibrium volumes at different temperatures are selected from the existing literature (Janz (1988), Cohen (1956) [59]), the temperature dependent trend provided as Equation 5.20 and 5.21 respectively. All supercells were first equilibrated in NVT ensemble for at least 50 ps and then continued to run 100 ps by using reverse non-equilibrium MD (rNEMD) method [81] to obtain the calculated viscosity.

$$(5.20) \rho_{FLiNaK} = 2.53 - 0.00073 T[C] \left[\frac{g}{cm^3} \right]$$

$$(5.21) \rho_{NaF-ZrF_4} = 3.71 - 0.00089 T[C] \left[\frac{g}{cm^3} \right]$$

During the rNEMD, an artificial velocity gradient is generated between the bottom and middle (along the z direction) in the simulation box representing shear. Based on the movement the exchanged momentum can be defined as the momentum difference along the x direction between the bottom and middle (5.22).

$$(5.22) P_{exchanged} = P_{x,bottom} - P_{x,middle}$$

This momentum flux is proportional to the product of the viscosity and velocity gradient, where t is time, S_{xy} is the area of the x-y plane of the simulation box, v_x is the partial velocity along the x direction, and η is the viscosity (5.23).

$$(5.23) \frac{\sum P_{exchanged}}{2tS_{xy}} = \eta \frac{\partial v_x}{\partial z}$$

5.4. Viscosity Results

Experimental measurements are compared to former studies of the same or similar composition in the case of NaF-ZrF₄. Viscosity was evaluated based on the same density trends as used in the MD simulations (5.20, 5.21). An additional evaluation was performed using density correlations for each salt obtained from this work, as provided Section 4. For each material, experimental and MD data sets are fit to the Arrhenius Equation (5.22) for comparison. Results for FLiNaK, shown in Figure 5.14, show good agreement with literature data, but do not match any one study. Trends are extrapolated beyond experimental data ranges for comparison with rNEMD data. Table 5.1 shows the Arrhenius coefficients (5.24) including additional ones not plotted in Figure 5.14.

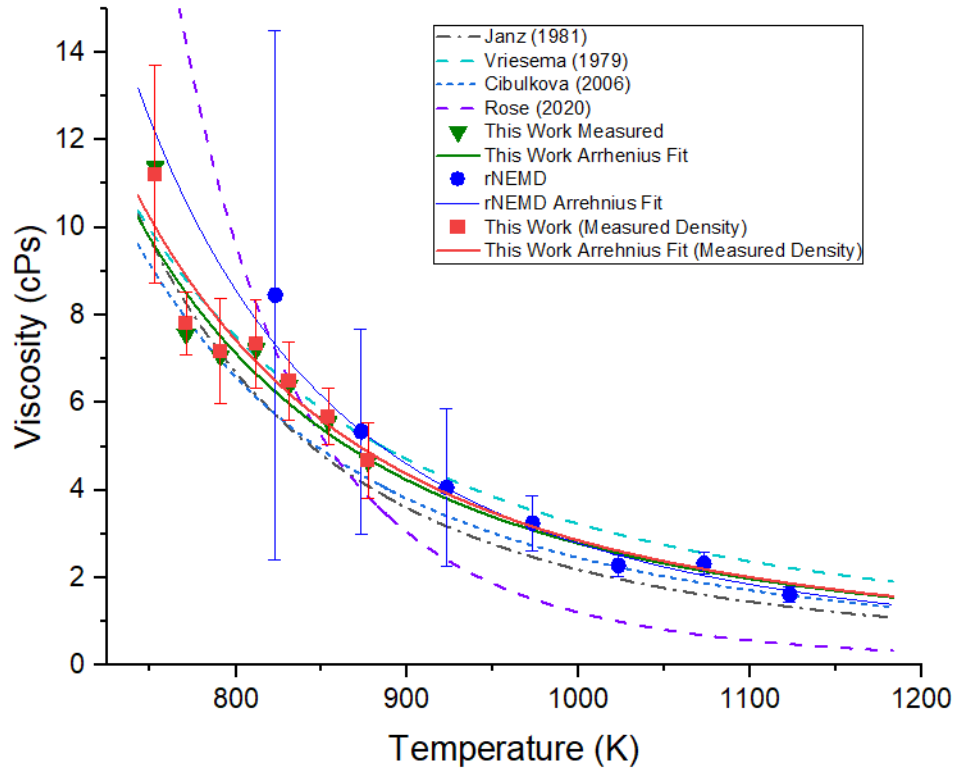


Figure 5.14: As measured FLiNaK viscosity as a function of temperature with an exponential-Arrhenius fit compared to selected former studies.

$$(5.24) \mu [Pa \cdot s] = A \exp(E/T [K])$$

Table 5.1: Viscosity [$Pa \cdot s$] FLiNaK Eutectic Arrhenius Coefficients (Equation 5.24)

Study	A	E
Janz (1981) [11]	2.48E-2	4478.62
Vriesema (1979) [11, 82]	1.1E-1	3379
Cibulkova (2006) [83]	4.74E-2	3947
Ambrosek (2009) [84]	4E-2	4170
Kubiřkovař (2012) [64]	3.80E-2	4565
Rose (2020) [26]	3E-2	8300
MD (This Work)	3.11E-2	4495.75
This Work (Measured Density)	6.206E-2	3828.7
This Work (Powers 1961 Density)	6.48E-2	3761.6

Similarly, results for NaFZrF₄ are plotted in Figure 5.15 with the relevant Arrhenius coefficients shown in Table 5.2. Similar compositions are shown in this case because of the limited information of the selected composition (53-47 mol%).

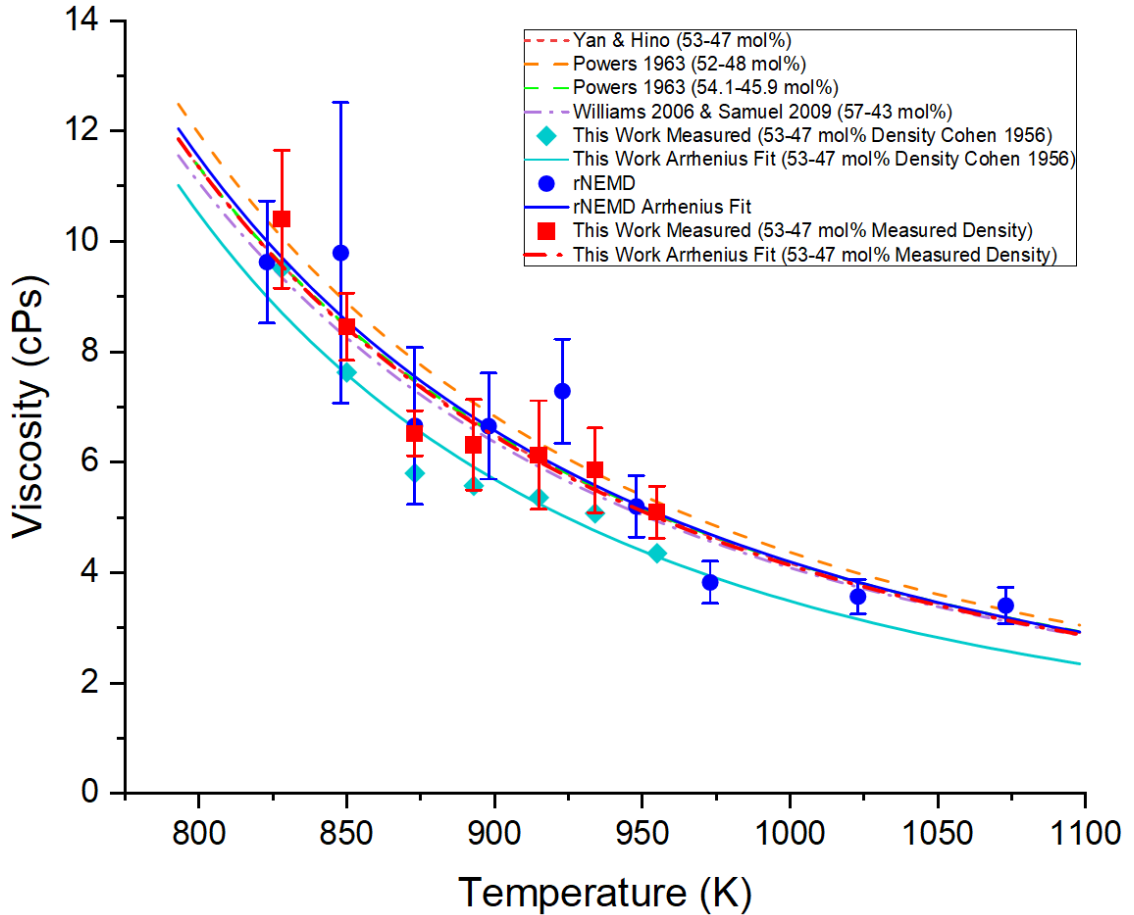


Figure 5.15: As measured NaF-ZrF₄ (53-47 mol%) viscosity as a function of temperature with an exponential-Arrhenius fit compared to selected former studies.

Table 5.2: NaF-ZrF₄ (53-47 mol%) and similar compositions Viscosity [$Pa \cdot s$] Arrhenius Coefficients (Equation 5.24)

Source	A	E
Powers (1963) [59]	7.8E-2	3984
Cohen (1956) (50-50 mol%) [59, 61]	7.09E-2	4168
Williams (2006) (57-43 mol%) [59]	7.67E-2	3977
Yan & Hino (2011) [59]	7.667E-2	3997
MD (This Work)	7.427E-2	4035.179
This Work (Measured Density)	7.323E-2	4034
This Work (Density Cohen 1956)	4.202E-2	4433.4

Standard error of mean is calculated with 95% confidence. Temperature variation, ball diameter tolerance and signal variation are the most impactful sources of error. The highest error occurs at the lowest temperature for both salts. Other factors not considered but likely minimal in comparison to the error include sensor spacing, convection and the accuracy of reported density values. End effects are also not accounted for.

The resultant Arrhenius trends from MD modeling shows good agreement to former studies where increasing temperature shows decreasing error. For both MD and experimental data, as the temperature approaches the melting point, error increases. Additionally, for FLiNaK, MD results deviate from experimental data at low temperatures. Measurements evaluated with as-measured density and the density described by Equation 5.21 provide minimal difference. In contrast NaF-ZrF₄ deviates at high temperatures. Percent difference between MD and experimental data for both salts is presented in Table 5.3 for select temperatures based on the given Arrhenius trends. Unlike FLiNaK, measurements evaluated with as-measured density show a more

agreeable viscosity correlation to literature, suggesting the density obtained in measurements of this work is more applicable for the given sample.

Table 5.3: Percent difference in viscosity at select temperatures between MD and experimental results evaluated with the same density.

Temperature (K)	FLiNaK Percent Difference	NaF-ZrF ₄ Percent Difference
825	16.93	9.08
875	11.14	12.13
925	6.22	14.92
975	1.99	17.49

5.5. Viscosity Discussion & Conclusion

This study demonstrates the applicability of a falling ball viscometer for making rapid measurements in high temperature molten salts. An accurate relationship can be established for this system between velocity and viscosity at Reynold's Number up to $Re = 300$ using numerical modeling methods. Additionally, there is good agreement with some variation between experimental results, MD results, and previously reported literature values.

Evaluating velocity data to obtain viscosity by using density correlations as determined in Section 4 provides stronger evidence of accurate measurements and consistent samples. NaF-ZrF₄ shows a significant difference in viscosity values between using densities from reported literature vs measurements from this work. The viscosity values with the as-measured density are almost the same as reported literature. In contrast, FLiNaK viscosity values evaluated with both densities is quite similar, mostly because density values are quite similar. This exemplifies the need for accurate density

measurements for this measurement method. As such, by performing density measurements in parallel to viscosity, a more accurate description of the salt samples is obtainable since there are fewer procedural variations from in house samples as opposed to external studies.

The variation in and between experimental results, MD results and other sources could be caused by many possible factors. Errs from experimental results could include non-optimal circuitry that causes variability in determining ball location due to noise from the Arduino power supply and the sampling method selected. Another cause could be related to volatility or reactivity that increases as temperature increases, more easily identified in NaF-ZrF₄. This salt is known to have increased volatility leading to loss of ZrF₄ at temperatures above 700 °C [11]. Additionally, these salts are susceptible to impurities from corrosion products, trace oxygen and trace moisture in the environment [38]. This effect of oxygen and moisture could not be completely removed from the glove box or from precursor materials, and results in the formation of oxyfluoride and oxide [5]. In these salts, impurities are more likely to target the larger cations (K and Zr respectively). Experimental samples are expected to end up with a loss of large cation-fluorine bonds, effecting the viscosity results [20, 85]. While our samples do not show significant change in composition by EDS and ICP analysis, excessive variation in composition could cause enough deviation to see a difference from the ideal compositional represented in rNEMD simulations or experiments with higher environmental control.

The general factors affecting the MD results are simulation time and supercell size (number of total atoms in systems), short time and small cells may not be able to represent the properties of bulk material sufficiently. Another possible factor is the accuracy of PFP potentials in Matlantis; even though the potentials are trained directly from DFT, some accuracy and description must be sacrificed to improve the calculation speed. As for the larger error bar at relatively low temperatures especially around the melting point of the salts, low temperatures may cause some ions' kinetic energy to be very close or even lower to the diffusion barrier, thus these ions will have low self-diffusivities compared to others and resulting large discrepancy of diffusivities of overall same type ions; finally, this difference will also be reflected in the viscosity results.

Future work with results from studies of x-ray measurement techniques of similarly prepared samples and MD simulations intends to explore these relationships between liquid atomic structure and thermophysical properties further [18, 19].

Similarly, sphere and crucible material may need to be reconsidered especially if working with alternative molten salts. Titanium was selected for this study based on its high melting point and low density to minimize the difference between ρ_{fluid} and ρ_{sphere} so that terminal velocity is achieved in a shorter distance and Re is minimized. Ti is known to not have good corrosion resistance with fluoride salts, particularly FLiNaK [51]. For this method, due to the quick sampling rates, the duration of salt exposure to Ti in this experiment is limited (several hours if changing between several temperatures) and is likely to have minimal effect. Post-measurement characterization of the salts shows no measurable amount of Ti in either salt, but trace amounts could still be present.

If the ball material is changed, it is believed that the system can be scaled accordingly to accommodate denser spheres that may otherwise take longer to reach terminal velocity. The extent of this would need to be determined. The measurements in this work only test $Re < 300$ and a $r_{sphere}/R_{crucible}$ ratio of up to 33%. In these cases, sphere and crucible diameter can be modified, but a more sensitive detection method would be required for smaller diameter spheres. Even with this consideration, there is a limit to the range achievable. As Re increases the viscous component of the drag becomes negligible. Also, the dynamics change in the vicinity between the ball and crucible wall as the $r_{sphere}/R_{crucible}$ ratio increases.

In conclusion, this work has demonstrated the ability for a falling ball viscometer to be applied to a high temperature application for fast, reasonably reliable measurements, but requires additional considerations to improve accuracy and applicability.

6. CONCLUSIONS AND FUTURE WORK

6.1. Conclusions

This work demonstrated successful implementation of high-measurement rate techniques to provide density, viscosity, and surface tension of high-temperature molten salts as a function of temperature. These well-known techniques were uniquely adapted for function at elevated temperatures and for use with these salts, resulting in novel systems specific to the molten salts studied herein. Additionally salt samples were characterized before and after measurements to provide evidence of sample quality and possible error sources that may have occurred during these measurements.

Density values obtained with the maximum bubble pressure method provide good agreement with several reported literature values on similar salt compositions. Specifically, the measured values are closest to those that reportedly account for surface tension. However, Surface tension measurements obtained simultaneously in this work differ from published studies. This could be associated with measurement uncertainties and/or variation in testing parameters which are not clearly specified in the published work. Alternatively, limited available comparable measurements for this property do not provide enough data to establish cross-verification of properties over several sources. Because this work considers simultaneous measurement of density and surface tension, the coupled relationship between density and surface tension fills this gap by providing evidence of accurate measurements when considering density values agree so well.

In parallel, a novel high temperature system using the classic concepts for the falling ball viscometer was designed and implemented to obtain viscosity measurements

as a function of temperature for FLiNaK and NaF-ZrF₄. Measurements of both salts show general agreement to measurements found in published literature on similar salt compositions. Viscosity was evaluated with density values determined as part of this work in addition to selected density from literature. The lesser studied NaF-ZrF₄ shows nearly identical viscosity correlations to reported literature when using the as-measured density values. Viscosity values for FLiNaK show little difference based on density used since measured and reported density values are so similar. Other possible sources of errors were identified which could account for the measurement uncertainty. For instance, a larger number of samples would be expected to reduce error, as the existing number is relatively small with 6-10 samples per temperature. The high measurement rates obtainable with this method make this a feasible option. Additionally, evaluation of viscosity using density measurements performed on similarly prepared samples in this work would provide an ideal analysis due to variations in sample preparation across published work.

In all three properties, FLiNaK shows stronger agreement than NaF-ZrF₄ when comparing this work to published studies of similar compositions. This is somewhat associated with the ease of working with FLiNaK and the large quantity of high-quality data available in published studies, where measurement techniques have been refined over time to work well with FLiNaK. In comparison, published studies on NaF-ZrF₄ are limited and dated. Unlike NaF-ZrF₄, FLiNaK is considered a reference salt, and therefore well studied. As such it would be expected to have well defined properties with high accuracy. This kind of consideration can be observed when comparing viscosity

measurements of NaF-ZrF₄ as evaluated with different densities. Measured viscosity values only match reported viscosity values when using densities from this work are used as opposed to densities reported with the same composition.

Variation in these studies such as salt quality and preparation can affect measurement results. The characterization in this work was aimed at identifying the quality of the salt used to provide context when comparing to other studies. Results show the as-made samples contain low levels of impurities as analyzed by available techniques. This does not mean they are completely free of impurities, and the exact values are not determined by these methods. In addition, properties such as melting point remained comparable to values reported and theoretical values obtained from phase diagrams.

With confidence in as-made sample quality, it can be expected that sources of error in measurements would primarily be associated with each technique. Characterization of post measurement components and samples show this is a possibility, particularly with the maximum bubble pressure method. Because this method introduces gas directly into the salt, trace oxygen and moisture would be introduced directly into the salt. As these gases are highly likely to cause oxide, oxyfluoride, and increase corrosion rates. Signs of chromium loss from the stainless-steel tubes indicate chromium species are present in the salt. Therefore, results presented in this work must be evaluated under this context as composition will change slightly over the course of measurements.

Characterization of viscosity measurements show limited signs of introduced impurities, with only some possible indications of minimal Ti corrosion. This is the only metal exposed to the salts during measurements. Impurity levels were limited based on

presented characterization. In this case, minimal effects on measurements are expected.

In addition, it is important to note that the original intent of this work was to perform several property measurements together with the same setup. Over the course of this work, it was determined that the methods and designs chosen were not ideal for application of multiple methods. The introduction of impurities over the course of each measurement also plays a role in the consideration of attempting to measure several properties. In some cases, the original considerations associated with this intent, such as fixing the crucible diameter to 9mm for viscosity measurements, limited possibilities for improvement in measurement quality of density and surface tension.

In conclusion, the data collected in this work provides evidence of a successful demonstration of each measurement technique, however, with further minor refinements more accurate property measurements involving lesser uncertainties can be made.

6.2.Future Work

Suggestions for future work with these measurement techniques include possible efforts for reduction of uncertainty and additional analysis that could be performed in association with these properties.

Starting with viscosity, the largest source of error is expected to come from the sensor and electrical component of the system. Reduction of noise through a well-designed circuit with a faster sampling rate would improve sensitivity and signal quality. This would allow for more accurate determination of timing as the ball moves through each coil. A circuit redesign may also be able to increase the sensitivity of the sensor, allowing for smaller diameter balls to be used which would reach terminal velocity faster.

This could improve the measurable range of the device, allowing for lower viscosities to be accurately determined.

Designed after the viscosity system, the maximum bubble pressure method was designed to work in conjunction with the falling ball method setup. This overly constrained possible features that could have been changed to improve results. Separating the methods further would allow for more flexibility in critical dimensions of the maximum bubble pressure method. More freedom in these parameters would increase the accuracy of the surface tension measurements. The easiest modification that could be made to the surface tension measurement setup would be to enlarge the crucible to provide room to separate the reference wire, bubbling tube, and thermocouple. The crucible tube was originally fixed at 9mm so measurements could be done in tandem with the falling ball viscometer. This change would help with decreasing the variability due to capillary effects between the components and make it easier to use the reference wire accurately by providing more space to avoid the outer edges of the meniscus when probing the top of the fluid with the bubbling tube at the beginning of the surface tension measurements

Additionally, changing the bubbling tube material to pure Ni, such as Ni-200 or Ni-201, would help reduce contamination from corrosion and possibly help to eliminate early bubble release due to instabilities at the interfaces. Additional improvements could also include preheating of the gas to ensure gas temperature matches salt temperature, or more precise flow rate control to guarantee slow bubble formation.

Aside from these modifications, several aspects of this work could be expanded

upon to improve scientific understanding of the molten salts. As discussed, this work was performed in parallel with structural analysis of molten salts through MD modeling supported by x-ray scattering and absorption experiments. Additional modeling is expected to provide correlations between changes in property measurements and changes in structure as a function of temperature. Measurements of alternative components in these salt systems would help provide additional insight into the property relationship with structure. Other property measurements can be designed with this setup, such as electrical conductivity, which would provide further insights into the relationships between diffusivity, viscosity, and structure.

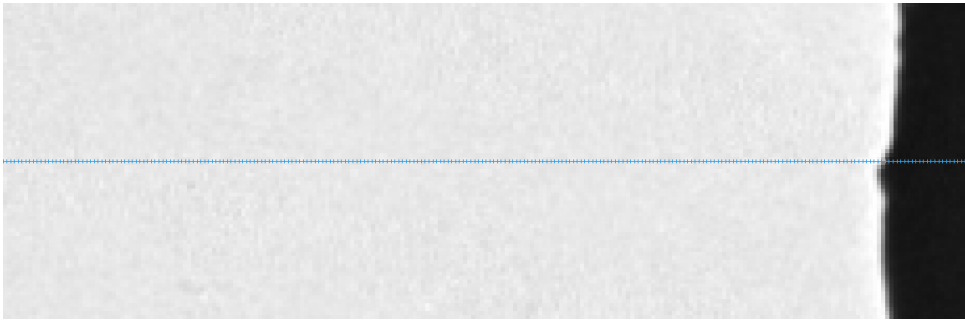
Lastly, an expanded study associated with impurities could be considered. While this study provides evidence that small levels of impurities do not significantly affect measurement results, a dedicated study with controlled quantities of impurities would be beneficial to support this argument. This could be expanded to include longer duration studies looking at the effects of impurities from moisture, oxygen or corrosion of relevant molten salt vessel materials on thermophysical properties. The longer duration study would be most relevant under the context of the lifecycle of the molten salts and associated technologies. In conjunction with efforts to reduce measurement error, it is expected that the falling ball viscometer and maximum bubble pressure methods are sensitive enough to measure the effects of these long-term compositional changes on thermophysical properties.

APPENDIX

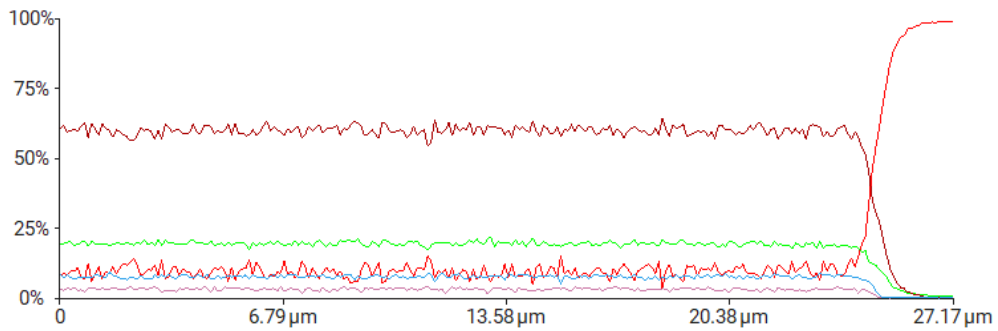
A.1. Original SEM/EDS Line Scan Results of Control Tube

	Element Number	Element Symbol	Element Name	Atomic Conc.	Weight Conc.
	6	C	Carbon	32.073	9.300
	24	Cr	Chromium	14.656	18.400
	25	Mn	Manganese	0.980	1.300
	26	Fe	Iron	45.164	60.900
	28	Ni	Nickel	7.128	10.100

Cut out of line scan (resolution: 256 points)



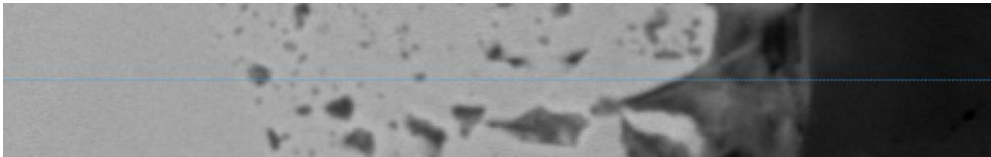
Combined line scan - Atomic



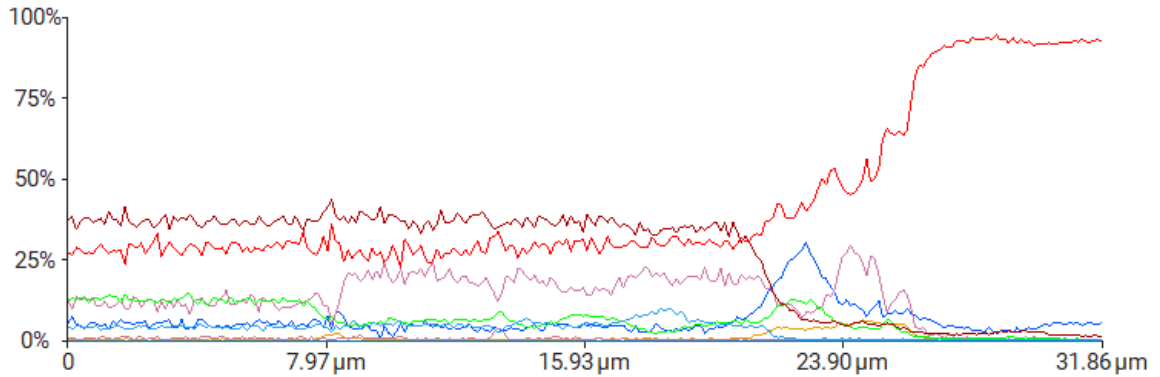
A.2. Original SEM/EDS Line Scan Results of the FLiNaK Tube

	Element Number	Element Symbol	Element Name	Atomic Conc.	Weight Conc.
	6	C	Carbon	55.666	23.400
	8	O	Oxygen	3.571	2.000
	9	F	Fluorine	3.308	2.200
	11	Na	Sodium	0.248	0.200
	19	K	Potassium	0.365	0.500
	24	Cr	Chromium	6.538	11.900
	25	Mn	Manganese	0.936	1.800
	26	Fe	Iron	23.378	45.700
	28	Ni	Nickel	5.988	12.300
	42	Mo	Molybdenum	0.000	0.000

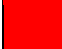









Cut out of Line Scan (resolution 256 points)



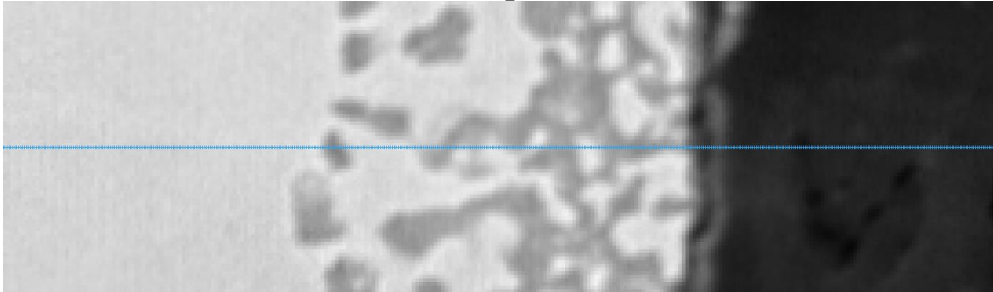
Combined line scan - Atomic



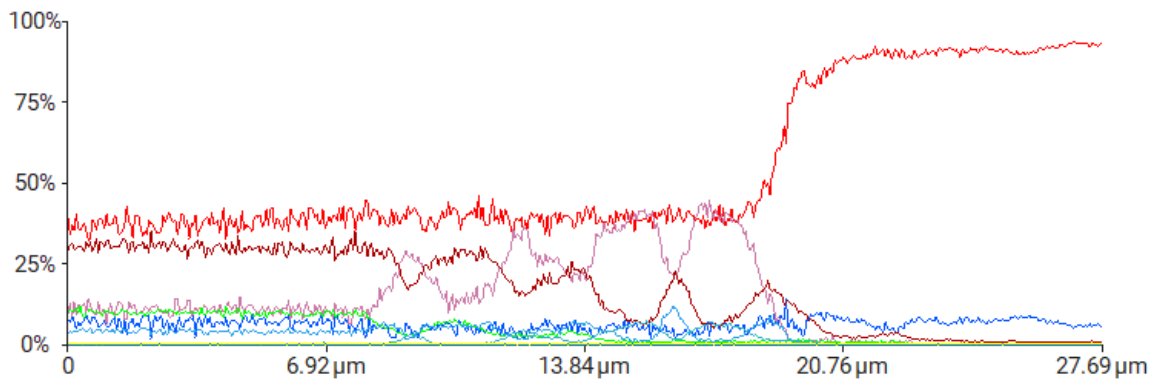
A.3. Original SEM/EDS Line Scan Results of the NaF-ZrF₄ Tube

	Element Number	Element Symbol	Element Name	Atomic Conc.	Weight Conc.
	6	C	Carbon	58.728	27.800
	8	O	Oxygen	11.893	7.500
	9	F	Fluorine	2.270	1.700
	11	Na	Sodium	0.221	0.200
	24	Cr	Chromium	2.586	5.300
	25	Mn	Manganese	0.000	0.000
	26	Fe	Iron	18.035	39.700
	28	Ni	Nickel	4.409	10.200
	40	Zr	Zirconium	1.196	4.300
	42	Mo	Molybdenum	0.079	0.300

Cut out of Line Scan (resolution 256 points)



Combined line scan - Atomic



A.4. Density Average Data Points

FLiNaK Density

Temperature (°C)	Density (kg/m ³)
558	2107.2
595	2048.3
620	2072.2
647	2012.6
682	2063.0
719	2027.0
748	1939.9

NaF-ZrF₄ Density

Temperature (°C)	Density (kg/m ³)
739	2988.5
707	2993.3
677	3075.7
642	3078.5
619	3107.1

A.5. Surface Tension Average Data Points

FLiNaK Surface Tension

Temperature (°C)	Surface Tension (mN/m)
558	180.4
595	187.3
620	174.9
647	174.1
682	164.7
719	166.4
748	154.6

NaF-ZrF₄ Surface Tension

Temperature (°C)	Surface Tension 1 ml/min Flow (mN/m)	Surface Tension 6ml/min Flow (mN/m)
615	155	158.2
644	151.4	144.8
675	147.7	146.7
704	147.9	133.4
733	140.4	133.8

A.6. Viscosity Average Data Points

FLiNaK Viscosity as Measured

Temperature (K)	Viscosity (cPs) Measured Density	Viscosity (cPs) Powers Density
753	11.217	11.38
771	7.808	7.56
791	7.179	7.0599
812	7.339	7.222
831	6.485	6.382
854	5.678	5.561
877	4.69	4.655

FLiNaK Viscosity MD

Temperature (K)	Viscosity (cPs) Powers Density
823	8.457
873	5.341
923	4.058
973	3.246
1023	2.285
1073	2.325
1123	1.614

NaF-ZrF₄ Viscosity as Measured

Temperature (K)	Viscosity (cPs) Measured Density	Viscosity (cPs) Cohen Density
828	10.606	9.518
850	8.521	7.629
873	6.556	5.803
893	6.456	5.576
915	6.354	5.362
934	5.928	5.077
955	5.137	4.352

NaF-ZrF₄ Viscosity MD

Temperature (K)	Viscosity (cPs) Cohen Density
798	11.665
823	9.626
848	9.795
873	6.660
898	6.657
923	7.290
948	5.202
973	3.828
1023	3.569
1073	3.407
1123	2.820

BIBLIOGRAPHY

- [1] H. Liu, X. Zhang, S. He, D. He, Y. Shang and H. Yu, Molten salts for rechargeable batteries, *Materials Today*, vol. 60, pp. 128–167, 2022.
<https://doi.org/10.1016/j.mattod.2022.09.005>
- [2] R. Roper, M. Harkema, P. Sabharwall, C. Riddle, B. Chisholm, B. Day and P. Marotta, "Molten salt for advanced energy applications: A review," *Annals of Nuclear Energy*, vol. 169, p. 108924, 2022.
<https://doi.org/10.1016/j.anucene.2021.108924>
- [3] Y. Mao, Y.-H. Hu, X.-Y. Hu, L.-Q. Yao, H. Li, L.-M. Lin, P. Tang, H. Li, S. Chen, J.-M. Li and G.-L. Chen, Molten Salts assisted Interfacial Engineering for Efficient and Low-Cost Full-inorganic Antimony Sulfide Solar Cells, *Advanced Functional Materials*, vol. 32, no. 48, p. 2208409, 2022.
<https://doi.org/10.1002/adfm.202208409>
- [4] "U.S. Nuclear Statistics," 18 Nov 2022. [Online]. Available:
<https://www.eia.gov/energyexplained/nuclear/data-and-statistics.php>
- [5] T. J. Dolan (ed.), *Molten Salt Reactors and Thorium Energy*, 1st Edition, Elsevier Science and Technology, 2017.
- [6] C. Forsberg, "Molten-Salt-Reactor Technology Gaps," Oakridge National Lab, Oak Ridge Tennessee, 2006. <https://www.osti.gov/etdeweb/biblio/21021093>
- [7] Gen-IV International Forum, "Technology Roadmap Update for Generation IV Nuclear Energy Systems," OECD Nuclear Energy Agency, 2014. <https://www.gen-4.org/gif/upload/docs/application/pdf/2014-03/gif-tru2014.pdf>
- [8] J. Serp, et al., "The molten salt reactor (MSR) in generation IV: Overview and perspectives," *Progress in Nuclear Energy*, vol. 77, pp. 308–319, 2014.
<https://doi.org/10.1016/j.pnucene.2014.02.014>
- [9] J. Uhlir, "Chemistry and technology of Molten Salt Reactors – history and perspectives," *Journal of Nuclear Materials*, vol. 360, pp. 6–11, 2007.
<https://doi.org/10.1016/j.jnucmat.2006.08.008>
- [10] S. Ladkany, W. Culberth and N. Loyd, "Molten Salts and Applications I: Molten Salt History, Types, Thermodynamic and Physical Properties, and Cost," *Journal of Energy and Power Engineering*, vol. 12, pp. 507–516, 2018. doi: 10.17265/1934-8975/2018.11.001
- [11] M. S. Sohal, M. A. Ebner, P. Sabharwall and P. Sharpe, "Engineering Database of Liquid Salt Thermophysical and Thermochemical Properties," Idaho National Laboratory, 2010. <https://doi.org/10.2172/980801>
- [12] Office of Nuclear Reactor Regulation. "Fuel Qualification for Molten Salt Reactors," US. Nuclear Regulatory Commission, NUREG/CR-7299, Oak Ridge,

- TN, 2022. <https://www.nrc.gov/reading-rm/doc-collections/nuregs/contract/cr7299/index.html>
- [13] B. W. Cottrell, H. E. Hungerford, J. K. Leslie and J. L. Meem, "Operation of the Aircraft Reactor Experiment, ORNL-1845," Oakridge National Laboratory, 1955. <https://doi.org/10.2172/4237975>
- [14] D. F. Williams, L. M. Toth and K. T. Clarno, "Assessment of Candidate Molten Salt Coolants for the Advanced High-Temperature Reactor (AHTR)," Oakridge National Laboratory, ORNL/TM-2006/12, 2006. <https://doi.org/10.2172/1360677>
- [15] D. F. Williams, P. F. Britt, "Report for DOE (Office of Nuclear Energy), Molten Salt Chemistry Workshop," Oakridge National Laboratory., April 2017. https://www.ornl.gov/sites/default/files/Molten%20Salt%20Workshop_Final_092917.pdf
- [16] T. Porter, M. M. Vaka, P. Steenbik and D. D. Corte, "Computational methods to simulate molten salt thermophysical properties," *Communications Chemistry*, vol. 5, no. 69, pp. 1-15, 2022. <https://doi.org/10.1038/s42004-022-00684-6>
- [17] A. Rodriguez, S. Lam and M. Hu, "Thermodynamic and Transport Properties of LiF and FLiBe Molten Salts with Deep Learning Potentials," *Applied Materials & Interfaces*, vol. 13, no. 46, pp. 55367-55379, 2021. <https://doi.org/10.1021/acsami.1c17942>
- [18] A. Wadehra, R. Chahal, S. Banerjee, A. Levy, Y. Zhang, H. Yan, D. Olds, Y. Zhong, U. Pal, S. Lam and L. Karl, "X-ray and molecular dynamics study of the temperature-dependent structure of molten NaF-ZrF₄," *Physical Review Materials*, vol. 8, no. 7, pp. 075402, 2024. <https://doi.org/10.1103/PhysRevMaterials.8.075402>
- [19] J. Guo, Y. Zhang, K. Ludwig, H. Yan, A. Levy, A. Wadehra, M. C. Gao, B. Chris, M. Rose, N. Condon, A. Powell, Y. Zhong and U. Pal, "X-ray and molecular dynamics study of the temperature-dependent structure of FLiNaK," *Nuclear Materials and Engineering*, vol. 37, no. 101530, 2023. <https://doi.org/10.1016/j.nme.2023.101530>
- [20] A. Y. Galashev, O. R. Rakhmanova, K. A. Abramova, K. P. Katin, M. M. Maslov, O. Y. Tkacheva, A. V. Rudenko, A. A. Kataev and Y. P. Zaikov, "Molecular Dynamics and Experimental Study of the Effect of CeF₃ and NDF₃ additives on Physical properties of FLiNaK," *The Journal of Physical Chemistry B*, vol. 127, no. 5, pp. 1197-1208, 2023. <https://doi.org/10.1021/acs.jpcc.2c06915>
- [21] R. O'Harye, "Materials Kinetics Fundamentals", 1st edition, Hoboken, New Jersey: John Wiley & Sons Inc., 2015.
- [22] A. J. Bard and L. R. Faulkner, "Electrochemical Methods", 3rd Edition, Hoboken New Jersey: John Wiley & Sons, 2022.
- [23] M. Liu, X. Li, T. Xu, L. Yan and Z. Tang, "Mapping relationships between cation-F bonds and the heat capacity, thermal conductivity, viscosity of molten NaF-BeF₂,"

- Journal of Molecular Liquids*, vol. 345, pp. 118915, 2022.
<https://doi.org/10.1016/j.molliq.2022.118915>
- [24] S.-C. Lee, Y. Zhai, N. P. Walter, M. Rose, B. J. Heuser and Z. Yang, "Comparative Studies of the Structural and Transport Properties of Molten Salt FLiNaK Using the Machine-Learned Neural Network and Reparametrized Classical Forcefields," *The Journal of Physical Chemistry B*, vol. 125, pp. 10562-10570, 2021.
- [25] R. C. Gallagher, C. Agca, N. Russel, J. W. McMurry and N. D. Ezell, "Assessment of molten eutectic LiF-NaF-KF density through experimental determination and semi-empirical modeling," *Journal of Chemical Engineering Data*, vol. 67, no. 6, pp. 1406-1414, 2022. <https://doi.org/10.1021/acs.jced.2c00081>
- [26] M. A. Rose, E. Wu and M. A. Williamson, "Thermophysical Property Measurements: Improved Density, Viscosity and Thermal Diffusivity Methods," Argonne National Lab, ANL/CFCT-20/38, 2020. <https://doi.org/10.2172/1734862>
- [27] M. Rose, J. Krueger, T. Lichtenstein, E. Wu and G. L., "Precision of Property Measurements with Reference Molten Salts," Argonne National Lab, ANL/CFCT-21/20, 2021. <https://doi.org/10.2172/1823476>
- [28] J.-H. Cheng, P. Zhang, X.-H. An, K. Wang, Y. Zuo, H.-W. Yan and Z. Li, "A Device for Measuring the Density and Liquidus Temperature of Molten Fluorides for Heater Transfer Storage," *Chinese Physical Letters*, vol. 30, no. 12, p. 126501, 2013. <http://dx.doi.org/10.1088/0256-307X/30/12/126501>
- [29] S. W. Hughes, "Measuring liquid density using Archimedes' principle," *Physics Education*, vol. 41, pp. 445-447, 2006. <https://doi.org/10.1088/0031-9120/41/5/011>
- [30] G. Lui, J. M. Toguri, and N. M. Stubina, "Surface tension and density of the molten LaCl₃-NaCl binary system," *Canadian Journal of Chemistry*, vol. 65, pp. 2779-2782, 1987. <https://doi.org/10.1139/v87-462>
- [31] O. Y. Tkacheva, A. V. Rudenko, A. A. Kataev, P. N. Mushnikov, A. S. Kholkina and Y. P. Zaikov, "The Viscosity of Molten Salts based on the LiF-BeF₂ System", *Metallurgy of Nonferrous Metals*, vol 63, pp. 276-283, 2022. <https://doi.org/10.3103/S1067821222030117>
- [32] T. Ito, N. Kojima and A. Nagashima, "Redetermination of the Viscosity of Molten NaCl at Elevated Temperatures", *International Journal of Thermophysics*, vol. 10 no. 4, pp. 819-831, 1989. <https://doi.org/10.1007/BF00514478>
- [33] K. Korklep and K. A. Oye, "An absolute oscillating-cylinder (or cup) viscometer for high temperatures," *Journal of Physical Engineering: Science Instrumentation*, vol. 12, no. 9, pp. 875-885, 1979. DOI 10.1088/0022-3735/12/9/021
- [34] A. Birri, N. Termini, P. J. Rose, S. Chapel, H. Andrews and N. D. B. Ezell, "Development and demonstration of a rolling ball viscometer for molten salts with

- near-minimum liquidus NaCl-KCl," *Thermal Science and Engineering Progress*, vol. 44, pp. 102029. 2023. <https://doi.org/10.1016/j.tsep.2023.102029>
- [35] M. B. Valentim, M. J. V. Lourenço, C. A. Nieto de Castro, "Correct Use of Oscillating-Cup Viscometers for High Temperature Absolute Measurements of Newtonian Melts," *International Journal of Thermophysics*, vol. 45, no. 64, pp. 1-20, 2024. <https://doi.org/10.1007/s10765-024-03355-x>
- [36] K. Torklep, and H. A. Oye "Viscosity of the Eutectic LiF-NaF-KF Melt (FLiNaK)," *Journal of Chemical Engineering Data*, vol. 25, pp. 17-21, 1980. <https://doi.org/10.1021/je60084a007>
- [37] M. Abe, *Measurement Techniques and Practices of Colloid and Interface Phenomena*, Noda, Japan: Springer Nature Singapore Pte Ltd, 2016.
- [38] M. Korenko and F. Šimko, "Measurement of Interfacial Tension in Liquid-Liquid High-Temperature Systems," *Journal of Chemical Engineering Data*, vol. 55, no. 11, pp. 4561-4573, 2010. <https://doi.org/10.1021/je1004752>
- [39] G. J. Janz, J. Wong and G. R. Lakshminarayanan, "Surface-Tension Techniques for Molten Salts," *Instrumentation Science & Technology*, vol. 1, no. 3, pp. 261-272, 1969. <https://doi.org/10.1080/10739146908543252>
- [40] K. Grjotheim, J. L. Holm, B. Lillebuen and H. A. Oye, "Surface Tension of Liquid Binary and Ternary Chloride Mixtures," *Acta Chemica Scandinavica*, vol. 26, no. 5, pp. 2050-2062, 1972. http://actachemscand.org/pdf/acta_vol_26_p2050-2062.pdf
- [41] E. Sada, S. Katoh and H. G. Damie, "Surface Tension of Some Molten Salt Hydrates by the Pendant Drop," *Journal of Chemical Engineering*, vol. 29, no. 2, pp. 117-119, 1984. <https://doi.org/10.1021/je00036a003>
- [42] J. Long, Y. Wang, Y. Zeng, X. Xiong, X. Li, H. Lun, Z. Ye, J. Hu, G. Sen, S. Chen, G. Yang, R. Li, T. Li and J. Zhang, "Surface tension measurement of Ti-Zr and Ti-Hf alloys at high-temperature by the pendant drop method," *Vacuum*, vol. 200, pp. 111045, 2022. <https://doi.org/10.1016/j.vacuum.2022.111045>
- [43] Z. Zhou, L. R. Cantu, X. Chen, M. R. Alexander, C. J. Roberts, R. Hague, C. Tuck, D. Irvine, and R. Wildman. "High-throughput characterization of fluid properties to predict droplet ejection for three-dimensional inkjet printing formulas," *Additive Manufacturing*, vol. 29, pp. 100792, 2019. <https://doi.org/10.1016/j.addma.2019.100792>
- [44] T. Hartmann and P. Paviet, "Corrosion of Containment Alloys in Molten Salt Reactors and the Prospect of Online Monitoring," *Journal of Nuclear Fuel Cycle and Waste Technology*, vol. 20, no. 1, pp. 43-63, 2022. <https://doi.org/10.7733/jnfcwt.2022.005>
- [45] D. E. Holcomb and S. M. Cetiner, "An Overview of Liquid-Fluoride-Salt Heat Transport Systems," Oakridge National Lab, ORNL/TM-2010/156, 2010. <https://doi.org/10.2172/990239>

- [46] A. K. Misra and J. D. Whittenberger, "Fluoride Salts and Container Materials for Thermal Energy Storage Applications in Temperature Range 973 to 1400K," AIAA-87-9226, Lewis Research Center, NASA, Cleveland Ohio, 1987.
<https://ntrs.nasa.gov/api/citations/19870014593/downloads/19870014593.pdf>
- [47] J. H. Shaffer, "Preparation and Handling of Salt Mixtures for The Molten Salt Reactor Experiment," Oak Ridge National Laboratory, ORNL-4616, Jan 1971.
<https://doi.org/10.2172/4074869>
- [48] C. Wang, X. Chen and Y. Gong, "On the Structures of Thorium Fluoride and Oxyfluoride Anions in Molten FLiBe and FLiNaK," *The Journal of Physical Chemistry B*, vol. 125, no. 6, pp. 1640-1646, 2021.
<https://doi.org/10.1021/acs.jpccb.0c10197>
- [49] A. A. Maslennikova, P. N. Mushnikov, A. V. Dub, O. Y. Tkecheva, Y. P. Zaikov, Y. L. Liu and W. Q. Shi, "Determination of the Oxygen Content in the Li-NaF-KF Melt. Materials (Basel).," *Materials*, vol. 16, no. 11, pp. 4197, 2023.
<https://doi.org/10.3390/ma16114197>
- [50] C. Li, T. Wen, K. Liu, J. Dequan, Z. Jiang and Y. Wang, "Controllable Syntheses, Crystal Structure Evolution, and Photoluminescence of Polymorphic Zirconium Oxyfluorides," *Inorganic Chemistry*, vol. 60, no. 18, pp. 14382-14389, 2021.
<https://doi.org/10.1021/acs.inorgchem.1c02176>
- [51] K. Patel, C. Mahajan, S. Muskeri and S. Makherjee, "Corrosion Behavior of Refractory High-Entropy Alloys in FLiNaK Molten Salts," *Metals*, vol. 13, no. 3, pp. 450, 2023. <https://doi.org/10.3390/met13030450>
- [52] P. Virtanen, R. Gommers, T.e. Oliphant, et al, "Fundamental Algorithms for scientific computing in Python," *Nature Methods*, vol. 17, pp. 261-272, 2020.
<https://doi.org/10.1038/s41592-019-0686-2>
- [53] H. L. Chan, E. Romanovskaia, V. Romanovski, D. Sur, M. Hong, P. Hosemann and J. R. Scully" Corrosion Electrochemistry of Chromium in Molten FLiNaK Salt at 600 °C," *Journal of The Electrochemical Society*, vol. 170, no. 081502, 2023.
10.1149/1945-7111/ace8c0
- [54] A. E. Danon, O. Muransky, I. Karatchevtseva, Z. Zhang, J. Z. Li, N. Scales, J. J. Kruzic and I. Edwards, "Molten salt corrosion (FLiNaK) of a Ni–Mo–Cr alloy and its welds for application in energy-generation and energy-storage systems," *Corrosion Science*, vol. 164, pp. 108306, 2020.
<https://doi.org/10.1016/j.corsci.2019.108306>
- [55] S. E. Eklund, Q. J. Chambers, G. Mamantov, J. Diminie and C. E. Barnes, "Tungsten Fluorides: Syntheses and Electrochemical Characterization in the FLiNaK Molten Salt Eutectic," *Inorganic Chemistry*, vol. 40, no. 4, pp. 715-722, DOI 10.1021/ic000491o, 2001.

- [56] C. J. Barton, W. R. Grimes, R. E. Moore and R. E. Thoma, "PHASE EQUILIBRIA IN THE SYSTEMS NaF-ZrF₄, UF₄-ZrF₄ AND NaF-ZrF₄-UF₄," *Journal of Physical Chemistry*, vol. 63, no. 6, p. 665–676, 1957, doi.org/10.1021/j150564a008.
- [57] C. W. Bale, E. Belisle, P. Chartrand, S. A. Deckerov, G. Eriksson, A. E. Gheribi, K. Hack, I. H. Jung, Y. B. Kang, J. Melancon, A. D. Pelton, S. Petersen, C. Robelin, J. Sangster, P. Spencer and M.-A. Van Ende, "FactSage Thermochemical Software and Databases-2010-2016," *Calphad*, vol. 54, no. <www.factsage.com>, pp. 35-53, 2016.
- [58] W.B. Cottrell, H. E. Hungerford, J. K. Leslie, and J. L. Meem, "Operation of the Aircraft Reactor Experiment, ORNL-1845," Oakridge National Lab, ORNL-1845. <https://doi.org/10.2172/4237975>
- [59] R. Romatoski and L. Hu, "Fluoride salt coolant properties for nuclear reactor applications: A review," *Annals of Nuclear Energy*, vol. 109, pp. 635-647, 2017. <https://doi.org/10.1016/j.anucene.2017.05.036>
- [60] P. Barborík, Z. Vasková, M. Boča and J. Prišćák, "Physicochemical properties of the system (LiF + NaF + KF (eut.) + Na₇Zr₆F₃₁): Phase equilibria, density and volume properties, viscosity and surface tension," *Journal of Chemical Thermodynamics*, vol. 76, pp. 145-151, 2014. <https://doi.org/10.1016/j.jct.2014.03.024>
- [61] S. I. Cohen and T. N. Jones, "Viscosity Measurements of Molten Fluoride Mixtures," Oakridge National Laboratory, ORNL-2278, 1957. <https://doi.org/10.2172/4803933>
- [62] T. Fujisawa, T. Utigard and J. M. Toguri, "Surface tension and density of the molten Pb-Cl₂-KCl-NaCl ternary system," *Canadian Journal of Chemistry*, vol. 63, no. 5, pp. 1132-1138, 1985. <https://doi.org/10.1139/v85-192>
- [63] G. J. Janz, "Thermodynamic and Transport Properties for Molten Salts: Correlation Equations for Critically Evaluated Density, Surface Tension, Electrical Conductance and Viscosity Data," *Physical and Chemical Reference Data*, vol. 17, no. 2, 1988. <https://srd.nist.gov/JPCRD/jpcrdS2Vol17.pdf>
- [64] B. Kubíková, P. Viliam, I. Macková and M. Boča, "Surface tension and viscosity of the molten (LiF–NaF–KF) eut–K₂ZrF₆ system," *Monatshefte für Chemie*, vol. 143, pp. 1459-1462, 2012. <https://doi.org/10.1007/s00706-012-0832-3>
- [65] T. Tanaka, A. Niino, N. Hirai and S. Hara, "Surface Tension of Molten LiF-MgF₂, CaF₂ and SrF₂ Binary Systems," *High Temperature Materials and Processes*, vol. 22, no. 3-4, pp. 151-156, 2003. <https://doi.org/10.1515/HTMP.2003.22.3-4.151>
- [66] P. Bhatnagar, S. Siddiqui, I. Sreedhar and R. Parameshwaran, "Molten Salts: Potential candidates for thermal energy storage applications," *Energy Research*, vol. 46, no. 13, pp. 17755-17785, 2022. <https://doi.org/10.1002/er.8441>

- [67] "G.E.N.-IV International-Forum, GIF R&D Outlook for Generation IV Nuclear Energy Systems, Generation IV International Forum (GIF)," 2009. https://www.gen-4.org/gif/upload/docs/application/pdf/2013-09/gif_rd_outlook_for_generation_iv_nuclear_energy_systems.pdf
- [68] A. Bhattad, "Review on viscosity measurement: devices, methods and models," *Journal of Thermal Analysis and Calorimetry*, vol. 148, pp. 6527-6543, 2023. <https://doi.org/10.1007/s10973-023-12214-0>
- [69] M. Brizard, M. Megharfi, C. Verdier and E. Mahe, "Design of a High Precision Falling Ball Viscometer", *Review of Scientific Instruments*, vol. 76, no. 2, pp. 025109, 2005. <https://doi.org/10.1063/1.1851471>
- [70] R. Sobczak, "Viscosity measurement by spheres falling in a magnetic field," *Rheologica Acta*, vol. 25, no. 2, pp. 175-179, 1986. <https://doi.org/10.1007/BF01332136>
- [71] L. R. Powell, L. A. Mondy, G. G. Stoker, J. W. Milliken and L. A. Graham, "Development of a falling ball rheometer with applications to opaque systems: measurements of the rheology of suspensions of rods," *Journal of Rheology*, vol. 33, pp. 1173-1188, 1989. <https://doi.org/10.1122/1.550054>
- [72] A. Bougas and M. Stamatoudis, "Wall Factor for Acceleration and Terminal Velocity of Falling Spheres at High Reynolds Numbers," *Chemical Engineering Technology*, vol. 16, no. 5, pp. 314-317, 1993. <https://doi.org/10.1002/ceat.270160506>
- [73] A. V. Singh, L. Sharma and P. Gupta-Bhaya, "Studies on Falling Ball Viscometry," *arXiv*, 2012. <https://doi.org/10.48550/arXiv.1202.1400>
- [74] T. A. Johnson and V. C. Patel, "Flow pas a sphere up to a Reynolds number of 300," *Journal of Fluid Mechanics*, vol. 378, pp. 19-70, 1999. <https://doi.org/10.1017/S0022112098003206>
- [75] H. v. Wahl, T. Richter, S. Frie and T. Hagemeyer, "Falling balls in a viscous fluid with contact: Comparing numerical simulations with experimental data," *Physics of Fluids*, vol. 33, pp. 033304, 2021. <https://doi.org/10.1063/5.0037971>
- [76] S. Feng, A. L. Graham, P. T. Reardon, J. Abbott and L. Mody, "Improving Falling Ball Tests for Viscosity Determination," *Journal of Fluids Engineering*, vol. 128, no. 1, pp. 157-163, 2006. <https://doi.org/10.1115/1.2137345>
- [77] J. Happel and H. Brenner, "Low Reynolds number hydrodynamics," Boston: Martinus Njhoff Publishers, 1983.
- [78] COMSOL, "Terminal Falling Velocity of a Sand Grain (Application ID 983)," COMSOL Application Gallery, 2024. <https://www.comsol.com/model/terminal-falling-velocity-of-a-sand-grain-983>

- [79] P. Lyu, "How Do I Compute Lift and Drag?" 16 June 2015. [Online]. Available: <https://www.comsol.com/blogs/how-do-i-compute-lift-and-drag/>. [Accessed 29 April 2024].
- [80] S. Takamoto, et al. "Towards universal neural network potential for material discover applicable to arbitrary combination of 45 elements.," *Nature Communications*, vol. 13, no. 1, pp. 2991, 2022. <https://doi.org/10.1038/s41467-022-30687-9>
- [81] P. Bordat and F. Müller-Plathe, "The shear viscosity of molecular fluids: A calculation by reverse nonequilibrium molecular dynamics," *The Journal of Chemical Physics*, vol. 116, no. 8, pp. 3362-3360, 2002. <https://doi.org/10.1063/1.1436124>
- [82] B. Vriesema, "Aspects of molten fluorides as heat transfer agents for power generation," WTHD No. 112, Delft University of Technology, 1979. <https://repository.tudelft.nl/record/uuid:9e8deede-eebe-4621-b962-d4afcc2a5038>
- [83] J. Cibulková, M. Chrenková, R. Vasiljev, V. Kremenetsky and M. Boča, "Density and Viscosity of the (LiF+NaF+KF)eut(1)+K2TaF7(2)+Ta2O5 (3) Melts," *Journal of Chemical Engineering*, vol. 51, no. 3, pp. 984-987, 2006. <https://doi.org/10.1021/je050490g>
- [84] J. Ambrosek, M. Anderson, K. Sridharan and T. Allen, "Current Status of Knowledge of Fluoride Salt (FLiNaK) Heat Transfer," *Nuclear Technology*, vol. 165, pp. 166-173, 2009. <https://doi.org/10.13182/NT165-166>

CURRICULUM VITAE

